FABRICATION AND TESTING OF NbN/MgO/NbN TUNNEL JUNCTIONS FOR USE AS HIGH-FREQUENCY HETERODYNE DETECTORS

Thesis by

Jeffrey Aaron Stern

In Partial Fulfillment of the Requirements

for the Degree of

Doctor of Philosophy

California Institute of Technology

Pasadena, California

1991

(Submitted August, 1990)

Acknowledgements

I would like to thank all the people who have helped me complete my Ph.D. In attempting this task, I realize that many friends, cohorts, and relatives, cannot be mentioned by name. To all of you, I must say many thanks. My life here at Caltech has been enriched by my interaction with you. Having said this, I will attempt to mention some of the people who have played a large role in my tenure here in Pasadena.

Many people have helped me develop from a green-eared graduate student into a capable researcher. First, and foremost I would like to thank Rick LeDuc. Rick has worked with me for over five years at JPL on NbN junction fabrication. He has been a role model for me, with his dedication to research. Rick has taught me much of what I know as an experimental scientist. From the very beginning Rick treated me as an equal, with respect. I cannot thank him enough for these five years.

Mike Wengler also helped to shape my early years at Caltech. To Mike I offer thanks, not only for teaching me about SIS mixers, but for being a friend, and confidant. Mike's support and enthusiasm made my early years at Caltech both instructional and enjoyable.

Many other people at Caltech helped to create a relaxed, stimulating, and generally enjoyable atmosphere to work in. Thank you to the entire submillimeter group. I offer special thanks to my long-time office-mate Erich Grossman and my current office-mate Thomas Büttgenbach. Additionally, everyone in the submillimeter group has been friendly and supportive. Our softball team "Down's syndrome" has also offered a relaxed getaway from everyday work, which I have appreciated.

My group at JPL has also been friendly, supportive, and knowledgeable. Let me especially thank Brian Hunt, who helped bring an influx of new ideas with his arrival from GE. His cynical wit always made JPL a special place. Brian and his wife Linda have also helped to liven up more than a few dinner parties. The rest of the JPL gang (Scott Cypher, Bruce Bumble, Mark Foote and Andreas Judas) have all been great to work with as well. Several group supervisors at JPL have also helped to support my research, both politically and financially. For this help special thanks go to Satish Khanna, Barbara Wilson, and Paula Grunthaner.

I would like to offer thanks to Rob McGrath and Dave Miller for working on two key measurements in this thesis. The receiver used for all the RF testing was assembled by Rob and Curtis Byrom. Additionally, Rob worked with me on most of the RF tests. Thanks, Rob, for teaching me about precision RF testing, and helping me complete my thesis work. Dave Miller performed the RF loss measurements mentioned in Chapter 3. This information has given me insight into the possible loss mechanisms in NbN films. Thanks to both of you for your collaborations with me.

Finally, and very importantly, I would like to thank Tom Phillips, my advisor. Tom has always given

me a great deal of freedom to pursue a difficult project. Tom waited patiently through the long process of developing NbN junctions. Thank you Tom, for your support and patience during my graduate career.

Many of my friends have also played an important role in my years at Caltech. They have supported me emotionally, and helped me from falling into a zero social life, so common at Caltech. I will mention only a few friends by name, but to all my friends, I have enjoyed my life in Pasadena a great deal because of you.

Let me mention three special friends by name. First, my two long-time house-mates Dave Dickie and Jeff Goldsmith have made my years here more than enjoyable. Jeff and I have enjoyed many bridge and poker games, concerts, and a host of other good times I cannot mention in public. Thanks, Jeff. You have been a true friend. Dave and I have also enjoyed great times together. The most special in my mind are the death-defying ski runs at Mammoth Mountain and our life-endangering Scuba trips to Laguna Beach. Dave may, in particular, remember the infamous Lobster Hunt of 1988. Dave has been a true confidant, good friend, and fellow maniac. Thanks, Dave (I think). Finally, I must thank my good friend Jennifer Stern. At this time, I will come forward, and publicly deny that we were ever married. Seriously, Jennifer has been a great friend. We have enjoyed many wonderful times, and many wonderful bottles of wine together. To these three close friends, I offer a special thanks for supporting me as only true friends can.

My family has always been very close to me, and their support throughout my life has helped me become the person I am. My mother and father are two of the best parents in any galaxy. I love them both a great deal. From the earliest baking soda and vinegar experiments my mother showed us, they have encouraged my inquisitive scientific thinking. Thank you, Mom and Dad. My siblings are also three of my best friends in the world. They are all special and wonderful to me. In particular, I have enjoyed having Ben and Libby out here in southern California. I have had great times with them at dinner parties, golf matches and swim meets.

Finally, let me thank the person who is most important to me in the world, Alison. The last year and a half have been the most enjoyable of my life, because of my relationship with Alison. I have hardly noticed any of the drudgery of thesis writing, because I am able to put my work away at home and enjoy our time together. Alison has been supportive of this thesis, and has helped me cure several bad writing habits. Because of her this is a much better written-document. Thank you, Alison, for your support and love.

Abstract

This thesis describes the development and testing of NbN/MgO/NbN tunnel junctions for use as superconductor-insulator-superconductor (SIS) mixers. SIS mixers are the most sensitive heterodyne detectors in the millimeter wavelength region. Most SIS mixers use Pb alloy tunnel junction. These tunnel junctions have several problems associated with the soft nature of Pb and its low superconducting transition temperature. NbN-based tunnel junctions are being developed to overcome these difficulties. These devices are intended to be used as mixers at millimeter and submillimeter wavelengths. This thesis describes the fabrication process involved in making NbN junctions, and the results of measurements on these devices. The purpose of these measurements is to determine the future possibilities of NbN tunnel junctions as high-frequency mixers.

The first chapter is an introduction to SIS mixers and explains how tunnel junction properties affect mixer performance. The basic theory of tunneling and mixing in SIS mixers is first presented. A description of quantum mixer theory is included in this presentation. This theory makes several interesting predictions that cannot be explained using classical theories. This is followed by a description of how real SIS tunnel junctions differ from ideal junctions. The physical origin of these differences is discussed, along with how they affect SIS mixer performance. Finally, the advantages and disadvantages of the various superconducting materials available are discussed. The decision to develop NbN devices is based on these material properties.

The second chapter describes the methods used to fabricate small-area NbN/MgO/NbN tunnel junctions. The chapter begins with a description of the various methods that have been used to deposit NbN films. Reactive magnetron sputtering is chosen as the best method for tunnel junction fabrication. Details on the vacuum systems and the methods used for depositing superconducting NbN are discussed. Next, the process used for depositing junction trilayers (NbN/MgO/NbN) is described. The probable growth mode of MgO on NbN is presented. The importance of this growth mode to the junction quality is explained in some detail. Next, standard junction processing steps are reported. The details and limitations of each step are put forth. The standard process allows for the fabrication of 1 μm^2 tunnel junctions. Finally, this chapter discusses several methods of fabaricating submicron junctions that are being pursued. The status of this work is given.

The third chapter describes the characterization of NbN films and NbN/MgO/NbN tunnel junctions. Film properties are described first. The correlation of these properties to deposition conditions is discussed in some detail. Next, values for the various features of the I-V characteristic are given; typical and exceptional values are noted. How these features limit mixer results is described in detail. Several important device attributes were measured using superconducting-quantum-interference-devices (SQUIDs).

These attributes are the junction's specific capacitance and the film's magnetic penetration depth. The theory and results of measuring specific capacitance and penetration depth are presented. Following the SQUID results is a large section on RF testing. Mixer tests were made at 205 GHz. The receiver design used, integral inductive tuning circuit used and results are discussed. These results are well understood, with the exception of the temperature dependence of the mixer performance. Finally, measurements of the uniformity of many junctions on a single wafer are presented. The importance of junction uniformity is also described.

The final chapter discusses the ultimate limits on NbN mixers, and tells what future work must be done to achieve these limits. The primary high-frequency limit on NbN junctions is the capacitance of NbN/MgO/NbN junctions. The limit imposed by the junction capacitance and circuits used to tune out this capacitance are discussed. Also, the low-frequency limits on NbN junctions are discussed. The status of submicron devices is presented. Junction area is the most immediate limitation on NbN mixer results. The possibility of using other barrier materials to increase the RC speed of NbN junctions is presented. Finally, the possibility of operating NbN junctions at temperatures above 4.2 K is discussed.

Table of Contents

Acknowledgements ii

Abstract iv

List of Figures viii

List of Tables x

Chapter I–Introduction 1

A. Submillimeter Astronomy 1

B. SIS Mixers 4

C. Properties of Real SIS Tunnel Junctions 9

D. Materials Choices for SIS Mixers 15

Chapter II–Device Fabrication 20

A. NbN Deposition 20

B. Barrier and Junction Trilayer Deposition 26

C. Standard Junction Processing 30

D. Submicron Device Processing 35

E. Chapter Summary 38

Chapter III–Materials and Device Characterization 39

A. Resistance as a Function of Temperature 39

B. Current Voltage Characteristics 43

C. SQUID Measurements 58

D. RF Testing 65

E. Junction Uniformity 83

F. Chapter Summary 86

Chapter IV–Conclusions and Future Work 89

A. RF Limitation of NbN/MgO/NbN Junctions 89

B. Submicron Devices 91

C. New Barriers and New Superconducting Materials 91

D. Operation of NbN junctions on Closed Cycle Refrigerators 93

Appendix A–The Josephson Effect 95

Appendix B–Photoresist Processing 99

Appendix C–SQUID Measurement Circuit 101

Appendix D–SQUID Data Summary 103

Appendix E–RF Testing Summary 105

Appendix F–Mask Modification Procedure 107

References 109

List of Figures

1.1 Schematic of upper and lower sideband, LO and intermediate frequencies 3

1.2 SIS tunneling 5

1.3 Semiconductor picture of photon-assisted tunneling 8

1.4 Stylized SIS I-V characteristic 9

1.5 Leaky I-V characteristic 11

1.6 Semiconductor picture of multiparticle tunneling 12

2.1 Schematic diagram of magnetron sputtering 22

2.2 Schematic diagram of vacuum deposition system 25

2.3 Transmission electron micrograph of a NbN/MgO/NbN trilayer 28

2.4 Reactive ion etching system 30

2.5 Mesa junction processing steps 34

2.6 Cross-line junction processing steps 35

2.7 Spin on glass, etch-back junction processing steps 37

3.1 Resistance versus temperature plots 40

3.2 SIS I-V characteristic for nonidentical superconductors 45

3.3 SIS I-V characteristic with an extremely large gap voltage 46

3.4 SIS I-V characteristic with a large gap voltage for an unheated substrate 47

3.5 SIS I-V characteristics with narrow and broad onset of tunneling at the gap voltage 48

3.6 SIS I-V characteristic with a large subgap resistance 49

3.7 Multiparticle tunneling I-V characteristics 50

3.8 SIS I-V characteristic showing the effect of self-heating on the gap voltage 54

3.9 SIS I-V characteristics at different temperatures 55

3.10 I-V properties as a function of temperature 56

3.11 SIS I-V characteristic showing electrode switching 57

3.12 Sketch and schematic circuit diagram for a SQUID 60

3.13 Modulation curve and voltage resonance for a SQUID 62

3.14 Specific capacitance versus log(R_nA) 63

3.15 SQUID critical current maxima versus control current 64

3.16 Graphical calculation of receiver noise 67

3.17 Equivalent lumped element circuit for a wire inductor tuning circuit 69

3.18 I-V characteristic showing stub resonances 71

3.19 Mixer I-V characteristic with and without LO power applied 74

3.20 Mixer noise temperature and conversion gain versus signal frequency 75

3.21 IF power versus voltage with a hot and cold load at the mixer input 75

3.22 Mixer performance as a function of capacitance tuned by the stub 77

3.23 Mixer I-V characteristic at two temperatures 78

3.24 Diagram of RF loss measurement apparatus 81

3.25 Absorptivity of NbN as a function of frequency 82

3.26 Series array I-V characteristic for 10 junctions 84

3.27 Series array I-V characteristics for 100 junctions 85

3.28 Histogram of critical currents 86

4.1 I-V characteristic for a junction fabricated using the SOG etch-back process 92

A.1 SQUID schematic 96

C.1 SQUID measurement circuit 101

F.1 Mask modification procedure 107

List of Tables

2.1 Conditions for NbN deposition 26

2.2 RIE etch rates 31

3.1 I-V characteristic summary 57

3.2 NbN microstrip line loss as a function of frequency 80

Appendix D SQUID Data summary 103

Appendix E RF testing summary 105

Chapter I. Introduction

This thesis describes the fabrication, characterization and testing of NbN/MgO/NbN superconductor-insulator-superconductor (SIS) tunnel junctions for use as heterodyne mixers in the submillimeter band (300-3000 GHz). The first section describes the importance of the submillimeter band in astronomy. In this frequency range, heterodyne detectors are used for detecting emission lines from atoms and molecules. Because of their extremely nonlinear current voltage characteristics, lead-based SIS junctions and more recently niobium-based SIS junctions are the most sensitive heterodyne detectors in the near millimeter band (100-600 GHz). NbN tunnel junctions are being developed as an alternative technology to lead-alloy tunnel junctions in order to extend the frequency range of SIS mixers to higher frequencies. To explain the physics of SIS mixers, an overview of superconductivity is given. The properties of an SIS tunnel junction are then described based on this overview. A quantum mechanical theory, which describes radiation detection using SIS junctions, is presented, and the basic physics and predictions of this theory discussed. Properties of real SIS junctions are compared to the properties of an ideal SIS junction. The physical origin of these nonideal properties and their effect on mixer performance are discussed. Finally, the various superconducting materials that are available for use in SIS tunnel junctions are described. The advantages and disadvantages of each material are presented. The decision to develop NbN tunnel junctions is based on these factors.

A. Submillimeter Astronomy

In the submillimeter band, distant galaxies, cosmic background radiation and star formation in gas clouds within our own galaxy all provide important subjects for astronomical observation. Observations of gas clouds are particularly fascinating because many molecules have rotational transitions at submillimeter wavelengths. The emission and absorption spectra of these molecules yield information about their relative abundances, temperatures, and velocity distributions. These data are critical for understanding star formation and interstellar chemistry. A review of techniques in submillimeter astronomy is given by Phillips (1987).

Submillimeter Telescopes

Telescopes in the submillimeter band have only recently been constructed because of several technological difficulties at this frequency. These large radio-style telescopes must have surface accuracies of less than $20\mu m$, which is very hard to attain with traditional techniques. Detectors and oscillators that work at this frequency are difficult to construct. Finally, the atmosphere is nearly opaque in the submillimeter band. Until the recent construction of several telescopes, the Kuiper Airborne Observatory (KAO) was the only telescope dedicated to operating in the submillimeter band. This telescope is a small (0.9 m) dish mounted in a Lockheed C-141 aircraft. The plane flies at an altitude of 12 km, because at this altitude

the atmosphere is nearly transparent in the submillimeter band with the exception of several strong absorption lines. More recently, three ground- based telescopes (the James Clerk Maxwell 15 m telescope, the Caltech Submillimeter Observatory 10.4 m telescope and the Swedish-ESO 15 m telescope) have been constructed on mountain peaks. At mountaintop altitudes, the atmosphere is nearly transparent in parts of the submillimeter band. These telescopes have much larger collecting areas than the KAO, resulting in greater sensitivity and improved angular resolution. Additionally, several space missions (NASA's Large Deployable Reflector, and Submillimeter Explorer) have been proposed. New detector technologies need to be developed to take advantage of these new telescopes.

Heterodyne Detectors

At millimeter and submillimeter wavelengths, it is difficult to construct amplifiers. Instead, mixers are used to downconvert the high-frequency signal (RF) to a lower frequency, known as the intermediate frequency (IF), which can be amplified. Once the signal has been amplified, it can be processed further without adding noise. The combination of the mixer, IF amplifiers and subsequent signal-processing equipment is called a heterodyne receiver. Incoherent detectors can also be used at millimeter and submillimeter wavelengths. These detectors measure the signal power over a large bandwidth. Spectral information about the signal can be obtained by filtering the radiation prior to detection. The filters used typically do not have high frequency resolution. In contrast, heterodyne systems typically have very high frequency resolution. For astronomers, this means narrow molecular emission lines can be resolved.

In order to downconvert a high-frequency signal to an IF signal, the signal, together with a coherent local oscillator (LO), is applied to a diode. If the local oscillator power is large compared to the signal power, there will be output radiation at all frequencies $\nu = n\nu_{LO} \pm \nu_{signal}$, where n is an integer. The LO is typically at a frequency very near the signal frequency. The mixer is usually designed so that all of these frequencies are terminated reactively except the signal, LO, and intermediate frequencies, where the IF is $\nu_{IF} = |\nu_{signal} - \nu_{LO}|$. These signals are shown schematically in Figure 1.1. On millimeter wave telescopes, the center of the IF band is typically 1 to 2 GHz, although IF's up to 5 or 10 GHz are sometimes used. Mixers can respond to radiation that is at a frequency $\nu_{signal} = \nu_{LO} + \nu_{IF}$; this is called the upper sideband. Similarly, mixers can also respond to the lower sideband, which is at $\nu_{signal} = \nu_{LO} - \nu_{IF}$. All receivers downconvert both the upper and lower sidebands to the IF. If the response to both sidebands is equal, the receiver is called a double sideband reaceiver. If the response to one sideband is suppressed significantly relative to the other, the receiver is called a single sideband receiver.

In order to compare receivers, their response and sensitivity must be quantified. Consider an input

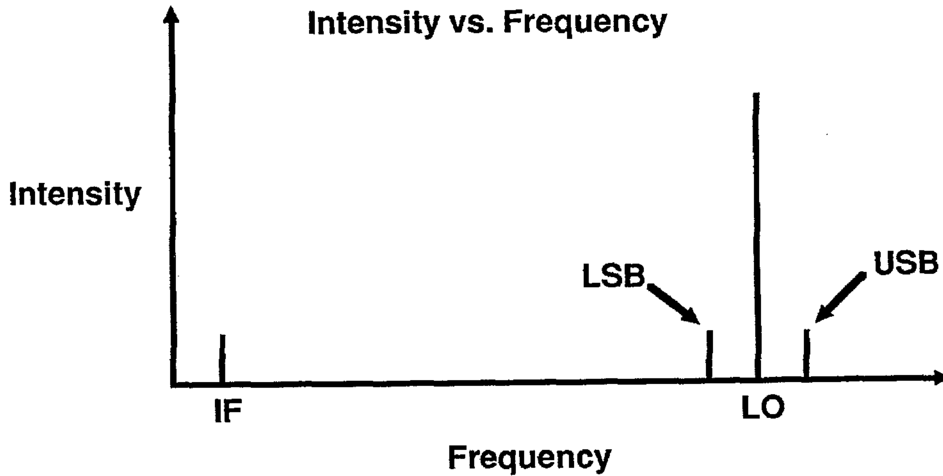

Figure 1.1 Schematic of upper and lower sideband, LO and intermediate frequencies.

signal of power P_{signal}, in a bandwidth B. For a linear mixer, the output power is

$$P_{output} = \eta(P_{signal} + P_{noise}), \tag{1.1}$$

where η is defined as the conversion gain of the mixer, and P_{noise} is the noise added by the mixer in a bandwidth B referred to the input of the mixer. Typically, the power-per-unit bandwidth added by the receiver is converted to an equivalent receiver noise temperature. This is defined as

$$T_r = P_{noise}/k_B B. \tag{1.2}$$

For most mixers, the conversion gain is less than unity. In this case, the IF signal is still very small, so the following IF amplifier will add noise to the system. The contribution of the receiver noise can be separated into the contributions from the mixer and the IF amplifiers,

$$P_{noise} = P_m + P_{IF}/\eta, \tag{1.3}$$

where P_m is the noise power added by the mixer, and P_{IF} is the IF amplifier noise power referred to the amplifier's input. Subsequent amplifiers will not degrade the signal, because the IF amplifier has significant gain. Equation 1.2 can be used to define the IF amplifier's equivalent noise temperature. At 4.2 K, a good IF amplifier has an equivalent noise temperature of 2 K. The details of measuring T_m, T_r, and η will be given in chapter three.

Most heterodyne mixers are based on semiconductor diodes, such as the Schottky diode. These devices have been used for mixers at submillimeter wavelengths; however, Schottky diodes have several disadvantages. Their inherent noise is fairly large, and their conversion gain is small. Both of these factors

will degrade the signal-to-noise ratio of the IF signal. Schottky diodes also require large LO power levels. At millimeter wavelengths, LO requirements are not a problem, because fundamental frequency, solid-state oscillators, like Gunn-effect diodes, have large output powers. At submillimeter wavelengths, solid-state local oscillators consist of a millimeter wavelength fundamental source and a semiconductor diode-based harmonic multiplier. These sources typically have very low output powers, which makes Schottky diode-based systems hard to implement. The next section describes an alternative technology, which is based on superconducting tunnel junctions.

B. SIS Mixers

Heterodyne systems based on SIS tunnel-junctions are an alternative to Schottky diode heterodyne receivers. An SIS tunnel junction consists of two superconducting electrodes separated by a thin insulating layer (typically 1-2 nm). Electrons in one electrode can tunnel through the thin insulator into the other electrode. Unlike Schottky diodes, SIS mixers require very low LO power levels. Additionally, SIS tunnel junctions are the lowest noise mixers in the near millimeter band.

This section discusses the basic physics behind SIS tunnel junction mixers. We begin with an introduction to superconductivity. The unusual density of states for the superconductor causes SIS tunnel junctions to have extremely nonlinear current voltage (I-V) characteristics. This extreme nonlinearity leads to several phenomena, which can be described only by using a quantum mechanical theory. This theory and these phenomena are described in detail. Experimental results with SIS mixers are presented last. These results verify the predictions of the theory.

Physics of SIS Tunnel Junctions

Superconductivity is caused by a small attractive force between conduction electrons in a metal. In a conventional superconductor, this attractive force is moderated by the electron-phonon interaction. Below the superconducting transition temperature (T_c), the electrons near the Fermi energy form bound pairs (Cooper pairs, Cooper 1956), because of this attraction. The Cooper pairs have a net spin of zero, so they act like bosons, not fermions. The pairs will condense into the ground state. These pairs can carry current without any dissipation of energy. A microscopic theory to explain this phenomenon was given by Bardeen, Cooper and Schrieffer (BCS, 1957). To create an excitation from the ground state, a Cooper pair is broken. The lowest energy states for the excited electrons is an energy Δ above the Fermi energy; therefore, the lowest excitation energy for the system is 2Δ, because there are two electrons in a Cooper pair. This excitation energy is called the superconducting energy gap. The density of the excited states as a function of energy is shown in Figure 1.2(a). There is an infinite density of states at the edges of the energy gap. The density of states shown in this figure is frequently called the semiconductor-picture of a superconductor. The Cooper pairs are not shown in this diagram; the pairs are at the Fermi energy. In

the ground state of the superconductor, all the electronic states below the energy gap are filled and all the electronic states above the energy gap are empty. The semiconductor picture of a superconductor is not a rigorous one, but an attempt to represent excitations of a many-body system in a simple manner. In a superconductor, the excitations are called quasiparticles. Quasiparticles act in most ways like electrons, but they have a finite lifetime and they will decay back into the pair states. An introduction to superconductivity is given by Tinkham (1975).

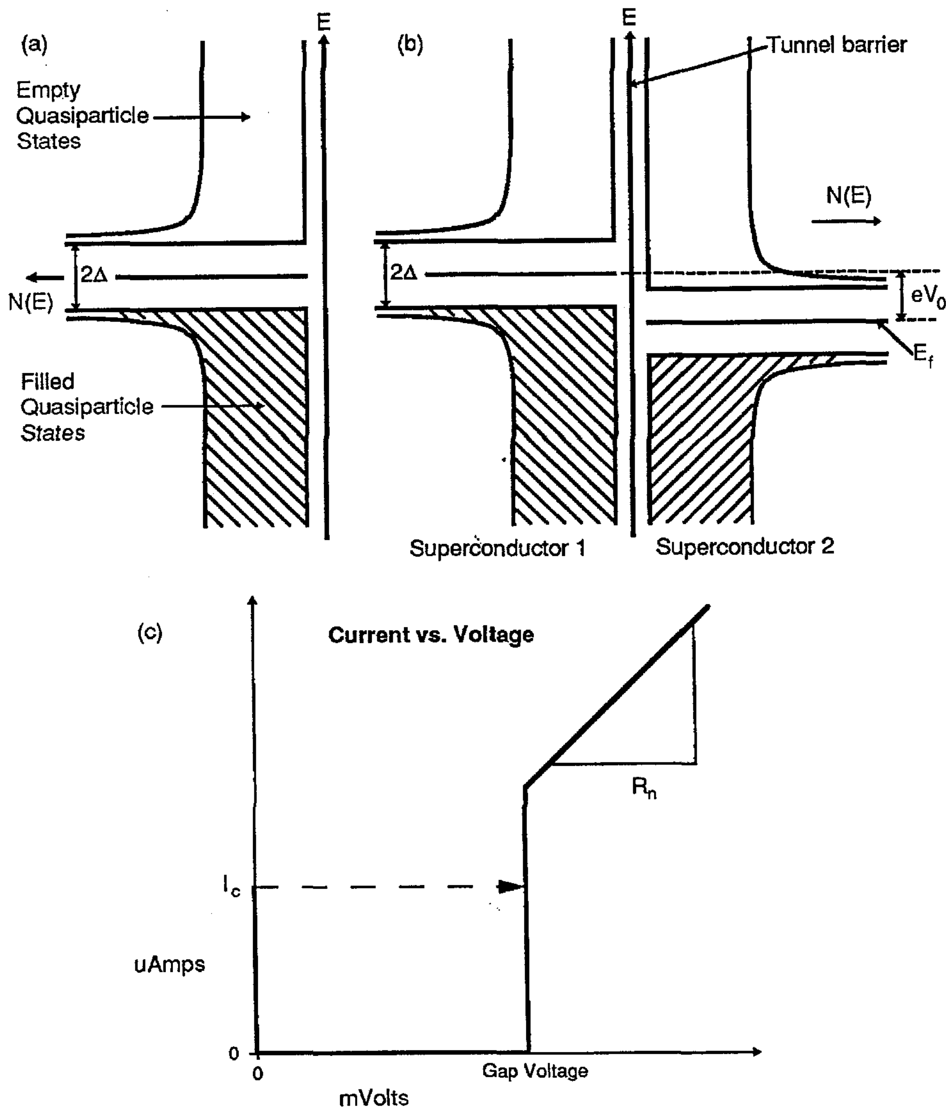

Figure 1.2 SIS Tunneling. Figure (a) shows the semiconductor picture of the BCS density of states at 0 K. Figure (b) shows the semiconductor picture of an SIS junction biased below the gap voltage. Figure (c) shows an ideal SIS I-V characteristic at 0 K.

The semiconductor picture can be used to understand SIS tunnel junctions. Figure 1.2(b) shows the semiconductor picture of an SIS tunnel junction biased at a voltage V_0. At this voltage, there are no empty

states for the quasiparticles in superconductor 1 to tunnel into. When the bias voltage is raised to the gap voltage ($V_0 = (\Delta_1 + \Delta_2)/e = \Delta_\Sigma/e$, where Δ_i is the energy gap for superconductor i), the filled states at the gap edge in superconductor 1 can tunnel into empty states at the gap edge in superconductor 2. The onset of tunneling current at this voltage is abrupt, because there are singularities in the density of states at both gap edges. Using the BCS expression for the density of states and the tunneling theories of Bardeen (1961) and Cohen *et al.* (1962), the I-V characteristic for a SIS tunnel can be calculated. This calculation involves determining the tunneling probability (T), which is equal to an overlap integral for the states on both sides of the barrier. All possible tunneling channels are summed over to obtain the total tunneling current for a given bias voltage. The I-V characteristic of a junction at 0 K is shown in Figure 1.2(c).

SIS tunnel junctions have nearly perfect I-V characteristics for heterodyne mixing. The optimal I-V characteristic for a classical mixer is a switch, which conducts no current below a certain bias voltage; above this bias voltage the current turns on abruptly. This happens in an ideal SIS I-V characteristic at the gap voltage. In real SIS junctions, the turn on of current is not perfectly sharp, but typically occurs over a fraction of a millivolt. The nonlinearity in an SIS tunnel junction is much sharper than the nonlinearity in semiconductor diodes ($\geq$10 mV for a cooled Schottky diode).

Quantum Theory of Mixers

When a tunnel diode has an extremely nonlinear I-V characteristic, classical mixer theory breaks down, and a quantum mechanical treatment is necessary. The frequency where classical theory fails depends on the voltage range over which the current is a nonlinear function. In SIS junctions, quantum mechanical effects have been experimentally observed at frequencies as low as 30 GHz (Face *et al.*, 1986). To explain these effects, a quantum mechanical theory for mixers was developed by Tucker (1975, 1979, 1983), Tucker and Millea (1978), based on the earlier theory of Werthamer (1966).

We will first apply Tucker's theory to the simple problem of direct detection of a coherent signal before considering the complete mixer theory. The figure of merit for a direct detector is the current responsivity (R_i), which is defined as the rectified current divided by the RF power absorbed. The current responsivity in a tunnel diode is

$$R_i = \frac{e}{h\nu}\left\{\frac{I_0(V_0 + h\nu/e) - 2I_0(V_0) + I_0(V_0 - h\nu/e)}{I_0(V_0 + h\nu/e) - I_{dc}(V_0 - h\nu/e)}\right\}, \qquad 1.4$$

where V_0 is the bias voltage, I_0 is the tunneling current, ν is the frequency of the radiation, e is the charge on an electron and h is Planck's constant. In the classical limit of small photon energies ($h\nu/e \ll \Delta V$, where ΔV is the voltage range over which the current is nonlinear), Equation 1.4 reduces to

$$R_i = \frac{1}{2}\frac{d^2I_0/dV_0^2}{dI_0/dV_0}. \qquad 1.5$$

This is the classical result for a square law detector. In the quantum mechanical limit of large photon energies ($h\nu/e \gg \Delta V$), Equation 1.4 reduces to

$$R_i = \frac{e}{h\nu}. \qquad 1.6$$

Tucker's theory predicts both the quantum result of one electron per photon absorbed (Equation 1.6) and the classical result for a power law direct detector (Equation 1.5). The important feature to notice is that the transition from classical to quantum mechanical behavior occurs when the voltage scale of the photon, $h\nu/e$, is comparable to the voltage range over which the current is a nonlinear function.

An informative picture of the quantum mechanical limit of direct detection in SIS junctions can be had by considering the semiconductor picture of SIS tunneling. Figure 1.3 shows the semiconductor picture of a tunnel junction biased just below the gap voltage. No current can flow at this bias voltage; however, if photons are incident on the tunnel junction, a quasiparticle can tunnel for each photon that is absorbed. Figure 1.3 shows the process of a photon being absorbed and an electron tunneling from superconductor 1 to superconductor 2. This process will occur, if the junction is biased at a voltage $h\nu/e$ below the gap voltage or at any higher bias voltage. If two photons are absorbed, tunneling can occur at bias voltages of $2h\nu/e$ below the gap voltage. Photon-assisted tunneling leads to a series of current steps in the I-V characteristic at voltages of $\Delta_\Sigma/e - nh\nu/e$, corresponding to the absorption of n photons. For bias voltages slightly less than the gap voltage, one electron can tunnel for each absorbed photon, which is the quantum regime discussed above.

Tucker also extends his quantum mechanical theory to the more complicated problem of heterodyne detection; his theory predicts several interesting phenomena. As noted above, steps should occur in the I-V characteristic of voltage width $h\nu/e$. For certain conditions, the regions between the steps will have negative differential resistances, and infinite conversion gain is available if the IF amplifier is matched to the junction. In a classical mixer, conversion gain must be less than one. The fact that SIS mixers can have conversion gains greater than one is very important, because it reduces the noise contribution of subsequent IF amplifiers to the receiver noise. The contribution of the IF amplifiers is typically a significant fraction of the system noise. Finally, the noise temperature of quantum mixers can approach the quantum limit imposed by the uncertainty principle (for a double sideband receiver, $T_{quantum\ limit} = h\nu/2k_B$) (Tucker, 1979; Wengler and Woody, 1987). The low inherent noise of SIS mixers coupled with the potential for conversion gain leads to very low receiver noise levels for these devices. All of these predictions have been experimentally verified in SIS mixers in the millimeter wave region (McGrath *et al.*, 1985; Face *et al.*, 1986; Pan *et al.*, 1989).

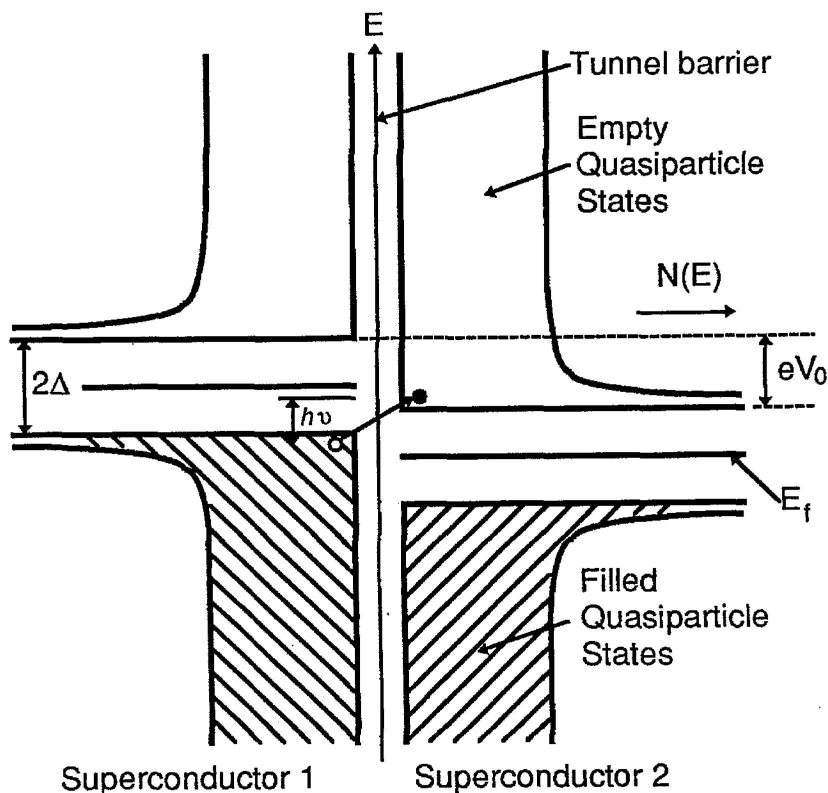

Figure 1.3 Semiconductor-picture of SIS photon assisted tunneling.

Experimental Results with SIS Mixers

Experimental results using SIS junctions as mixers first appeared in 1979 (Dolan, Phillips and Woody, 1979; Richards *et al.*, 1979; Rudner and Claeson, 1979). These early results showed extremely low noise temperatures and photon-assisted tunneling steps. Reviews on experimental results have been written by Tucker and Feldman (1985) and Phillips and Woody (1982). To date, SIS mixers have shown excellent performance from 30 to 230 GHz (Face *et al.*, 1986; Pan *et al.*, 1989; Ellison *et al.*, 1987). Mixer results above 230 GHz have been much more recent and fewer in number. Recent results of a waveguide receiver at 345 GHz by Ellison *et al.* (1989) are extremely good. At higher frequencies, two open-structure receivers have also given good results (Wengler *et al.*, 1985; Büttgenbach *et al.*, 1988). Performance of mixers at these higher frequencies have been limited by tunnel-junction characteristics.

SIS tunnel junction-based mixers require very low LO levels and are very sensitive, because they have extremely nonlinear I-V characteristics. The abruptness of the nonlinearity is caused by a singularity in the density of states at the gap edge. A theory to explain SIS mixers has been developed by Tucker. There are limitations on the performance of SIS mixers, particularly at higher frequencies. These limitations are caused by nonideal I-V properties and by the basic physics of superconductors. The properties and limits of real SIS tunnel junctions are discussed in the next section.

C. Properties of Real SIS Tunnel Junctions

The previous section discribed the performance of mixers using ideal SIS tunnel junctions; however, real SIS junctions have properties that limit their performance. This section analyzes these limitations and their physical origins. Figure 1.4 shows a stylized version of a real SIS I-V characteristic, as compared to the ideal I-V characteristic shown in Figure 1.2(c). The properties of this I-V characteristic are referred to throughout this section.

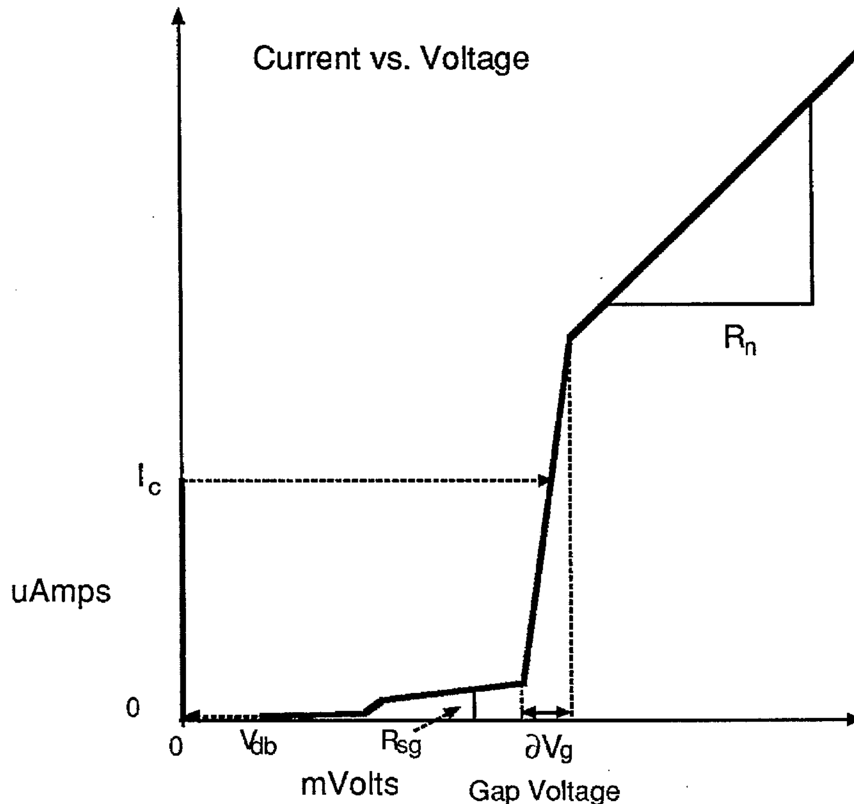

Figure 1.4 Stylized SIS I-V characteristic. This figure shows a stylized version of a real current versus voltage plot for an SIS tunnel junction. There is a finite subgap resistance (R_{sg}), a broadening of the onset of tunneling at the gap voltage (δV_g), and the drop-back voltage (V_{db}), below which there is no stable nonzero bias voltage. Additionally, there may be an increase in subgap leakage at half the gap voltage.

Rounding of Current-Voltage Characteristics

SIS-based mixers exhibit quantum behavior only when the I-V is extremely nonlinear. Real tunnel junctions have subgap leakage currents and a smeared turn-on of the tunneling current at the gap voltage. Both of these nonideal properties reduce the nonlinearity in an SIS I-V characteristic. Devices with rounded I-V characteristics will show quantum mechanical effects only at higher frequencies.

The most severe problem in I-V rounding is the gap smearing; it comes about because supercon-

ductivity is not a local phenomenon. In a superconductor the Cooper pair extends over a finite region. The size of the Cooper pair is the superconducting coherence length (ξ). Because of the finite size of the Cooper pair, the local energy gap of a superconductor is a weighted spatial average of the material in a volume ξ^3. Real superconductors are not spatially uniform, but have imperfections such as grain boundaries, impurities, crystal defects and nonstoichiometric material. If the size of these imperfections is small compared to the coherence length, the measured gap will be the spatial average of the local gap values. In this case, the gap voltage will be reduced, but the onset of tunneling at the gap voltage will be sharp. If the scale of imperfections is large compared to the coherence length, the measured gap will be reduced and will vary spatially. This leads to a smeared onset of tunneling at the gap voltage. To reduce gap smearing in short coherence length materials, it is necessary to deposit superconducting materials that are more nearly perfect crystals.

The second form of I-V characteristic rounding is subgap leakage currents. The BCS I-V characteristic in Figure 1.2 shows no sub-gap leakage currents, because the physical temperature is absolute zero. At finite temperatures, quasiparticles can be excited thermally, leading to subgap leakage currents. This leakage is very low for temperatures below $T_c/2$. In real junctions, there are finite subgap leakage currents even at very low temperatures (1.5 K). There are several possible sources of this "excess" leakage current. There can be holes in the barrier that lead to parallel bridge-type weak links. There can be normal metal regions in the the superconductor that lead to parallel, superconductor-insulator-normal metal (SIN) tunneling. There can be multiparticle tunneling events that lead to conduction below the gap voltage. The effects of these three mechanisms on the I-V characteristic are now discussed.

If there are pinholes in the barrier, there will be conduction through constricted superconductor-bridges. For a pinhole that is smaller than a coherence length, a bridge-type weak link is formed in parallel with the tunnel junction (Anderson and Dayem, 1964; Barone and Paternò, 1982). Junctions with parallel leakage through pinholes will usually have a nonhysteretic component to the critical current, because bridge-type weak links have nonhysteretic I-V characteristic. If pinhole conduction is large, the effect is obvious, as seen in Figure 1.5. Typically, junctions do not have large nonhysteretic components of the critical current. Pinhole conduction is probably not the dominant subgap leakage mechanism.

One characteristic frequently seen in leaky tunnel junctions is an increase in subgap conduction at half the gap voltage. This increase gives a clue to the physical mechanism of excess leakage current. The next two subgap conduction mechanisms lead to an increase in leakage currents at half the gap voltage.

If there are normal metal regions in one of the tunnel-junction electrodes, there will be SIN conduction. The normal regions need to be larger than an electronic coherence length, or they will only cause reduction in the gap voltage through the proximity effect. SIN I-V characteristics have a conductance maximum at

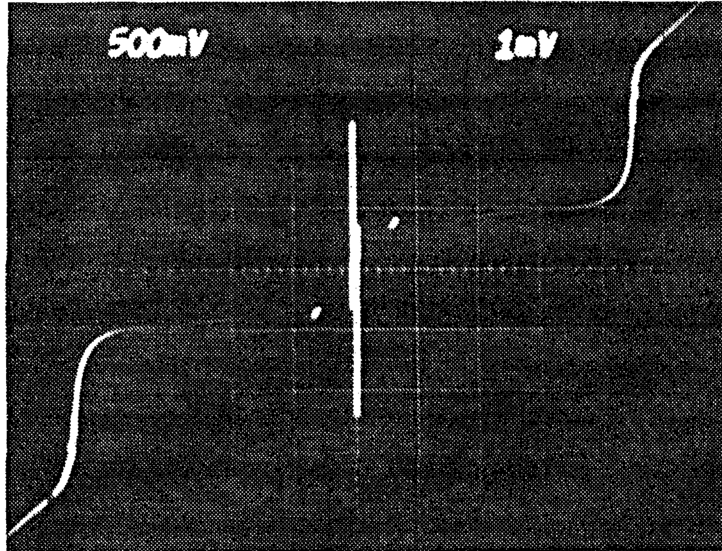

Figure 1.5 Leaky I-V characteristic. *This tunnel junction shows extreme parallel leakage currents through a Josephson weak link.*

half the gap voltage and can explain the increase in subgap current at half the gap voltage.

If the barrier is thin, there will be conduction below the gap voltage through multiparticle tunneling processes. In a multiparticle tunneling process, two or more quasiparticles tunnel simultaneously. Theories for multiparticle tunneling were first proposed by Taylor and Burstein (1963) and by Schrieffer and Wilkins (1963). Two-particle tunneling is shown schematically in Figure 1.6. A typical two-particle tunneling event occurs for a bias voltage of half the gap voltage. A Cooper pair at the Fermi energy breaks, and the two quasiparticles tunnel into the empty states in the other electrode. This process is proportional to the transmission probability squared (T^2), because two particles must tunnel simultaneously. Two-particle tunneling creates a current rise at half the gap voltage, explaining qualitatively the subgap leakage currents. Three-particle tunneling can occur if three quasiparticles tunnel simultaneously. The effects of multiparticle tunneling on NbN/MgO/NbN junctions will be analyzed in Chapter three.

High-Frequency Limits on SIS Mixers

The high-frequency roll-off of the detection efficiency for an SIS tunnel junction is limited by two of its properties. The junction capacitance acts to short out the signal at high frequencies, and the superconducting energy gap limits performance through two mechanisms at high frequencies. Both of these effects are now discussed.

The two electrodes and the barrier of a tunnel junction form a parallel plate capacitor; this capacitor forms a low pass filter with the tunneling resistance. The capacitance acts to shunt signal current away from

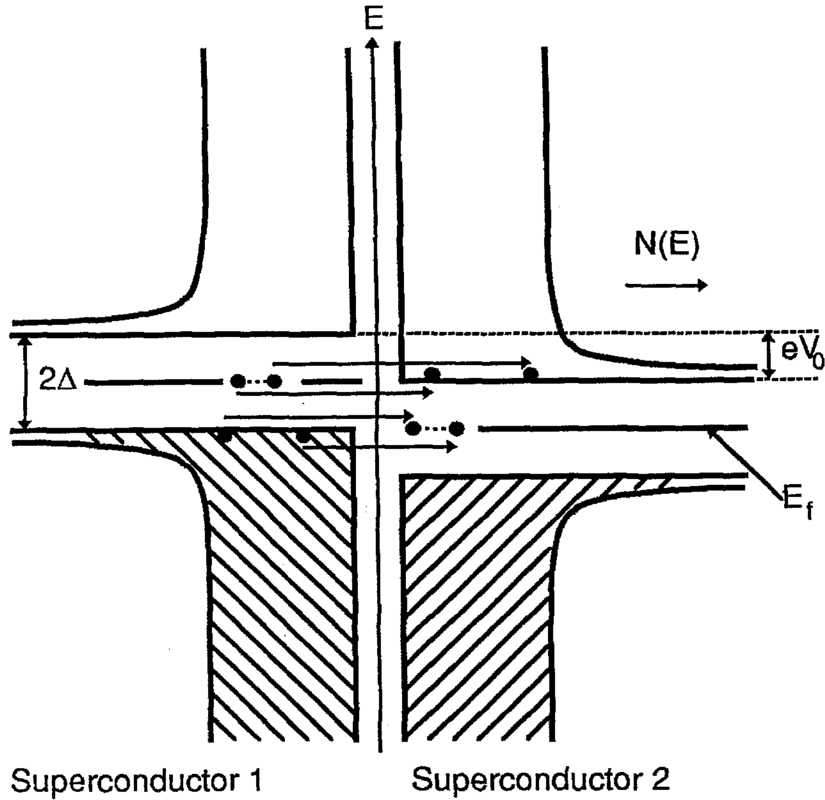

Figure 1.6 Semiconductor-picture of multiparticle tunneling.

the nonlinear tunneling element. When calculating the "RC" speed of a junction, the correct resistance to use is the junction-radiation input resistance, which depends on the junction bias conditions. The junction-radiation input resistance is of the same order as the normal-state-tunneling resistance, as is noted by Tucker and Feldman (1985). In this thesis, the normal state resistance is used to calculate RC speed. The junction capacitance is

$$C = \epsilon A/d, \quad 1.7$$

where ϵ is the barrier dielectric constant, A is the junction area, and d is the barrier thickness. For a simple square barrier, the junction normal state resistance is

$$R_n = \frac{h^2 d}{e^2 A\sqrt{2m\phi}} \times \exp\left(4\pi d\sqrt{2m\phi}/h\right), \quad 1.8$$

where ϕ is the barrier height, m is the mass of the electron, h is Planck's constant, and e is the charge of an electron. Several things are clear about the R_nC product: It does not depend on the junction area, because the resistance and capacitance vary in an inverse manner with area; the RC speed varies with barrier thickness as $\exp(-d/d_0)$, because the linear thickness terms in the capacitance and the resistance cancel out. High-speed junctions will have thin tunnel barriers and small R_nA products. The impedance of the mixer mount is roughly 100 Ω. To obtain impedance-match, the junction impedance must be roughly

100 Ω, so the junction area must be small. If materials with reduced barrier heights or dielectric constants are used, R_nC products will improve.

The second limitation on high-frequency performance is the energy gap. For $h\nu \geq 2\Delta$, photon energies are large enough to break Cooper pairs and create excited quasiparticles. Above this gap frequency, the resistivity of the superconductor is roughly equal to its normal state resistivity. This implies that antenna and transmission line circuits will be lossy and will not act in an ideal manner. At twice this frequency, the junction is no longer an efficient mixer. Consider a junction biased just below the gap voltage. For $h\nu \geq 4\Delta$, photon energies are large enough that photon-assisted tunneling can take place in both the forward and reverse bias directions. At this frequency, the tunnel junction no longer acts as a rectifier, and it is not an efficient mixer. Tests have been made of Pb mixers at frequencies above $2\Delta/h$ with good success (Büttgenbach *et al.* 1988). This means that although superconductors are lossy at frequencies above $2\Delta/h$, SIS junctions still exhibit mixing.

Josephson Tunneling in SIS Junctions

Both quasiparticles and Cooper pairs can tunnel in an SIS tunnel junction. The effects described so far are quasiparticle tunneling. This is the effect that is typically used in mixers. Cooper pairs can tunnel coherently across the barrier. Pair tunneling is called the Josephson effect (Josephson 1962, 1965). A review on Josephson tunneling and its applications is given by Barone and Paternò (1982).

For the small area junctions used in quasiparticle mixers, two simple equations describe the Josephson effect. These equations are derived in Appendix A and are:

$$I = I_c \sin(\phi) \text{ and} \qquad 1.9$$

$$V = h/2e \times d\phi/dt,$$

where ϕ is difference in the macroscopic phase of the superconductor wave function across the barrier, and I_c is a constant determined by the barrier and the area of the junction. The most obvious effect of Josephson tunneling is the finite current at zero voltage. At zero voltage, ϕ can take on any constant value, and the current can vary between $+I_c$ and $-I_c$. The Josephson supercurrent is the dissipationless tunneling of pairs across the barrier. A second effect is that if the junction is biased at a DC voltage (V_0), $\phi = \phi_0 + 2eV_0t/h$, the current will oscillate at a frequency $\nu = 2eV_0/h$. The Josephson oscillations are just one of a wealth of phenomena caused by Josephson tunneling.

The Josephson effect causes two problems in SIS quasiparticle mixers. Below a certain voltage, V_{db} (called the drop-back voltage), there are no stable DC bias points, and the junction switches to the zero-voltage state. The Josephson effect can be used for heterodyne mixing. Josephson mixing can interfere with quasiparticle mixing and cause increased mixer noise. These two phenomena are described.

The drop-back voltage is caused by the Josephson oscillations. At a small bias voltage, the voltage amplitude of the Josephson oscillations is larger than the bias voltage. The zero voltage state is a lower energy state than the finite voltage state, so the junction switches to the zero-bias state. At larger bias voltages, the oscillations are at high frequencies and will be shunted out by the junction capacitance; therefore, large bias voltages will be stable. As the bias voltage is reduced, the voltage amplitude of the oscillations increases. At the drop-back voltage, the voltage amplitude of the oscillations is roughly equal to the bias voltage. The value of the drop-back voltage can be calculated analytically to be

$$V_{db} \approx \sqrt{\frac{\hbar I_c}{4\pi C}}, \qquad 1.10$$

(Johnson, 1968). High-speed junctions, which have small RC products, will have large drop-back voltages. If the local oscillator causes the ac bias to enter this unstable drop-back region, the mixer will be very noisy. The addition of noise to SIS mixers from the Josephson effect has been studied by Dolan *et al.* (1981) and Rudner *et al.* (1981a, 1981b).

The Josephson effect can be used to detect radiation. When an RF signal is applied to a Josephson junction, steps appear in the I-V characteristic at voltages proportional to the frequency ($V_n = nh\nu/2e$, Shapiro 1963). The heights of the steps is a function of the RF power level, so the current level between steps is a function of RF power. The Josephson effect, like quasiparticle tunneling, can be used for direct detection and mixing. For typical LO power levels, only the first few Josephson steps are evident. At low frequencies, these steps are at low voltages and do not interfere with quasiparticle mixing; at high frequencies, the steps are spaced further apart, and they are in the typical bias range for quasiparticle mixing. The details of the interaction of Josephson mixing with quasiparticle mixing are not fully understood; however, if Josephson steps are present near the bias region, noise levels are typically higher than normal.

A magnetic field can be applied to suppress the Josephson effect. This reduces problems with the drop-back voltage and Josephson mixing. To fully suppress the Josephson effect, one-half of a quantum of magnetic flux ($\Phi_0/2 = h/4e$) should be threaded through the barrier region. The magnetic field necessary to suppress the Josephson effect is roughly $B = \Phi_0/2t(d + 2\lambda)$, where t is the length of the junction, d is the barrier thickness and λ is the magnetic penetration depth. (The penetration depth is discussed further in chapter three.) For a $0.5 \times 0.5\mu m^2$ junction with a penetration depth of 300 nm and a barrier that is 1 nm thick, the magnetic field needed is 3×10^{-3} Tesla. Experimentally, the magnetic field can be large enough to suppress the gap and degrade the I-V characteristic (Wengler 1986). Junctions with larger gap voltages will have fewer problems with the drop-back voltage and Josephson mixing, because the typical bias voltage (just below the gap voltage) is larger.

Real SIS tunnel junctions have many properties that will limit mixer performance. These limitations

can be put into four general categories: rounding of the I-V characteristic, high-frequency roll-off from the junction capacitance, the high-frequency limit imposed by the superconducting energy gap and problems caused by the Josephson effect. All of these limitations depend on the properties of the superconductor and the barrier. The next section describes several different materials that can be used to fabricate SIS tunnel junctions.

D. Materials Choices for SIS Mixers

There is a large range of materials that can be used for SIS mixers. The desired properties for an SIS tunnel junctions used as a submillimeter mixer are now summarized, so that these materials can be evaluated. The junction capacitance should be small; therefore, barriers of low dielectric constant, low barrier height materials are advantageous, and submicron low R_nA product junctions are needed. The energy gap of the superconductor should be large to avoid losses in the superconductor and to reduce the effect of the drop-back voltage. The transition temperature should be large (15-20 K), so that closed-cycle refrigerators can be used to cool the junctions. The junctions should survive thermal cycling and long periods of storage, because rugged junctions are more convenient for use in practical instruments. Finally, the I-V characteristics need not be as sharp as they would be at lower frequencies to reach the quantum mechanical regime. The advantages and the disadvantages of the various superconductors will be discussed in this section. It will become clear that no single material satisfies all these requirements, and trade-offs need to be made.

Lead Tunnel Junctions

The SIS tunnel junctions simplest to fabricate are made of lead (or lead-alloy) electrodes with native oxide tunnel barriers. The first SIS junctions ever fabricated were of this type (Giaever, 1960). Lead junctions are easy to fabricate for several reasons. Lead is a low-melting-point material, so thermal evaporation from a resistively heated source can be used to deposit it. Impurities in lead films typically do not degrade the film quality. This is because the electronic coherence length is large (83 nm, Kittel, 1976) relative to other materials, and impurities can at worst degrade the average properties of the film. Additionally, many lead alloys have higher transition temperatures than pure lead (the T_c of pure lead is 7.2 K and the T_c of lead-bismuth is 9.3 K). Lead junctions use a native-oxide tunnel barrier, which is easily formed by exposing the base electrode to a controlled oxygen atmosphere. Finally, a great deal is known about lead-alloy junction fabrication which was developed significantly during the Josephson supercomputer effort at IBM.

There are a number of advantages to using lead-alloy tunnel junctions as mixers. Small-area tunnel junctions can be fabricated. Dolan (1977) developed a technique for making submicron lead-alloy junctions: Using optical lithography, a hanging photoresist bridge is made; the lead electrodes are evaporated at an

angle under the bridge to form a submicron overlap junction. The specific capacitance of PbInAu junctions is very low (c=45×10^{-15} F/μm^2 at J_c=6000 A/cm^2, Baker and Magerlein 1983). The onset of tunneling in lead junctions is sharp, because the electronic coherence length is large. For these reasons, lead-alloy junctions have been used to date on most SIS mixers. At high frequencies in particular, lead junctions have given all the best mixer results, because they have a small specific capacitance, and submicron junctions can be fabricated easily.

Lead junctions have several problems. The largest arises from the soft nature of lead. Upon thermal cycling, hillocks form in the lead-base electrode to relieve thermal stress in the lead film. These hillocks can puncture the barrier, destroying the junction. Additionally, tunnel-junction properties may change with time, if the junctions are not stored at cryogenic temperatures. Finally, lead-alloy junctions have small gap voltages and small transition temperatures ($V_g \approx 2.7$ meV, $T_c \approx 8.5$ K). Because the transition temperature is small, lead junctions must be cooled below 4.2 K to approach the zero Kelvin gap voltage and reduce thermal leakage currents.

Nb/oxide/Pb Tunnel Junctions

Tunnel junctions can be fabricated with a Nb base electrode, a native oxide tunnel barrier and a Pb counter electrode. This type of junction was also developed at IBM for the Josephson supercomputer effort. The fabrication technique for these junctions is as follows. A Nb layer is deposited (typically by sputtering), and the film is etched using a photoresist stencil to define the Nb electrode area. Next, an insulating layer, with windows for the junction areas, is lifted off using a photoresist stencil. The samples are returned to the vacuum system, the Nb is cleaned using an ion mill, the Nb is oxidized to form the tunnel barrier, and a lead counter electrode is deposited. Kleinsasser and Buhrman (1980) altered this technique so that the junction area was defined on the edge of the Nb film. In this way junction areas can be made very small, because the Nb can be very thin. Edge-junctions of 0.1 μm^2 area or smaller can be fabricated using optical lithography.

The problems with Nb/oxide/Pb junctions arise from the oxide barrier. There are several stable oxides of niobium. The different oxides are a low T_c superconductor, a semiconductor and an insulator. When the oxide barrier is formed, all of these niobium-oxides will be present, making the superconductor-barrier interface poor. Additionally, the insulating phase (Nb_2O_5) has a dielectric constant of 30. The large dielectric constant makes the specific capacitance large (c=150 fF/μm^2, for a critical current density of 6000 A/cm^2, Baker and Magerlein 1983). This means that the RC product, even for a thin barrier, is high for these junctions. One additional problem is that junction resistances can increase with time.

Nb/oxide/Pb junctions have several advantages. These junctions do not have problems with hillock formation like Pb junctions, because the base layer is refractory. Nb/oxide/Pb junctions will survive cycling

between 4.2 K and 300 K. Additionally, junctions with submicron areas can be fabricated easily, using the edge-geometry. The small area of edge-junctions helps compensate for the large specific capacitance. The gap voltage and transition temperature of Nb/oxide/Pb junctions is only slightly larger than Pb junctions; however, NbN/oxide/Pb edge-geometry junctions have been fabricated (Letrou *et al.*, 1987; Meng *et al.*, 1989). These junctions have larger gap voltages (Δ_Σ=4.0 meV) than Pb/Pb or Nb/Pb junctions.

Nb/Al-AlO$_x$/Nb Tunnel Junctions

Two types of all refractory SIS junctions with good I-V characteristics have been fabricated. One, NbN/MgO/NbN, is the topic of this thesis. The other, Nb/Al-AlO$_x$/Nb, was developed by Gurvitch *et al.* (1983). This type of junction is made by first depositing the junction trilayer (Nb/Al-AlO$_x$/Nb) in a single vacuum deposition. The niobium and aluminum are typically sputtered. The barrier is formed by depositing an aluminum overlayer and thermally oxidizing the overlayer. The resulting Al_2O_3 barrier has much better properties than native niobium oxide, because there is only one stable oxide, and the relative dielectric constant is lower (ϵ_r = 10). The junction area and surrounding circuit are defined after the trilayer is completed. Chapter two describes the trilayer junction process in detail. This deposition and fabrication process is straightforward; many groups in this country and in Japan have made Nb/Al-AlO$_x$/Nb junctions.

Nb/Al-AlO$_x$/Nb junctions have several important advantages over Pb junctions. The I-V characteristics are extremely sharp. The subgap leakage of these junctions is very low (the subgap to normal state resistance ratio is as large as 100), and the gap width is small (0.2 mV). The thermal stability of these junctions is very good, and they can be stored at room temperature without any degradation of the I-V characteristic. Additionally, the run-to-run uniformity of these junctions is excellent. This uniformity is advantageous in designing complicated mixer circuits.

Nb/Al-AlO$_x$/Nb junctions should make excellent mixers in the millimeter band. The main problem with these junctions is in fabricating small area junctions. Fabrication of submicron junctions using the trilayer process is difficult. The specific capacitance of Nb/Al-AlO$_x$/Nb junctions may be somewhat larger than Pb junctions. Preliminary measurements on Nb/Al junctions at JPL indicate the specific capacitance is 50 fF/μm^2 for a critical current density of 4000 A/cm^2. The specific capacitance of PbInAu junctions has been reported to be 25 to 45 fF/μm^2 for comparable junctions. The larger area and possibly larger specific capacitance of Nb junctions relative to PbInAu junctions has made testing of these junctions as mixers at high frequencies difficult. Recently there have been several promising mixer results with Nb/Al/Nb junctions (Tsuboi *et al.*, 1987; Inatani *et al.*, 1987; Kerr *et al.*, 1990)

Nb/Al-AlO$_x$/Nb junctions have excellent physical and electrical properties; however, the gap voltages of these junctions are only 2.8 meV, so the Nb will be lossy above 700 GHz. Additionally, submicron Nb junctions must be fabricated for high-frequency tests. Considering all the advantages offered by these

junctions, it is likely that mixers in the near-millimeter band will use Nb/Al-AlO_x/Nb junctions.

Niobium and Vanadium Compound Superconductors

The materials discussed so far do not have significantly larger energy gaps or higher transition temperatures than lead-alloy junctions. Compounds of niobium and vanadium can have larger energy gaps and transition temperatures than pure niobium or lead alloys. There are two general classes of materials: a group with the A15 crystal structure and another with the B1 crystal structure, which is the NaCl structure, or a face-centered cubic lattice. The largest gaps and transition temperatures of nonoxide superconductors are exhibited by A15 materials. Nb_3Ge has a transition temperature of 23 K. Both the A15 and the B1 superconductors are metastable at room temperature; however, experimentally it has proven easier to deposit B1 superconductors. Both classes have short electronic coherence lengths ($\xi \approx 4$ nm). As discussed previously, this leads to gap smearing in tunnel junctions. Early attempts at fabricating Nb-compound based tunnel junctions resulted in I-V characteristics with large subgap leakage currents and reduced gap voltages. B1 materials are the prime candidates for higher T_c Nb-based tunnel junctions, because they are easier to deposit than A15 materials.

NbN Films and Tunnel Junctions

NbN has one of the largest transition temperatures (17 K) for B1 materials. For this reason, much of the work in fabricating Nb compound superconductors has been focused on NbN. The energy gap for NbN is as large as 6.18 meV (Gurvitch *et al.*, 1985). Unfortunately, like most compound Nb materials the electronic coherence length is small ($\xi = 3 - 5$ nm). Another potential problem with NbN is its large magnetic penetration depth ($\lambda = 280 - 400$ nm). The magnetic penetration depth and its effect on circuits will be discussed at length in Chapter three.

A large number of barrier materials have been tried with NbN: native oxide (Shoji *et al.*, 1983; Villegier *et al.*, 1985), hydrogenated amorphous silicon (Shinoki *et al.*, 1981; Cusauskus *et al.*, 1983), metallic overlayers of Mg and Al (Braginski *et al.*, 1986), aluminum oxide (Talvacchio and Braginski, 1987) and magnesium oxide (Shoji *et al.*, 1985). All these barriers except MgO have had little success, in that junctions were very leaky, and the gap voltages were reduced from the expected value of greater than 5 meV.

The problem in fabricating NbN tunnel junctions is caused by the short electronic coherence length and the fact that NbN is metastable. The short coherence length means that the NbN has to be in the superconducting phase within 4 nm of the barrier. Typically, NbN begins to grow in a tetragonal phase, which has a lower energy gap. The B1 phase must be stabilized at the barrier-counter electrode interface to avoid reduction of the gap voltage by this tetragonal phase. MgO helps stabilize the B1 phase by acting as a template for epitaxial NbN growth. This growth will be discussed in the next chapter. MgO is the only

barrier material that has worked well with NbN. Unfortunately, the specific capacitance of NbN/MgO/NbN junctions is roughly twice that of PbInAu junctions (c=80 fF, Shoji *et al.* 1985).

NbN/MgO/NbN junctions are being developed for use as submillimeter band mixers. The choice of NbN is based on several trade-offs. NbN has the advantage of a large energy gap and a high T_c, as compared to Nb or Pb. The larger gap of NbN will allow for operation of mixers up to 1200 GHz. NbN junctions are stable with respect to time and thermal cycling. There are several problems that need to be addressed if NbN junctions are to be used as high-frequency mixers. The specific capacitance of NbN/MgO/NbN junctions is larger than PbInAu junctions. To reduce the junction capacitance, submicron junctions need to be fabricated. This can be done either by using an edge-geometry or by using electron-beam lithography to define the junction area. I-V characteristics of NbN/MgO/NbN junctions are more rounded than Pb junctions, because of the short coherence length. This thesis attempts to address these problems and to determine the feasibility of NbN/MgO/NbN submillimeter band SIS mixers.

Chapter II. Device Fabrication

This chapter describes techniques used to deposit NbN films and NbN/MgO/NbN tunnel junctions. Several methods have been used by others to deposit NbN films; the relative merits of each method are discussed. We use reactive magnetron sputtering to deposit NbN. The parameters we use to obtain high-quality NbN are presented. Tunnel junctions are fabricated by sequentially depositing NbN, MgO and NbN over an entire wafer. This is called the junction trilayer. MgO is the only barrier material to date that yields high-quality NbN tunnel junctions, because MgO grows epitaxially on polycrystalline NbN films. The importance of this growth mode is discussed. The process used to define individual junctions from the trilayer is reported. This includes overviews on reactive ion etching and ultraviolet photolithography. For high-frequency mixers, submicron junctions are needed. The current limitations in fabricating submicron NbN/MgO/NbN are described.

A. NbN Deposition

The goal in depositing NbN is to obtain the correct stoichiometry and crystal structure. The high-temperature superconducting phase of NbN has a B1 crystal structure, but the stable phase at room temperature has a tetraganol crystal structure. Above 1400° C, the B1 phase is stable, so stabilizing the B1 phase is much easier at elevated temperatures. A wide range of techniques have been used to deposit NbN at substrate temperatures in excess of 1000° C. These techniques are not useful for tunnel-junction fabrication, because the barrier will not survive these high temperatures. Two forms of sputtering have been used to deposit superconducting NbN on unheated substrates. Sputtering is a form of physical vapor deposition that involves dislodging material from a target with accelerated ions. We use reactive magnetron sputtering to deposit NbN films. The vacuum system and methods used to deposit high-quality NbN films are described.

NbN Deposition Techniques

Three methods of depositing NbN at very high substrate temperatures ($T_s \geq 1000°$ C) are nitridation of Nb films, chemical vapor deposition and reactive evaporation. The simplest method of deposited NbN is nitriding niobium films at 1400° C in an ultrapure nitrogen atmosphere (Gurvitch *et al.*, 1985). Very high-quality films can result from this process (T_c = 17.2 K), because the B1 phase of NbN is stable at this temperature. The characteristics of these films will be used as a reference point throughout this thesis for analyzing NbN properties. Several other methods use substrate temperatures of 1000° C. High-quality NbN films have been deposited by chemical vapor deposition ($T_c \approx 15.5$ K, Oya and Onodera, 1970, 1974). Reactive evaporation of Nb in an NH_3 atmosphere has also been used to deposit NbN (Serling, 1972). The quality of the films deposited using reactive evaporation was not exceptional ($T_c \approx 13.5$ K).

Sputtering is a form of physical vapor deposition. In the sputtering process, the deposited material

is dislodged from a pure target through momentum transfer by accelerated ions (typically argon or xenon, because they are heavy and inert). The dislodged material (atoms, compounds or atomic clusters) deposits on a nearby substrate. Using the sputtering process, high-quality films have been deposited onto unheated substrates. This makes sputtering a much more attractive process for tunnel-junction fabrication. The two forms of sputtering that have been used to deposit NbN are ion beam sputtering and reactive magnetron sputtering.

In ion-beam sputtering, a beam of ions from a Kauffman source bombards a Nb target. The Kauffman source produces ions by flowing a gas past a hot cathode. The ionized gas is accelerated, using a series of grids at high voltages. The ion-optics is designed to give an unfocused beam (typically 1" in diameter). The accelerated ions eject atoms from a target, the atoms then deposit on a substrate. NbN can be deposited by ion-beam sputtering (Lin and Prober, 1987). The Nb atoms are ejected from a pure Nb target. Nitrogen is incorporated in the film either by including nitrogen in the first ion beam, or by directing a second low-energy nitrogen ion beam at the substrate. NbN tunnel junctions have been fabricated using ion-beam sputtering; however, the NbN film and the device quality were not exceptionally good (T_c = 12 K).

Magnetron sputtering can also be used to deposit NbN. Figure 2.1 shows a schematic of the magnetron sputtering process. In this method, a negative bias (-V) is applied to a Nb target. The vacuum chamber is filled with an inert heavy ion (usually argon). The target is backed by fixed magnets, so a plasma can be confined at relatively low pressures. Typically, magnetron sputtering is done between 1 and 100 mTorr. Once a plasma has been struck, positive ions are accelerated towards the negatively biased target. These ions eject Nb atoms into the plasma. Subsequently, the Nb atoms condense on the substrate and chamber walls. If nitrogen is present in the plasma, it will react with the Nb at the target, substrate and chamber walls to form NbN_x. This is called reactive magnetron sputtering; it has been used by many groups to deposit NbN (Mitsuoka *et al.*, 1968; Gavaler *et al.*, 1969; Wolf *et al.*, 1980). Magnetron sputtering can be used to deposit the metastable B1 phase of NbN on unheated substrates, because the atoms in the plasma can have a much higher effective temperature than the substrate. Transition temperatures of films deposited this way are as high as 17 K. A good general reference for magnetron sputtering techniques is given by Hoffman and Thorton (1977).

Ion-beam sputtering has the advantage over magnetron sputtering of being a directional deposition process. Magnetron sputtering is done typically at 10 mTorr. At this pressure, the Nb atom will have many collisions before reaching the substrate, because the mean free path is 0.3 mm. The collisions randomize the atom's velocity, so the process is not significantly directional. Ion-beam sputtering is done at 10^{-4} to 10^{-5} Torr. At this pressure, the Nb atom will traverse the several centimeters to the substrate without a collision, so the deposition is directional. Directional deposition allows the use of shadowing

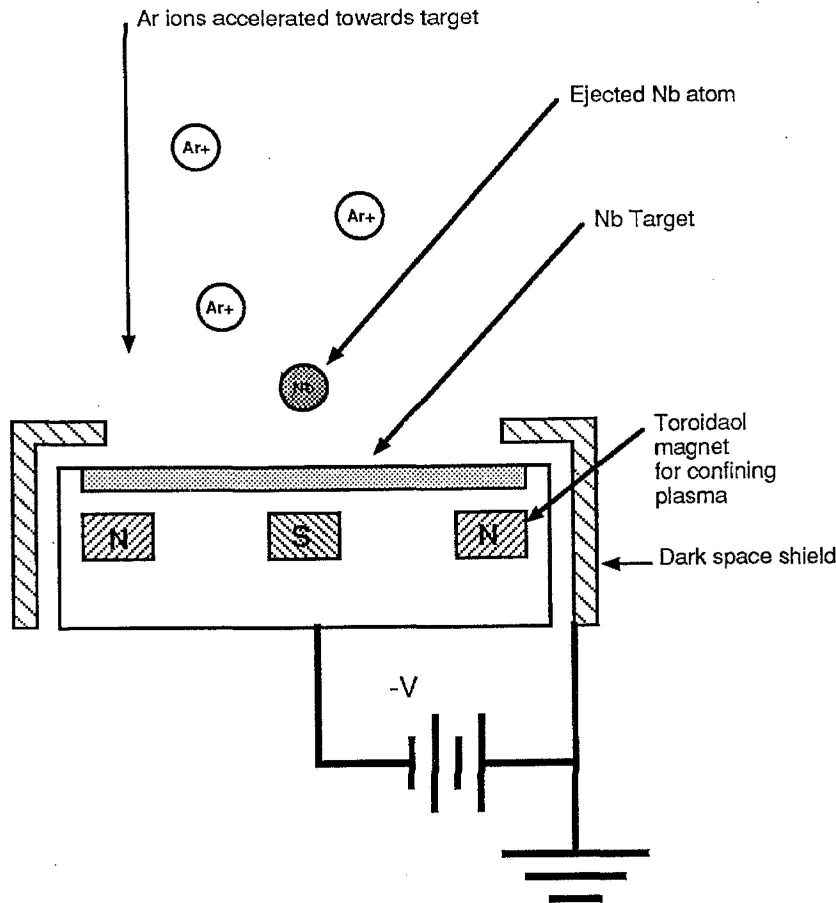

Figure 2.1 Schematic diagram of magnetron sputtering.

techniques to pattern films. These techniques can be particularly useful in defining small features. This advantage is offset by the lower quality of these films and devices.

Stabilization of the B1 Phase

High-quality NbN can be deposited using magnetron sputtering; however, the B1 phase is difficult to stabilize. Several methods have been used to obtain high-transition temperature films. Methane can be introduced into their gas mixtures to get NbC_xN_y films (Cusauskus, 1983 and Bacon *et al.*, 1983). NbC_xN_y films can have slightly higher transition temperatures than NbN, and they are easier to stabilize. A substrate with the same lattice spacing as NbN can be used to promote epitaxial growth of the B1 phase. MgO and Al_2O_3 crystalline substrates were used to promote epitaxial growth of NbN (Gavaler *et al.*, 1986).

NbN quality is very strongly influenced by the substrate temperature during film growth. The following observations are based on work in our lab. NbN films that are deposited on unheated substrates typically have transition temperatures of 14 to 15 K; NbN films that are deposited at higher substrate temperatures (200 to 300° C) have transition temperatures of 15 to 16 K; NbN films that are deposited at still higher substrate temperatures (400 to 600° C) have transition temperatures of 16 to 17 K. At higher substrate

temperatures, sapphire or MgO substrates need to be used to avoid interaction between the NbN film and the substrate. This trend in transition temperature as a function of substrate temperature is similar to that seen by Gavaler *et al.* (1986), although their transition temperatures were generally lower than ours. Films with transition temperatures of 16 K can be deposited on unheated substrates (Thakoor *et al.*, 1985), but the range of sputtering conditions that will yield high-quality films is extremely small, and most films will have lower transition temperatures. During the sputtering process, electrons from the plasma will bombard the substrate if it is electrically grounded. This electron bombardment will heat the substrate, particularly during long sputter depositions. This type of unintentional substrate heating will also improve film quality.

One of the effects of substrate heating is to increase NbN grain size. The larger grain size leads to better quality films, because the grain boundaries occupy a smaller fraction of the films. As was discussed in Chapter one, defects such as grain boundaries cause spatial variation of the energy gap in NbN. As the grain size increases, the surface roughness at the grain boundaries increases. Covering a rough surface with a 1 nm barrier can be difficult. Figure 2.3 shows a cross-sectional transmission electron micrograph of a NbN/MgO/NbN junction deposited on a sapphire substrate. The temperature of the substrate was 400° C, during the base layer deposition. The grain size in this film is roughly 30 nm, and the roughness of the surface is roughly 7 nm. Depositing tunnel junctions on heated substrates leads to better devices, but if the barrier is thin, the resulting junctions are usually short-circuited by holes in the barrier. Results of depositing junctions on heated substrates are discussed further in Chapter three.

Substrate Materials and Preparation

The substrate on which NbN is deposited can affect the quality of NbN film. An exception to this is films that are deposited on unheated substrates. In this case, glass, quartz, sapphire and Si (both oxidized and unoxidized) give equally high transition temperatures and produce high-quality tunnel junctions. At elevated temperatures, substrate interaction plays an important role. Studies of NbN on quartz at 200 to 400° C (Hunt *et al.*, 1989) have shown that a buffer layer of MgO or Al_2O_3 is necessary to prevent degradation of the first layers of NbN. Single-crystal sapphire substrates yield high-quality films and junctions when the substrate is heated to 400° C. Single-crystal MgO yields even better quality films than sapphire, although no junctions have been fabricated on MgO by our group. Work by Talvacchio and Braginski (1987) indicates that at elevated substrate temperatures NbN grows epitaxially on MgO and on most crystal orientations of sapphire. The exact temperature needed depends on the crystal plane of the substrate.

Substrate cleaning procedures also affect NbN quality. For unheated substrates, film and junction quality is somewhat insensitive to the substrate cleaning procedure. At elevated substrate temperatures, any residue left behind by the cleaning steps will inhibit the growth of superconducting NbN. In our

laboratory, substrates are typically cleaned ultrasonically in a series of rinses (Alconex soap, DI H_2O twice, acetone, and finally isopropyl alcohol). Cleaned samples are stored in isopropyl alcohol in sealed glass containers. Oxidized silicon wafers are frequently not cleaned, because they are cleaned by the manufacturer.

NbN Deposition Systems

NbN tunnel junctions are deposited in ultrahigh vacuum (UHV) system. A DC magnetron sputter-gun is used to deposit NbN and an RF magnetron sputter-gun or electron-beam evaporation source is used to deposit MgO. We have used two different systems. The first system is pumped by an ion-pump and a turbo-pump. MgO barriers are deposited by electron-beam evaporation. The second system is designed to fabricate NbN junctions; Figure 2.2 shows a schematic of it. The system is pumped by an 8" cryopump, and it is equipped with a turbo-pumped, load-lock chamber. Samples are introduced into the load-lock chamber, which is then pumped out for 5 to 10 minutes. A gate valve to the main chamber is then opened for sample introduction into the main chamber. The system base pressure is typically 2×10^{-8} Torr. The system has two US Inc. 2" diameter DC magnetron sputter-guns and one US Inc. 2" diameter RF magnetron sputter-gun. All of the sputter-guns are in a vertical orientation below the substrate. The sputter-guns, thermal gold evaporation source, and ion-mill are all on a 12" diameter circle. Substrates come up through the load-lock gate valve (also on the 12" circle) into a bayonet-mount substrate holder. Substrates are typically 2.5" above the sputter-guns, but the height can be varied. The substrate holder can rotate 360° continuously, and it has a molybdenum meander-line heater, which is close to the substrate. With this heater, substrates can be heated to 550° C. Electrical connection is made to the heater through a system of copper-beryllium brushes. The gas mixture in the system is regulated by four mass-flow controllers. Ultrahigh purity gases are used in the gas mixture. Both the Au and Nb fluxes can be measured using crystal rate monitors installed near the sources.

Sputtering Procedures and Parameters

The geometry of the sputter-guns used to deposit NbN and their placement in the vacuum system influence sputtering conditions significantly. This sensitivity to geometry makes transferring sputtering conditions from one system to another difficult. Several methods are available to optimize the controllable variables in the sputtering process (argon and nitrogen partial pressures, argon and nitrogen flow rates, sputtering voltage or current, and substrate-to-target distance). The methods used in our lab and elsewhere are now discussed.

In general, as the total sputtering pressure is reduced, transition temperatures increase, but as total pressure is reduced, compressive stress in the films increases, causing poor adhesion of the film to the substrate. Sputtered films generally have compressive stress when deposited at low pressures and tensile

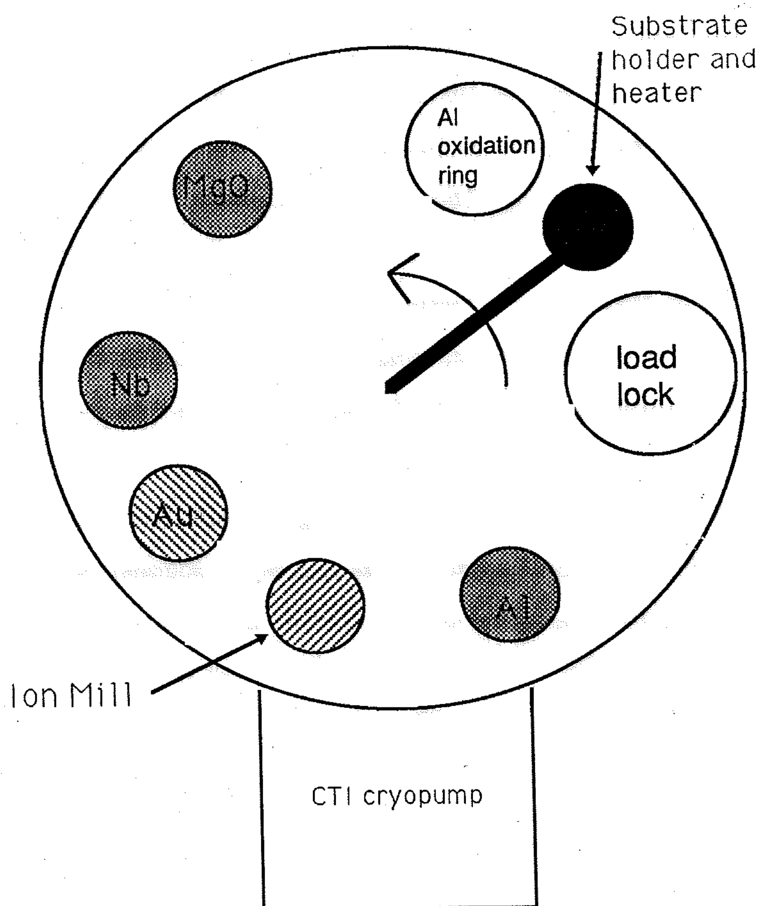

Figure 2.2 Schematic diagram of vacuum deposition system. A top view of the vacuum system used for trilayer deposition is shown above.

stress when deposited at high pressures (Hoffman and Thorton, 1977). The optimum total pressure is the lowest pressure for which adhesion is not a problem.

NbN quality is a strong function of nitrogen partial pressure, because this pressure controls the stoichiometry of the film. Two methods have been used to optimize nitrogen partial pressure. The partial pressure can be optimized by considering the nitrogen consumption versus injection curve (Thakoor *et al.*, 1985). In this method, the nitrogen partial pressure and total pressure are measured before a potential is applied to the sputter-gun. The drop in the total pressure after the potential is applied indicates how much nitrogen is being consumed by the reactive sputtering process. The consumed nitrogen can be measured as a function of the partial pressure of nitrogen. Empirically, the shape of this curve is an indication of the proper nitrogen partial pressure. Nitrogen partial pressure can also be optimized by monitoring nitrogen and niobium emission lines in the plasma (Bhushan, 1987a, 1987b). This measurement gives an indication of the relative abundances of niobium and nitrogen. Both of these methods are time-consuming, and they are best used to determine the optimum nitrogen pressure in a new vacuum system. The nitrogen partial pressure can be fixed at the optimal value, once it has been determined.

If reproducible films are to be obtained, NbN sputtering rates must be kept constant. The sputtering rate will change significantly as the Nb target erodes with use, particularly if small sputtering targets are used. This variable can be eliminated by measuring the Nb flux with a crystal rate monitor; the sputtering current can be adjusted to keep the rate constant. This method has proved effective in obtaining high-quality films throughout the life of a target.

Before each sputter deposition, the target is presputtered in a pure argon atmosphere. This removes the nitrided layer on the target and helps eliminate problems of target memory of previous depositions. A second presputter in the argon-nitrogen mixture will allow the target to come to equilibrium, so the sputtering conditions do not vary during the film deposition.

All of the methods discussed above are guidelines. Regardless of the methods used, some trial and error is necessary using the transition temperature as a measure of NbN quality. High-quality films can be deposited reproducibly, once deposition parameters have been optimized. A list of typical sputter conditions used in our lab is given in Table 2.1 as a starting point.

Table 2.1 Conditions for NbN Deposition

Parameter	Value
Argon Partial Pressure	12.0 mTorr
Nitrogen Partial Pressure	1.5 mTorr
Argon Flow Rate	150 sccm
Nitrogen Flow Rate	15 sccm
Sputtering Current	0.5-0.8 Amps
Sputtering Voltage	-230 Volts
Deposition Rate	7 Å/sec

B. Barrier and Junction Trilayer Deposition

The junction trilayer is formed by sequentially depositing the NbN base electrode, MgO barrier, NbN counter electrode and Au cap layer. NbN deposition has already been discussed in detail, so this section will focus on the formation of the barrier. The MgO barrier grows epitaxially on the base electrode. This barrier acts as a template for the growth of the counter electrode in the B1 phase. The growth mode of MgO on NbN leads to high-quality NbN tunnel junctions. After the barrier is deposited, an oxygen glow discharge is performed to form a thick oxide in any pinholes in the barrier. Following the counter electrode deposition, a thin, gold layer is deposited to prevent the counter electrode from oxidizing.

MgO Barrier Deposition

MgO grows epitaxially on NbN; this means there is a definite registration between the deposited MgO lattice and the underlying NbN lattice. This registration helps to stabilize the counter electrode. Both MgO

and NbN have the B1 crystal structure. The lattice spacing in NbN is 0.4392 nm, and the lattice spacing in MgO is 0.4211 nm. There is a 5% mismatch between the MgO lattice and the NbN lattice. The lattice match between MgO and NbN is good, but not exceptional. Low-energy electron diffraction (LEED) and reflection, high-energy electron diffraction (RHEED) studies of the NbN/MgO system by Talvacchio and Braginski (1987) have shown that MgO will grow epitaxially on polycrystalline and single-crystal NbN films. This MgO layer acts as a template for the growth of the counter electrode in the B1 phase. The epitaxial growth of MgO on NbN accounts for the high quality of NbN/MgO/NbN junctions as compared to NbN junctions with other barrier materials. In order to get high-speed junctions, the barrier must be very thin; therefore, the barrier must coat the base-electrode surface, even for very thin layers.

Epitaxial growth can be broken into three general categories. If the free energy of the base-layer (NbN) surface is less than the deposited material (MgO), the deposited material will grow in islands and only form a continuous layer for thick films (Volmer-Weber growth). If the free energy of the base-layer surface is greater than the deposited material, the first monolayer of deposited material will coat the entire surface to lower the free energy of the system. Subsequent layers may still form islands (Stranski-Krastanov or S-K growth), or grow monolayer by monolayer (Frank-Van der Merwe growth). If there is a good lattice match for the two materials, Frank-Van der Merwe growth will occur, otherwise S-K growth will occur. If the first monolayer of the barrier coats the NbN surface, a pinhole-free barrier will result. The reactive surface of NbN should have a higher free energy than the chemically inert surface of MgO.

The experimental evidence suggests that MgO grows on NbN in the S-K mode (LeDuc *et al.*, 1987). Thin layers of MgO provide pinhole-free tunnel barriers; this indicates the first monolayer is coating the base electrode. Because junction resistance increases slower than exponentially with increasing barrier thickness, the MgO is probably growing in islands after coating the surface, so most of the tunneling takes place through thin spots between the islands. RHEED and LEED data by Talvacchio and Braginski *et al.* (1987) reveals that although MgO grows epitaxially on NbN, the diffraction spots are smeared, indicating a rough surface. Figure 2.3 shows a cross sectional TEM of a junction. In this micrograph, crystallites of NbN continue through the barrier region, indicating that the barrier is growing epitaxially on the NbN, and the counter electrode is growing epitaxially on the MgO. The available evidence implies that MgO growth on NbN follows the S-K mode. When looking for potential new barriers, both the lattice match of the material with NbN and the surface chemistry of the barrier growth should be considered.

We have successfully deposited MgO barriers with electron-beam evaporation and RF magnetron sputtering. In both cases, the MgO is deposited as a compound. Electron-beam evaporation is done from a 3 kWatt TLI Inc. source. Sputtering is done from a 2" RF magnetron sputter-gun in 10 mTorr of Ar. The sputtering power is 50 Watts at a frequency of 13.56 MHz. RF sputtering is preferred over e-beam

Figure 2.3 Transmission electron micrographs of a NbN/MgO/NbN trilayer. In this film the diameter of the crystallites is roughly 30 nm.

evaporation, although both methods work well. Covering rough base electrodes is easier with sputtering, because it is not a directional process, whereas evaporation is. RF sputtering of the barrier is also more compatible with NbN deposition, because both are done in an argon atmosphere. If e-beam evaporation is used, the chamber must be evacuated before the MgO deposition. This extra pumping step allows the NbN base layer to be contaminated by oxygen and water vapor in the vacuum system. NbN tunnel junctions cannot be made by depositing Mg overlayers and then oxidizing the over layers, as is done with Al on Nb, because Mg diffuses into NbN (Braginski *et al.*, 1986).

MgO barriers are typically deposited while rotating the substrate holder past the MgO sputter-gun in a circular orbit (Shoji *et al.*, 1985); however, we have fabricated junctions both with intermittent

MgO deposition and with the substrate directly over the MgO sputter-gun during the barrier deposition. Intermittent deposition of MgO is preferred, because it gives more uniform coverage of the base layer, helps cover any roughness in the base electrode and gives lower, more controllable deposition rates.

Oxygen Pinhole Cure

An oxygen-glow discharge is performed after the barrier deposition to cure pinholes. If there are any holes in the barrier, the oxidation step will grow a NbO_x layer in these regions. If the NbO_x is thick enough, tunneling will occur preferentially through the MgO. Low, critical-current density junctions have been made without this oxidation step, but as the barrier is made thinner, the pinhole cure becomes necessary to avoid electrical short circuits in the barrier.

Residual gas-analyzer measurements, during both sputtering and evaporation of MgO, show an increase of the oxygen partial pressure; this indicates that the deposited MgO layer may be losing oxygen during deposition. The oxygen- glow discharge may be replacing lost oxygen in the MgO barrier layer.

The glow discharge is done with 115 mTorr of oxygen in the chamber. A potential of -500 Volts is applied to a high-purity aluminum ring beneath the substrate for 1 minute. As the barrier thickness is reduced, the oxidation time is reduced to get high critical-current density junctions. If oxidation time is held fixed and junctions with decreasing barrier thicknesses are fabricated, then the junctions with the thinnest barriers will have higher resistance than the junctions with thicker barriers. This indicates that for thin barriers oxygen is diffusing through the barrier and forming a tunneling oxide.

The Trilayer Junction Process

The tunnel-junction trilayer (NbN/MgO/NbN) is deposited sequentially in a single vacuum pump down; otherwise the superconductor barrier interface will not be a clean one. The trilayer method was first developed by Gurvitch *et al.* (1983) for Nb/Al-AlO_x/Nb tunnel junctions. In the trilayer method, the entire wafer is covered with the trilayer. All processing of circuits and junctions takes place after the trilayer deposition. The advantage of this process is that the junction interface region is contamination- and damage-free, because no cleaning step is required before depositing the barrier or counter electrode. Trilayer processing is especially important for materials with short, electronic coherence lengths, such as NbN. In short coherence-length materials (ξ = 4 nm), even a monolayer (0.4 nm) of damaged or contaminated superconductor near the barrier will degrade device properties.

Typically, the final step in our trilayer formation is the deposition of a thin, gold layer (30 nm). This gold layer prevents the counter electrode from oxidizing and allows the subsequent wiring layer to make good electrical contact to the counter electrode. Junctions can also be made without gold caps, but the counter electrode must be cleaned using an ion mill before the wiring electrode is deposited. Figure 2.5(a) shows a diagram of a completed trilayer before it is processed.

C. Standard junction processing

The junction trilayer must be processed to form small-area tunnel junctions, circuits, and antennas. Two of the key technologies in this process are reactive ion etching (RIE) and photolithography. Photolithograpy is used to define small features, and RIE is used to etch these features. Overviews on these two technologies are given to introduce these technologies, describe the exact processes used in our lab, and to understand the limits in fabricating submicron tunnel junctions. The two processes we use to fabricate one-micron tunnel junctions are described. Following this, a description of the difficulties and limitations of these processes is given.

Physics of Reactive Ion Etching

Reactive ion etching (RIE) is a dry anisotropic form of etching. Figure 2.4 shows a typical reactive ion etcher. The etcher consists of two parallel plates in a vacuum chamber. A gas species, such as CF_4, is introduced through the top plate. The pressure in the etcher is typically 10-100 millitorr. The samples rest on the bottom plate. This plate has an RF signal is applied to it, and the top electrode is grounded. This creates a plasma in the chamber. A DC voltage will arise on the RF electrode, because of the difference in mobility of the ions and electrons. During the positive half of each RF cycle, electrons will move towards the bottom electrode, but during the negative half of the RF cycle, the heavier ions will move much less towards the bottom electrode; this creates a net negative bias on the RF electrode. The bias voltage will accelerate positive ions towards the RF electrode and the sample. If the ions are reactive, such as a fluorine radical, they will react with the NbN to form NbF_5, which is volatile and will be pumped out of the system. The DC bias will give the ions a large, vertical velocity component, so the etch is anisotropic. Oxygen is added to the gas mixture to avoid the formation of fluorinated carbon compounds. The oxygen plasma acts to etch organic material away. Unfortunately, the oxygen also etches the photoresist.

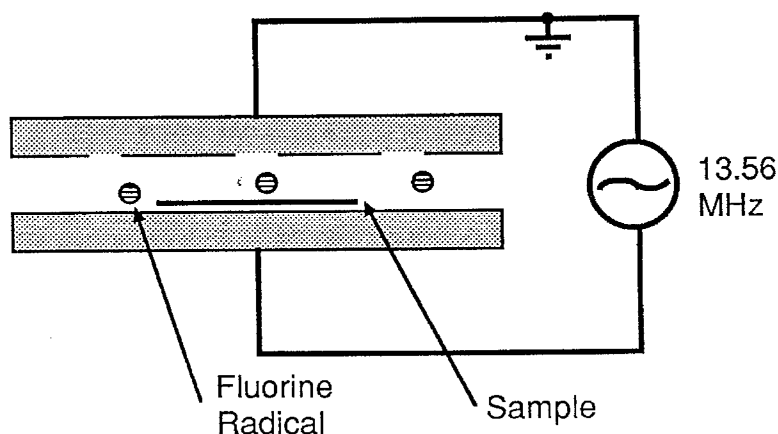

Figure 2.4 Reactive ion-etching system.

The Au and MgO layers cannot be reactively etched; for these materials, a straight sputter etch is

used. Pure Ar is introduced into the chamber, and the materials are etched by Ar ions dislodging Au atoms or MgO molecules, just as they would in RF magnetron sputtering. Sputter etch rates are slow compared to RIE rates, but both the Au and MgO layers are thin. Table 2.2 shows typical etching conditions and rates for NbN, Au, MgO, photoresist, SiO and SiO_2. A good review of the subject is given in a text edited by Powell (1984).

Table 2.2 RIE Etch Rates

Material	Cf_4-O_2 etch rate[1] (nm/min.)	Ar etch rate[2] (nm/min.)
Au	–	10
NbN	170	5
MgO	–	0.3
SiO	60	–
SiO_2	100	–
SOG[3]	100	–

[1] etch rates for: $F_{CF_4} = 20$ sccm, $F_{O_2} = 2$ sccm, Pressure=30 mTorr, Power=0.16 W/cm^2
[2] etch rates for: F_{Ar}=20 sccm, Pressure=30 mTorr, Power=0.16 W/cm^2
[3] SOG was Filmtronix GL 802 cured at 210° C for 20 min.

Reactive ion etching, not wet etching, is used, because it is anisotropic, so small features can be etched without undercutting. Additionally, RIE is less sensitive to temperature than wet etching, because the etch rate is controlled primarily by the pressure and power density. Dry etching is rapidly becoming the standard form of etching in the semiconductor industry.

If reproducible RIE processing is to be obtained, an endpoint detection method is needed. The simplest method of endpoint detection is watching through the etcher window for a wafer to etch completely through. When etching through the counter electrode, the trilayer does not etch completely through. To detect the counter electrode endpoint, a test sample with only a NbN layer the thickness of the counter electrode can be used; when this clears, the etch is done. This method is simple and reliable, although a second NbN deposition is necessary to make the test sample. Another endpoint detection method uses an optical multichannel analyzer (OMA) to monitor emission lines in the plasma. Nitrogen emission lines at wavelengths of 335 nm and 355 nm can be used to monitor NbN etch rates; when the emission signal drops, the etch is complete. If the area being etched is less than 0.25 sq. inches, the emission signal is too small, and this method will not work. Both of these methods have been used successfully in our lab.

Photolithography

Photolithography is used to define small features in solid-state devices. Typically, a photoactive polymer (photoresist) is applied to the surface of the sample; a small amount of photoresist is applied to

the center of the sample, and the sample is spun a several thousand revolutions per minute to evenly coat the sample. The photoresist is exposed to optical or ultraviolet radiation in certain regions. The radiation changes the solubility of the photoresist in a developer. The sample is then immersed in the developer to remove the exposed photoresist (positive imaging photoresist), or leave the exposed photoresist (negative imaging photoresist). The most common photoresists are diazo-based resist (*e.g.*, AZ 1350-J). These resists are positive imaging and develop in a basic solution. The photoresist pattern can be used to mask a substrate during an etch, or a material can be deposited on the photoresist pattern and lifted off by dissolving the remaining photoresist.

Lithography of small features is typically done at ultraviolet (UV) wavelengths to reduce diffraction. For high-frequency mixers, submicron devices are desirable. In fabricating small-area junctions, lithography limits the minimum feature size, so UV lithography should be used. Most research is done with contact mask aligners; the sample is brought as close to a mask as possible. The mask is a glass or quartz plate with a metal or emulsion pattern on it. After aligning the sample to the mask, the photoresist is exposed by UV radiation.

The limit to photolithography resolution is determined by near-field diffraction around the photomask features. Typically the mask-to-sample separation is a few microns. This separation is determined by the thickness of the photoresist, particle contamination on the mask or sample and the flexibility of the substrate (more flexible substrates will conform better to irregularities). The near-field diffraction pattern around the mask cannot be calculated analytically; however, several generalizations can be made on the basis of numerical solutions. Minimum-feature sizes will scale down with higher frequencies; therefore, most lithography is done in the UV range. Unfortunately, even the most sensitive diazo-type photoresists are not sensitive at wavelengths shorter than 310 nm; for this reason, much high-resolution UV lithography is done at 315 nm. At higher frequencies, photoresists such as polymethyl methacrylate (PMMA) and polymethyl isopropenyl ketone (PMIKB), which are more difficult to process, are used. At 315 nm, resolution of 0.6 μm can be achieved under optimal conditions; however, at this resolution, photoresist profiles will be significantly rounded. A good review of this and optical lithography in general is given by Lin (1980).

Our mask aligner is a Carl Suss MJB-3 contact printer. This mask aligner has a high-pressure mercury vapor lamp with filters cutting off radiation for wavelengths above 315 nm. Two photoresist families are used in our processing, the AZ 4000 series and the AZ 5200 series. The AZ 4000 series photoresists (4330 RS, 4210, and 4110) have excellent resistance to dry etching, although they do not reproduce small features well. The AZ 5200 series photoresists (5214-E and 5206-E) reproduce micron and submicron features well. AZ 5206 is only 0.6 μm thick when applied at 4000 rpm as compared to 1.4 μm for AZ 5214. The thicker photoresist proved more useful for all but the smallest features (dots less than 2 μm

in diameter and lines less than 1 μm in width). Using a post-exposure-bake and a flood exposure, AZ 5200 photoresists can be reversed from a positive to negative imaging photoresist. Image reversal with AZ 5200 photoresists is particularly useful, because an etch and lift-off process can be tried with the same mask plate. When reversed, AZ 5214 makes an excellent lift-off-stencil, because an overhanging profile is naturally obtained. Two developers are used with these photoresists (AZ 400K and AZ developer). AZ developer is NaOH-based and is used when aluminum processing is done; AZ 400K is KOH-based and etches aluminum rapidly. Detailed processing descriptions for these photoresists are included in Appendix B.

Mesa and Cross-Line Junction Processing

Most junctions fabricated at JPL use the mesa-junction process; this process is shown in Figure 2.5. A photoresist pattern is defined, and the trilayer is etched completely through. The photoresist is removed, and a second photoresist layer is defined in the shape of a dot, which will delineate the junction area. The exposed trilayer is etched down to the barrier to form a mesa. This mesa is electrically isolated by the deposition of an insulator, such as SiO or SiO_2. The photoresist dot is lifted off to reveal the planarized junction mesa. This isolation technique is called self-aligned liftoff, because the same photoresist layer is used for the mesa etch and dielectric liftoff. Finally, a NbN wiring electrode is deposited over the entire wafer, a photoresist pattern is defined, and the wiring layer is etched through. This process is fairly simple for junctions that are 2×2 μm^2 or larger, and with effort 1×1 μm^2 junctions can be fabricated.

A similar, but more complicated, cross-line process involves defining a junction at the intersection of two lines. The cross-line process is shown in Figure 2.6. The first steps are identical to the mesa process; however, instead of a dot, a line is etched, planarized and lifted off. The wiring electrode is deposited, and a second photoresist line crossing the first line is defined. Both the wiring layer and the counter electrode are etched through. The junction area is delineated only where the two lines overlap. The advantage of the cross-line process is that smaller and more uniform area junctions can be fabricated with optical lithography. The disadvantage of this process comes during the final RIE step; the wiring layer, gold cap and the counter electrode must be etched. The extra etch steps of the gold cap and counter electrode may etch through a thin photoresist stencil. Additionally, the junction area is much more exposed, because the wiring layer no longer completely encases the junction. Some cross-line junctions have degraded with time, because oxygen diffuses through the gold layer and creates a series weak link between the wiring electrode and the counter electrode. This problem could be reduced by coating the junction area with a protective layer, such as SiO.

In the actual mesa and cross-line process, there are several difficulties that arise. When attempting to fabricate small junctions ($\leq 1 \mu m^2$), diffraction in the lithography step is a problem. The cross-line process lessens this problem, because the diffraction occurs in only one dimension. In general, cross-line

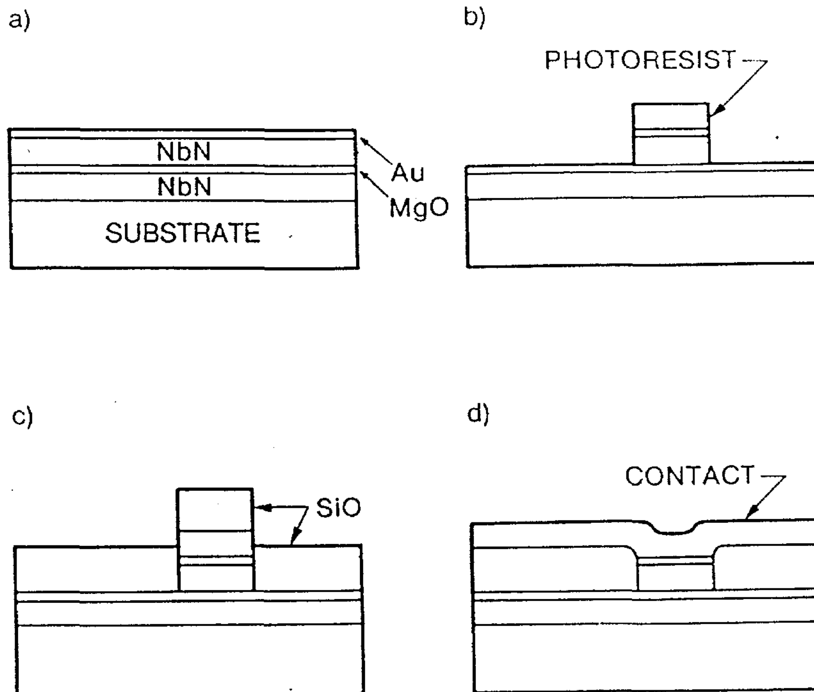

Figure 2.5 Mesa junction processing steps. (a) The unprocessed trilayer is shown; the base layer thickness is typically 250 nm, the counter electrode thickness is typically 120 nm, and the gold cap is 30 nm. (b) The junction area is defined by a photoresist dot, and the counter electrode is subsequently etched. (c) An insulating SiO layer is deposited and later lifted off. (d) A wiring layer is deposited and patterned.

junctions are of more uniform size and shape than mesa junctions. (Cross-line junctions are square, while mesa junctions have rounded corners.) As the junction size gets smaller, thinner photoresists are used to reduce diffraction. If the photoresist thickness is roughly equal to the dielectric thickness, lifting off the dielectric can be difficult. In particular, the dielectric layer will continuously cover the photoresist, without a break at the edge, if the photoresist profile is rounded. When the photoresist is lifted off, a vertical wall of dielectric will be left where the edge of the resist was. This "liftoff flag" is difficult to cover with the wiring layer. Additionally, the photoresist layers may polymerize during the RIE steps, leaving photoresist residue, which is difficult to remove. Finally, RIE forms vertical edge profiles. Covering the vertical edge of the the NbN film with a continuous dielectric layer is difficult. All of these problems can be tolerated if the processing is carefully controlled.

Several insulators are used to planarize mesa and cross-line junctions. SiO (actually SiO_x) is thermally evaporated in a diffusion-pumped system for many junctions. The main disadvantage of SiO is that the dielectric properties are not well defined and can vary with oxygen content. This can be a problem when microstrip line circuits are being fabricated and line impedances and electrical lengths need to be known accurately. SiO_2 has more well-defined dielectric properties than SiO and can be deposited by e-beam

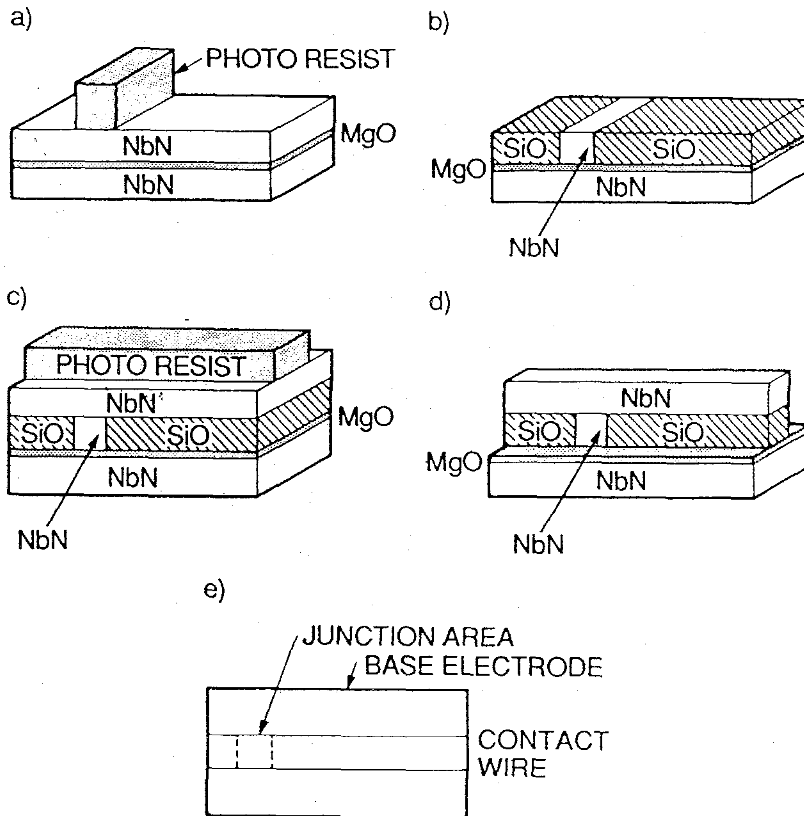

Figure 2.6 Cross-line junction processing steps. (a) A photoresist line is defined. (b) The counter electrode is etched and the line planarized. (c) A wiring layer is deposited and a photoresist layer is defined to form a cross line. (d) The wiring and counter electrode are etched through to delineate the junction area. (e) A top view of the completed junction is shown.

evaporation. During e-beam evaporation, oxygen can be lost from the films, so the evaporation is done in 2 mTorr of oxygen. In the cross-line process, the planarization layer is subject to the final RIE step. To avoid etching of the SiO or SiO_2 by the CF_4-O_2 plasma, a thin MgF or MgO layer is deposited on top of the SiO or SiO_2 to act as an etch stop. MgF is thermally evaporated, and MgO is e-beam-evaporated in oxygen.

The standard mesa and cross-line junction processes can be used to fabricate junctions with areas down to 1 μm^2. At submillimeter wavelengths, smaller junctions are needed to reduce the junction capacitance.

D. Submicron Device Processing

NbN/MgO/NbN tunnel junctions used as mixers at submillimeter wavelengths must have submicron areas to have small RC products. Using UV lithography, the cross-line process should work for dimensions as small as 0.6 μm. This is the minimum feature size attainable with our photolithography equipment. The self-aligned liftoff technique does not work well for submicron junctions. An alternate planarization method involving planarization and etch-back is described. This method is applicable to both mesa and

cross-line junction fabrication. In addition, this method can be used to planarize junctions defined by electron-beam lithography. The combination of electron-beam lithography and etch-back planarization is a good method for fabricating submicron tunnel junctions. An alternate approach has been developed to fabricate submicron NbN/MgO/NbN edge-geometry junctions. These methods are now described and compared.

Submicron Cross-Line Junctions

Submicron tunnel junctions have been fabricated using the cross-line process and mid-UV lithography (Aoyagi *et al.*, 1986). We had limited success in fabricating submicron cross-line junctions in our lab. To reduce diffraction, a thin photoresist, AZ 5206, is used. The edge profile of submicron lines in this photoresist are rounded. This rounding leads to insulator liftoff flags. If the wiring electrode is not continuous over the flag, the device will be an open circuit. Additionally, the photoresist may not liftoff at all if the coverage of the photoresist layer by the dielectric layer is continuous. The thin photoresist layer of the second line must withstand the etch of the wiring electrode and the counter electrode. Work on submicron cross-line junctions is continuing in hope of fabricating $0.5\mu m^2$ junctions.

Planarization and Etch-Back Tunnel Junction Processing

Planarization and etch back is an alternative technique to self-aligned liftoff for electrically isolating submicron cross-line and mesa junctions. As was previously discussed, self-aligned liftoff is problematic for very small junctions. The etch-back technique involves covering the entire trilayer with a planar dielectric layer. High spatial frequency features, like the junction mesa or trilayer edge, are planarized. Using reactive ion etching, the dielectric is etched back until the mesa surface is exposed. The junction wiring layer is deposited and etched in the normal manner. In the planarization and etch-back technique, the mask layer used to etch the junction mesa is not used for liftoff of the dielectric layer. The mesa etch mask layer can be a 50 nm thick aluminum dot. This metal etch mask can be defined using optical or e-beam lithography.

Two planarization techniques have been used by other groups to fabricate tunnel junctions. Bias sputtering of SiO_2 has been used to planarize SIS tunnel junction (Imamura *et al.*, 1987). In this process, an RF bias is applied to the substrate and SiO_2 is sputter-deposited. Back sputtering occurs preferentially from sharp features on the substrate, because high electric fields form at sharp features. Spin-on glass (SOG) has also been used to planarize junctions. A SOG is an organic solution that can, like photoresist, be spun on and cured to form a glass-like layer. In the SOG etch-back method, an insulating layer (SiO_2) is deposited, the SOG is applied to planarize the sample, the SOG is cured to form a glass-like layer, and the glass layer and some of the insulator are removed in an etch-back step. By controlling the cure temperature, the SOG etch rate can be matched to the insulator etch rate.

Mesa junctions have been fabricated at JPL using a slightly modified SOG etch-back process; this process is shown in Figure 2.7. A junction trilayer is deposited normally. After the trilayer is etched, it is planarized by self aligned lift-off (Figure 2.7(a)). An aluminum mask layer is deposited and wet-etched to form a 1 μm diameter dot. The counter electrode is etched to form the mesa (Figure 2.7(b)). The aluminum layer is removed, a photoresist dot 4 μm in diameter is aligned on top of the mesa, and a dielectric layer is deposited (Figure 2.7(c)). The photoresist is lifted off to reveal the mesa; a spin on glass is applied and cured at 210° C (Figure 2.7(d)). The spin-on-glass layer is etched back to reveal the mesa surface; the wiring layer is deposited and etched normally (Figure 2.7(e)). The only SOG remaining after the etch-back is in the trench surrounding the junction. The dielectric properties of the SOG cured at low temperatures are not exceptional, but the SOG will electrically isolate the junction. This process is completely compatible with junctions defined by electron-beam lithography.

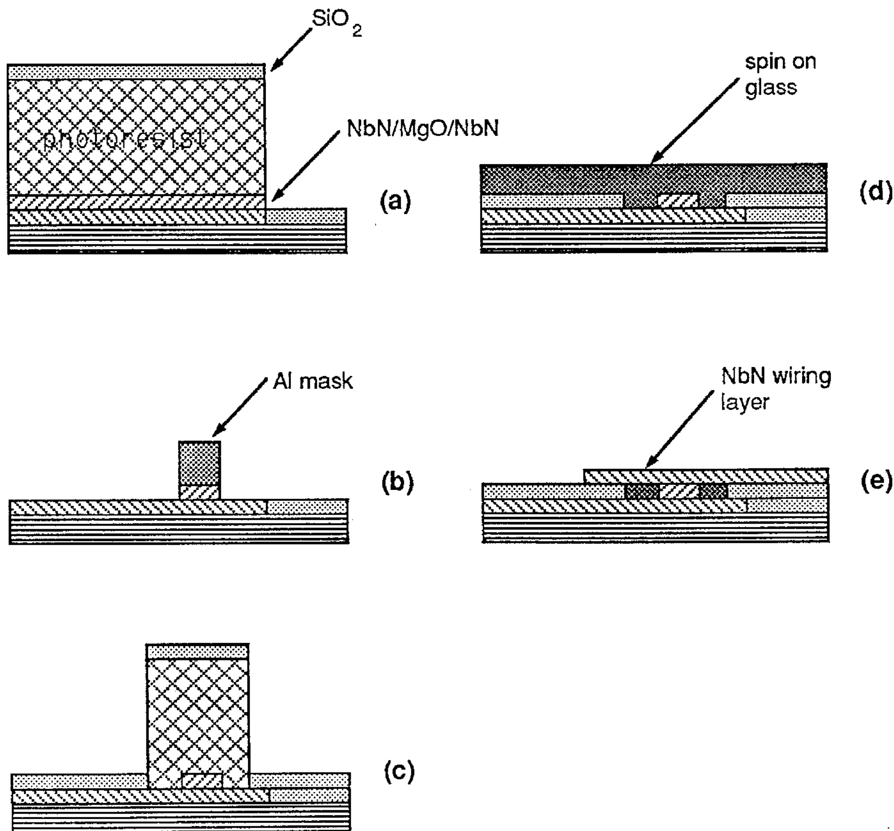

Figure 2.7 Spin on glass, etch-back junction processing steps. (a) The trilayer is etched and planarized. (b) An aluminum mask layer is defined and the junction mesa is etched. (c) A dielectric layer is lifted off around the junction area. (d) The SOG layer is applied to planarized the junction. (e) The completed device is shown.

NbN/MgO/NbN Edge-Geometry Junctions

A process for fabricating all NbN edge junctions has been developed at JPL by Hunt *et al.* (1989). In this process, a base NbN layer is deposited at elevated temperatures to promote the deposition of B1 material for the entire thickness of the film. An insulating layer is deposited on top of the NbN for use as an etch mask. The NbN film is ion-milled through (I_{Ar^+}=25 mA, V_{Ar^+}=250 V) to form a slightly tapered edge, which is masked by an insulating layer. The exposed edge is cleaned by a second lower-energy ion mill step (I_{Ar^+}=10 mA, V_{Ar^+}=150 V) to remove any damaged NbN at the edge's surface. An MgO barrier is deposited, followed by a pinhole cure and the counter-electrode deposition. A lithography step defines an etch stencil of a line crossing the edge, and the counter electrode is etched. The junction area is defined by the base-layer thickness and the width of the line covering the edge. Using this technique, $0.1\mu m^2$ junctions have been fabricated. The difficulty with this method is that the entire base-layer thickness must be high-quality NbN, or a rounded gap will result. Some damage may remain from the low-energy ion cleaning. This damage will also lead to a rounded gap. Typical edge junctions have more rounded I-V characteristics than comparable trilayer junctions, because of these two factors. Additionally, edge-junction processing is less reproducible than mesa-junction processing. Despite these difficulties, edge junctions are attractive for high-frequency applications, because submicron junctions can be easily fabricated.

E. Chapter Summary

Many methods have been used to deposit NbN. Of these methods, only reactive magnetron sputtering yields high-quality films at low substrate temperatures. The optimum sputtering conditions will vary between vacuum systems. Determining these conditions can be difficult. I have attempted to outline the best methods for optimizing and controlling the deposition variables. This includes a complete description of our deposition conditions, and a description of several methods of optimizing nitrogen partial pressure. Once proper deposition conditions are determined, high-quality films can be deposited reproducibly. Good-quality junctions can be fabricated using MgO barriers and the trilayer process; this is for two primary reasons. MgO grows epitaxially on NbN and acts to stabilize the B1 phase. The trilayer method allows the formation of a contaminant-free, barrier-superconductor interface. The difficulty with the trilayer method is in fabricating very small-area junctions; however, submicron junctions can be fabricated using electron-beam lithography or edge-geometry junctions.

Chapter III. Materials and Device Characterization

This chapter presents measurements of NbN films, tunnel junctions and mixers. All of these measurements are made in order to understand and improve mixer results. Resistance versus temperature and associated measurements are made on NbN films primarily as a quick method of measuring film quality. These measurements also yield insight into the microscopic structure of NbN films. This information can be used to improve film and junction quality. The I-V characteristics provide the most direct measurement of a tunnel junction's quality. I-V quality can be improved through understanding the physical origin of I-V properties and by observing how properties vary with deposition conditions. In particular, the voltage range over which the current is nonlinear is critical to mixer performance. The junction specific-capacitance and the NbN magnetic-penetration depth are two parameters that need to be known to properly design mixer circuits. These values are measured using two junctions in a superconducting loop, known as a superconducting quantum-interference device (SQUID). The last of these measurements to be made is the testing of the receiver performance of NbN junctions at 205 GHz. For these tests, integral tuning circuits were designed based on the junction specific-capacitance and NbN magnetic-penetration depth. The results are presented as a function of the tuning circuits' properties. Finally, the implications of these tests on future NbN mixers at higher frequencies are discussed.

A. Resistance as a Function of Temperature

One of the most important diagnostics of NbN film quality is a resistance-versus-temperature (R vs. T) plot, because the film's quality can be determined without fabricating a tunnel junction, a fairly elaborate process which can take several days. By contrast, an R vs. T measurement can be completed in the course of an hour, allowing an excellent feedback mechanism for depositing NbN in a new sputtering chamber. Once high T_c films can be deposited, the more complex task of junction deposition and fabrication can be undertaken with the knowledge that the NbN is of good quality. In addition, several other related measurements (residual resistivity ratio–RRR, room-temperature resistivity, and critical current-density) give indirect evidence of the microscopic nature of the NbN film. This evidence can be used to improve tunnel-junction quality.

R vs. T Measurement Apparatus

The apparatus used for the R vs. T and associated measurements is discussed before giving the results. The apparatus is designed to be simple and to allow rapid testing of samples. The samples are heat-sunk to a copper block to insure that the sample is at a uniform temperature. The copper block has enough thermal mass that its temperature is stable over the measurement period and is surrounded by a 1" diameter stainless steel can, which can be evacuated and then back-filled with helium gas. The helium acts as a thermal link between the copper block and the stainless steel can. The entire apparatus is lowered slowly

into a liquid-helium storage-dewar. The temperature of the sample is controlled by adjusting the height of the can above the surface of the liquid helium in the storage dewar. Measurements of R vs. T are made while both cooling and warming the sample to insure that any hysteresis in the plot can be accounted for. The temperature of the copper block is measured using a temperature-sensing silicon diode from Lakeshore Cryotronics Inc., which is accurate to ±0.1 K. The readings are also checked against a germanium resistance thermometer and found to agree to within 0.1 K. Electrical measurements on the sample are made using four wires to eliminate lead resistance. The measurement setup is simple, and sample turnaround is rapid. The use of a dipstick and a storage dewar minimizes liquid helium consumption.

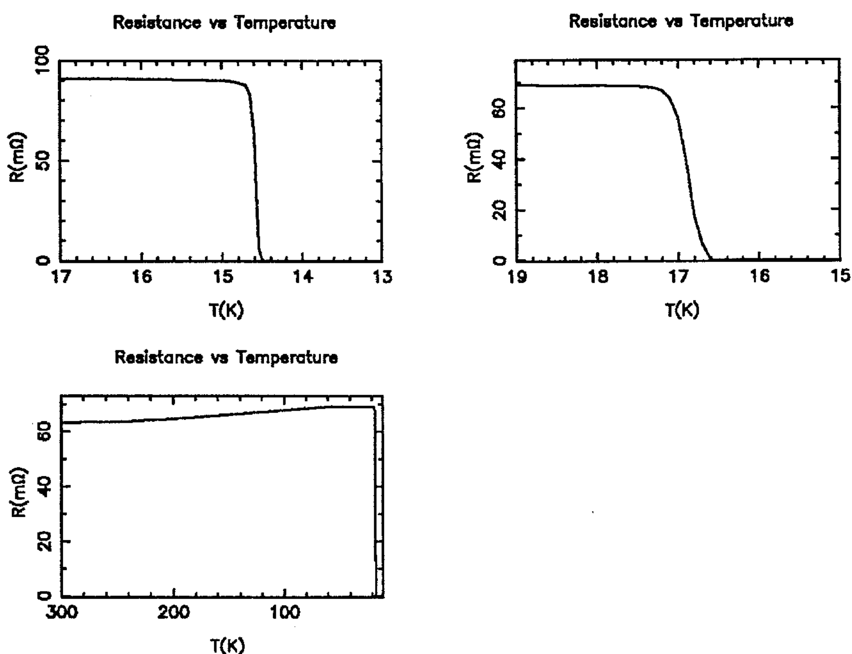

Figure 3.1 Resistance versus temperature plots. Figure (a) shows the resistance as a function of temperature of an NbN film deposited on an unheated oxidized silicon wafer. Figure (b) shows the resistance as a function of temperature for NbN deposited on a heated silicon wafer with an MgO buffer layer. Figure (c) shows this same transition over the entire temperature range of 300 to 10 K.

Superconducting Transition Temperature of NbN Films

The first thing one learns from an R vs. T measurement is the temperature of the onset and completion of the superconducting transition. A typical R vs. T plot for NbN deposited on an unheated, oxidized silicon substrate is shown in Figure 3.1(a) (T_c = 14.6 K). Here the onset of superconductivity begins near 14.7 K, and the sample has zero resistance by 14.5 K. In this thesis, T_c is measured as the midpoint of the transition; this is a reasonable definition if the transition is fairly sharp, as is typical for NbN. A sharp transition (0.3 K) indicates that the film is spatially uniform and composed of a single phase. High T_c NbN films can be

deposited at elevated temperatures; Figure 3.1(b) shows R vs. T curves for NbN on heated Si with an MgO buffer layer (T_c = 16.9 K, T_s = 350° C). The higher T_c film has a broader transition, indicating the existence of lower T_c material mixed with the B1 material; however, even in this case the transition is less than one Kelvin wide. Figure 1.3(c) shows R vs. T for this same film from room temperature down to 10 K. These two superconducting transitions are typical for films deposited on heated and unheated substrates.

Critical Current Density of NbN Films

NbN critical current density (J_c) can be measured by etching a well-defined line in the NbN film before measuring R vs. T. A film's critical current density is defined as the maximum supercurrent-per-unit cross-sectional-area, which can flow in a wire. NbN critical current density (J_c) should not be confused with tunnel-junction, critical current density ($\mathrm{J_c}$). In an ideal superconducting wire, as the current level is increased, the magnetic field created by the current increases; at some current value the energy associated with the screening currents, which are expelling the magnetic field from the wire, is equal to the condensation energy of the superconducting state; above this current level, the wire will go into the normal state. By comparison, the critical current density of polycrystalline films will be dominated by the conduction mechanism between grains, and the size of the grains. Thin nonmetallic layers between grains will lower the current density more than will metallic or low T_c superconducting layers between grains.

Critical current densities of our NbN films varied significantly as a function of film quality. As an example, J_c was measured for a typical film deposited on unheated, oxidized Si; the film had a transition temperature of 14.3 K and a critical current density of 3×10^6 Amp/cm^2, whereas a film deposited on heated Si with an MgO buffer layer had a transition temperature of 16.6 K and a critical current density of 6×10^6 Amp./cm^2. Critical current densities in our films are reduced from the maximum value for NbN of 2×10^7 Amp/cm^2. The larger critical current density of films deposited on heated substrates is attributed to the larger grain size in these films. The reduction of critical current densities from its maximum value implies that even for heated films, the critical current density is limited by intergrain conduction.

Resistivities of NbN Films

Films, which are etched into wires, also allow for measurement of the NbN room-temperature resistivity (ρ = RA/l, ρ is the resistivity, A is the cross-sectional area of the wire, and l is the length). The resistivity of a film is an indication of the scattering length in the film. Films with a large number of defects, like grain boundaries and impurities, will have larger resistivities. High-quality films have resistivities of 100 $\mu\Omega$ cm, although the lowest reported values are those of Gurvitch *et al.* (1985) (ρ = 85 $\mu\Omega$cm). Our films range from 200 $\mu\Omega$ cm for typical films deposited on unheated substrates to 120 $\mu\Omega$ cm for typical films deposited on heated substrates (200-400° C). This is another indication that NbN quality improves

and crystallite size increases with increasing substrate temperature.

Residual Resistivity Ratios of NbN Films

The residual resistivity ratio also gives a measure of the conduction mechanism in NbN films. The RRR is defined as R(20 K)/R(300 K) (some authors define the RRR as the inverse of this). For high-quality NbN films, the RRR will be slightly below unity, indicating a metallic conduction mechanism between grains in the NbN film. The residual resistance ratio in high-quality NbN is near unity because NbN is a "dirty metal," meaning the resistance is dominated by impurity scattering of electrons, not phonon scattering. In lower-quality films, the ratio is above unity, indicating that a hopping or tunneling mechanism is dominating the conduction between grains at low temperatures. For reference purposes, the nitrided films of Gurvitch (1985) have RRRs of 0.80. Films deposited on unheated substrates have resistivity ratios of 1.1-1.2, indicating that the conduction between crystallites is not metallic; it also explains the lower critical current density in the films deposited on unheated substrates. Films deposited at elevated substrate temperatures (200-400° C) typically have RRRs of 1.05, although occasional films had RRRs less than one. As an example, the film in Figure 3.1(c) has a RRR of 1.05. Resistivities and residual resistivities for NbN are discussed at greater length by Wolf *et al.* (1980).

Conclusions

An important hypothesis can be formulated from the RRR, room-temperature resistance and current-density measurements. The nonmetallic values of the RRR, even for most films deposited at elevated substrate temperatures, indicate nonconducting material between grains of NbN. As substrate temperature increases, the RRR decreases, the room temperature resistance decreases, and the critical current density increases. All of these changes indicate that the size of the grains is increasing with increasing substrate temperature, thus reducing the effect of the intergrain material. The critical current density for samples deposited on heated substrates is typically twice that of samples deposited on unheated substrates, but is still a factor of three below the highest reported value, indicating that even for high-quality films there is nonsuperconducting material at the grain boundaries. Several interesting conclusions can be made. Grain size increases with increasing substrate temperature. Material at the grain boundaries limits conduction at low temperatures. The intergrain material is usually not metallic, but can be metallic if elevated substrate temperatures are used. Finally, the intergrain conduction can be improved significantly by adjusting the substrate temperature and deposition conditions.

These conclusions suggest that gap-smearing can be reduced by depositing junction trilayers onto heated substrates. Nonsuperconducting material, like grain boundaries, is a source of gap-smearing in NbN. Films with RRRs less than unity may show less gap-smearing than films with larger RRRs for two reasons. The grain size will be larger, thus reducing the relative contribution of the grain boundaries. The

material at the grain boundaries will be metallic or superconducting; this material at the grain boundaries will have a larger gap by the proximity effect than will insulating or semiconducting material. Thus, the gap-smearing will be less for junctions made with films having RRRs less than unity. This argument does not address the problem of surface roughness in heated films, but it does suggest that further work in fabricating trilayers on heated substrates may lead to junctions with narrower sum-gap voltages.

In summary, R vs. T measurements serve two important functions. They are the most convenient measure of NbN quality. Thus, R vs. T can be used to optimize sputtering conditions for a given vacuum system. This is particularly useful, because of the large number of deposition variables that need to be optimized. The RRR, room temperature resistivity and critical current density for a NbN film offer indirect evidence of the microscopic structure of the NbN film. This information may be useful in improving device properties.

B. Current-Voltage Characteristics

The response of an SIS mixer is determined by the tunnel junction's current-voltage characteristic and the embedding impedance of the junction at various frequencies (signal, IF and higher harmonics); therefore, a careful analysis of NbN/MgO/NbN I-V characteristics is very important. Chapter one described a number of properties of the I-V characteristic that affect mixer performance (gap voltage, gap voltage width and subgap resistance). This section describes typical and exceptional values of these properties. Wherever possible, the physical origin of these properties is described, because understanding of these origins may lead to improvements in the I-V characteristics. The temperature dependence of I-V characteristics is measured, so the possibility of operating NbN mixers at elevated temperature can be analyzed.

Measurement Apparatus and Sample Geometry

The techniques used to measure I-V characteristics are similar to those used to measure R vs. T. Most I-V measurements are made by immersing the sample directly in a liquid-helium storage dewar. Using this method, the sample can be cooled to 4.2 K and tested rapidly. Measurements of I-V characteristics as a function of temperature are made by attaching the sample to a copper block with thermal grease. The temperature of the copper block is measured with a temperature-sensing silicon diode. The temperature of the block was controlled by adjusting the height of the block above the liquid helium. This method gave temperature stability over the measurement period of ± 0.2 K.

Three types of samples have been used to measure I-V characteristics. The earliest measurements were made by indium-soldering leads to chips containing three 30 μm^2 devices. These samples were much less sophisticated than later samples, requiring only one photolithography step. The standard test chips used for materials development are 5/8" square. Each chip has three 4 by 4 μm^2, three 2 by 2 μm^2 and three 1 by 1 μm^2 devices on it. The nine devices share one common electrode, and all measurements are

made using the four-wire technique to eliminate the effect of series resistance in the leads. Contact is made to the chips by spring-loaded pogo pins. The most recent measurements on SQUIDs and series arrays are made with 1/4" square chips that are mounted in standard 28 pin dual-in-line, ceramic chip packages made by Kyocera Inc. Two-inch or three-inch diameter Si wafers are processed to completion and then cut into 88 separate 1/4" chips. One-mil aluminum wires are bonded from the package to the chip using an ultrasonic wedge-bonder. The adhesion of the aluminum to NbN is excellent. The use of the wire bonder and smaller chips has two advantages. With one mil aluminum wire, many connections can be made to a small chip. With the smaller chip size, 88 separate chips are processed in parallel. Because of these two facts, device-testing time, not device-processing time limits the rate of device measurement.

Gap Voltage

The gap voltage of an SIS tunnel junction can limit its high-frequency response. Gap voltages for NbN/MgO/NbN junctions are generally reduced from their maximum value. If the cause of this reduction can be determined, it may lead to improved gap voltages. The energy gap of the base electrode can be calculated using NbN/native-oxide/Pb junctions. When an SIS tunnel junction has two different superconductors as its electrodes, there will be a peak in the subgap conductance at a voltage corresponding to the difference in the energy gaps of the two superconductors ($V_{dif.} = (\Delta_1 - \Delta_2)/e$, where $V_{dif.}$ is the gap-difference voltage). The peak occurs at this voltage because thermally excited quasiparticles in the smaller energy-gap superconductor can tunnel into the infinite density of states in the larger energy-gap superconductor; this is shown in figure 3.2(a). The individual energy gaps can be calculated using the gap difference voltage and the gap sum voltage (V_{sum}). Figure 3.2(b) shows the I-V characteristic of a NbN/native-oxide/Pb junction; the NbN energy gap is found to be 2.8 meV ($V_{sum} = (\Delta_1 + \Delta_2)/e$=4.1 mV, $V_{dif.} = (\Delta_1 - \Delta_2)/e$=1.5 mV; therefore, $\Delta_1 = e(V_{sum} + V_{dif.})/2$=2.8 meV). The highest energy gap reported for NbN is 3.09 meV (Gurvitch, 1985). Gap-sum voltages for all NbN junctions should be as large as 6.18 mV; however, our junctions typically have gap-sum voltages between 4.5 and 5.2 mV, and most published values for NbN/MgO/NbN junction gap-sum voltages are below 5.3 mV. With substrate heating, larger gap-sum voltages are occasionally obtained. Figure 3.3 shows a junction with a gap-sum voltage of 5.6 mV, which is one of the largest values ever reported for NbN tunnel junctions. Figure 3.4 shows a junction with a gap-sum voltage of 5.0 mV, which is a large value for a trilayer deposited on an unheated substrate.

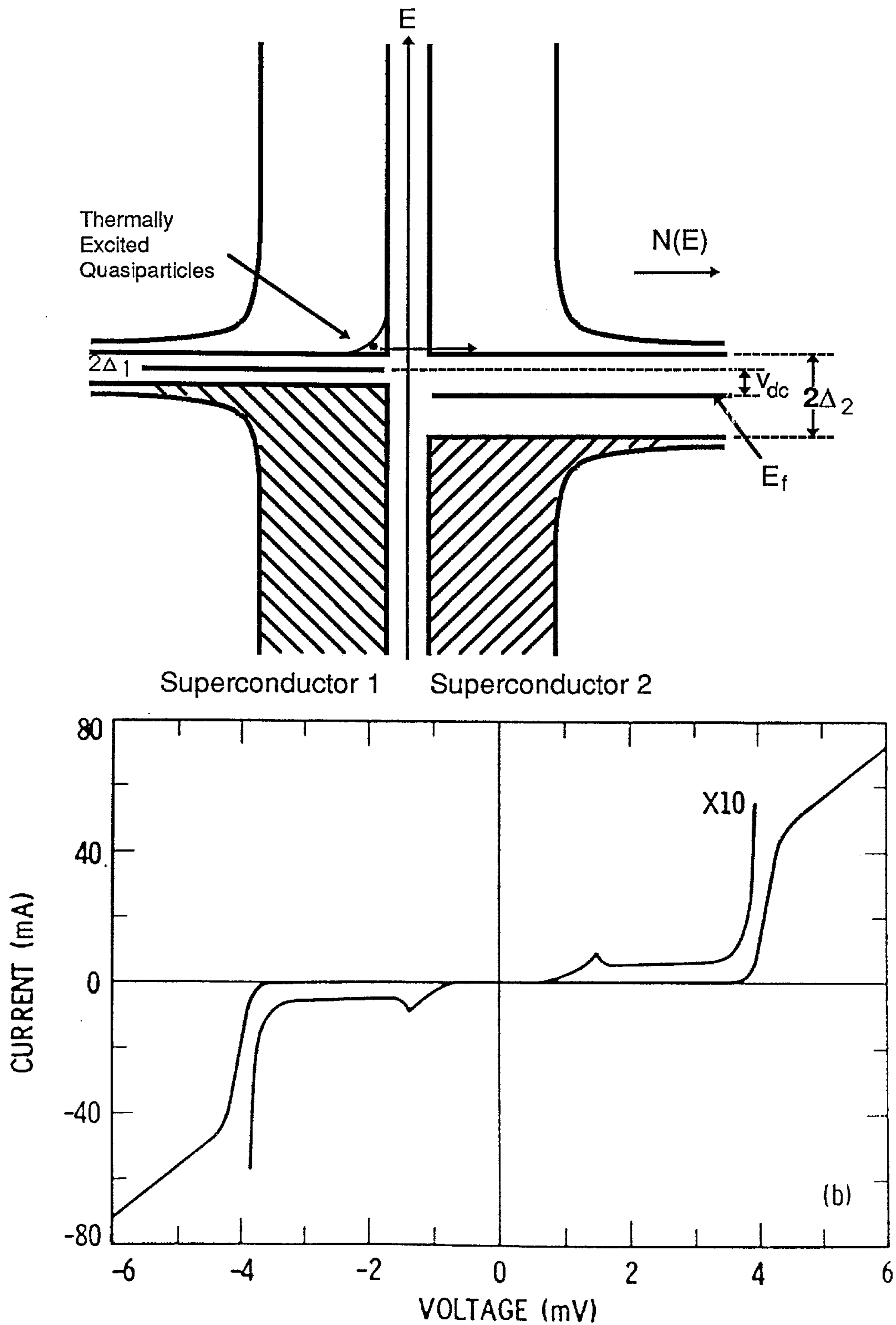

Figure 3.2 SIS I-V characteristic for nonidentical superconductors. Shown in Figure (a) is the semiconductor picture of a junction with two different energy-gap superconductors biased at the gap difference voltage. Shown in Figure (b) is the I-V characteristic for a NbN/native-oxide/Pb tunnel junction.

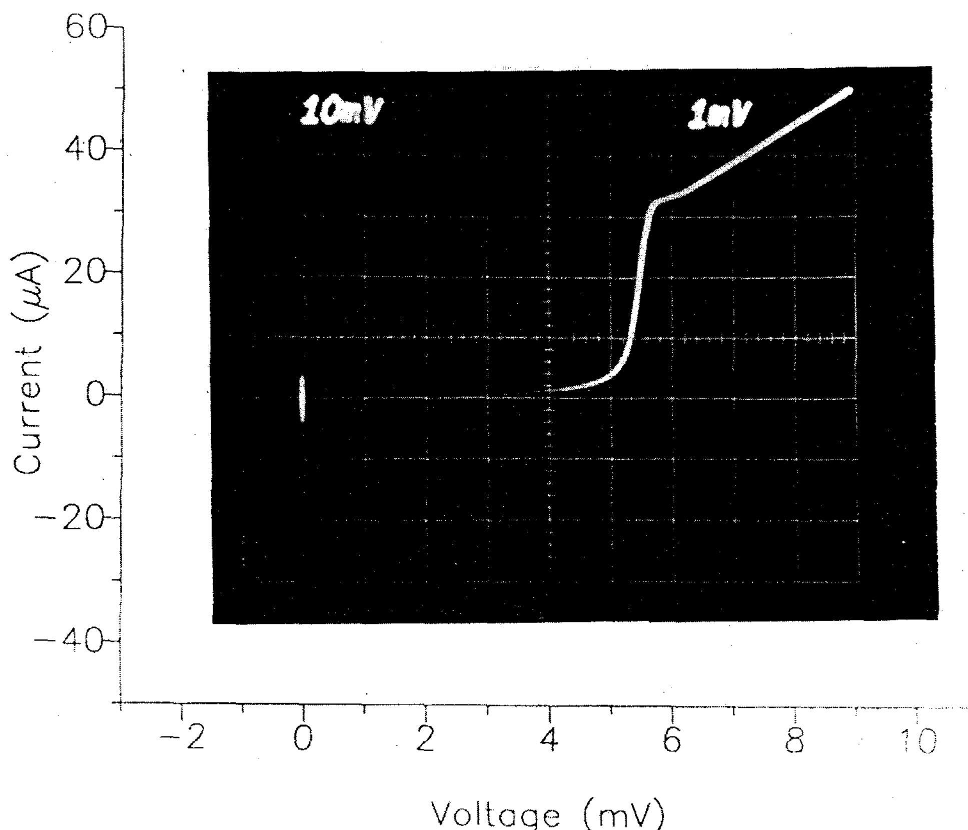

Figure 3.3 SIS I-V characteristic with an extremely large gap voltage.

Reduction of gap voltages from their maximum value is probably caused by a thin layer of non-B1 material at the interface of the barrier and the counter electrode. NbN/NbN junctions with barriers other than MgO have even smaller gap voltages than those with MgO barriers. The MgO barrier helps to stabilize the counter electrode; however, if a thin layer of the NbN is nonsuperconducting, the gap voltage will be reduced. Heating the substrate during NbN deposition makes stabilizing the B1 phase easier. This explains the exceptionally large gap voltage of the junction in Figure 3.3. NbN/native-oxide/Pb junctions typically show a large energy gap for the NbN base electrode; therefore, the reduction in the gap-sum voltage is probably caused by reduction of the counter-electrode energy gap, not the base electrode.

Observation of a gap-difference structure in the I-V characteristic of NbN/MgO/NbN junctions would help determine the source of gap reduction in these junctions; however, measuring the gap-difference voltage in NbN/MgO/NbN junctions is difficult. The energy-gap smearing broadens the gap difference structure. The gap-difference voltage is typically below the drop-back voltage and consequently is hard to observe. The difference structure can be easily confused with resonant tunneling structure in the I-V characteristic, such as Fiske (1964) steps.

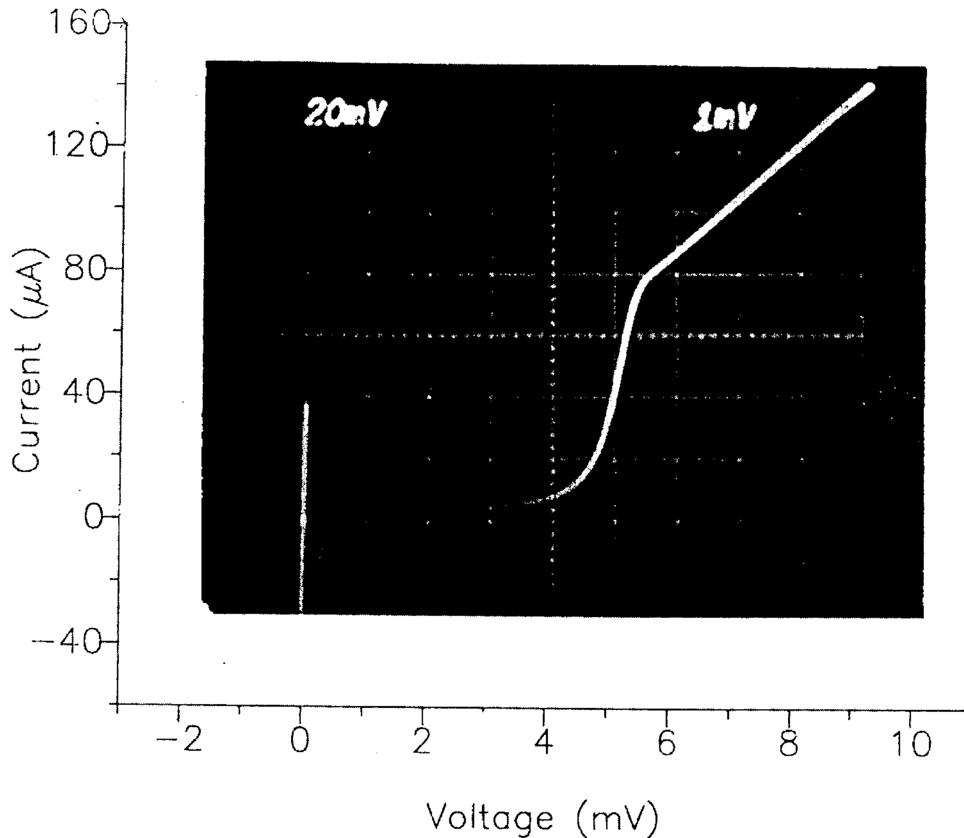

Figure 3.4 SIS I-V characteristic with a large gap voltage for an unheated substrate.

Gap-Voltage Smearing

In real junctions, the tunneling current turns on gradually near the gap voltage; this "gap-voltage smearing" is very important to mixer performance. As discussed in the first chapter, the voltage over which the current is a nonlinear function must be smaller than the voltage scale of the photon ($h\nu/e$) to get quantum behavior from SIS mixers. If the gap-voltage smearing is larger than the photon voltage scale, then conversion gain and quantum-limited performance are not possible. For a gap width of 1 meV, quantum behavior will occur above 240 GHz. The "gap width" is defined here as the difference in voltages at 90% and 10% of the current rise near the gap voltage. In our NbN junctions, the gap width varies from 0.6 meV to 2.0 meV. Figure 3.5 compares the two extreme cases of a narrow (0.6 mV) and smeared (1.6 mV) gap-voltage widths. Narrow gap widths are desired; unfortunately, no strong correlation between deposition conditions and gap width have been noted.

Subgap Resistance

Subgap resistance also affects mixer performance significantly. Current at the bias point contributes shot noise to the overall mixer noise (Tucker and Feldman, 1985). Additionally, subgap current rounds the I-V characteristic, which degrades mixer performance. Typical bias points for mixers are below the

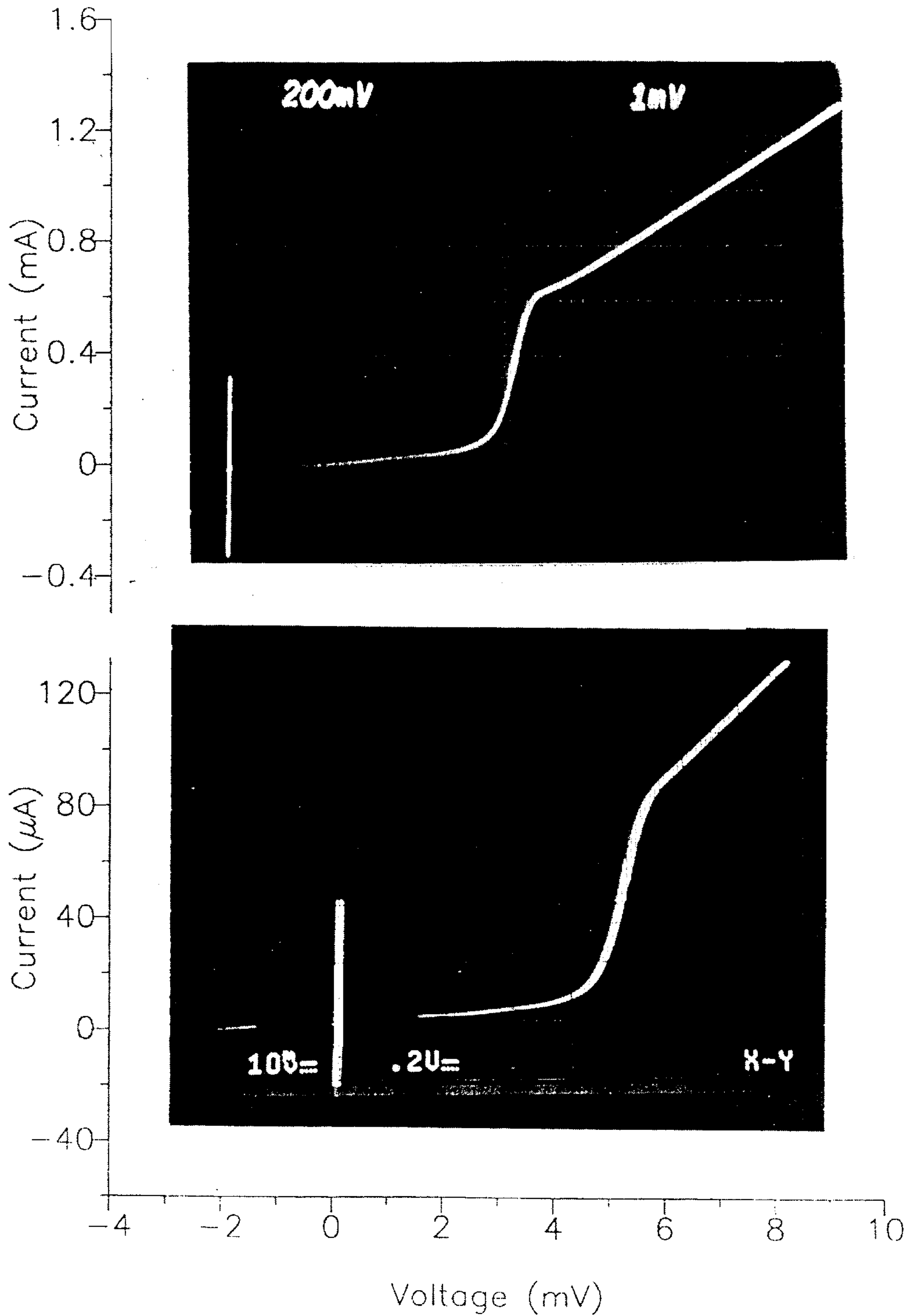

Figure 3.5 SIS I-V characteristics with a narrow (a) and broad (b) onset of tunneling at the gap voltage

gap voltage. The subgap resistance increases at half the gap voltage. The subgap resistance is measured at 3.0 mV, because it is a good indication of the resistance where a mixer would be biased even for junctions with small gap voltages. Junctions are characterized by the ratio of the subgap to the normal

state resistance. For junctions with R_nA products of 100 $\Omega\mu m^2$, the subgap-to-normal-state resistance ratio is typically 10, although for large R_nA junctions the ratio can be much higher, and for the lowest R_nA values, a ratio of 5 is more common. Figure 3.6 shows a junction with a subgap-to-normal-state resistance ratio of 16 and an R_nA product of 460 $\Omega\mu m^2$.

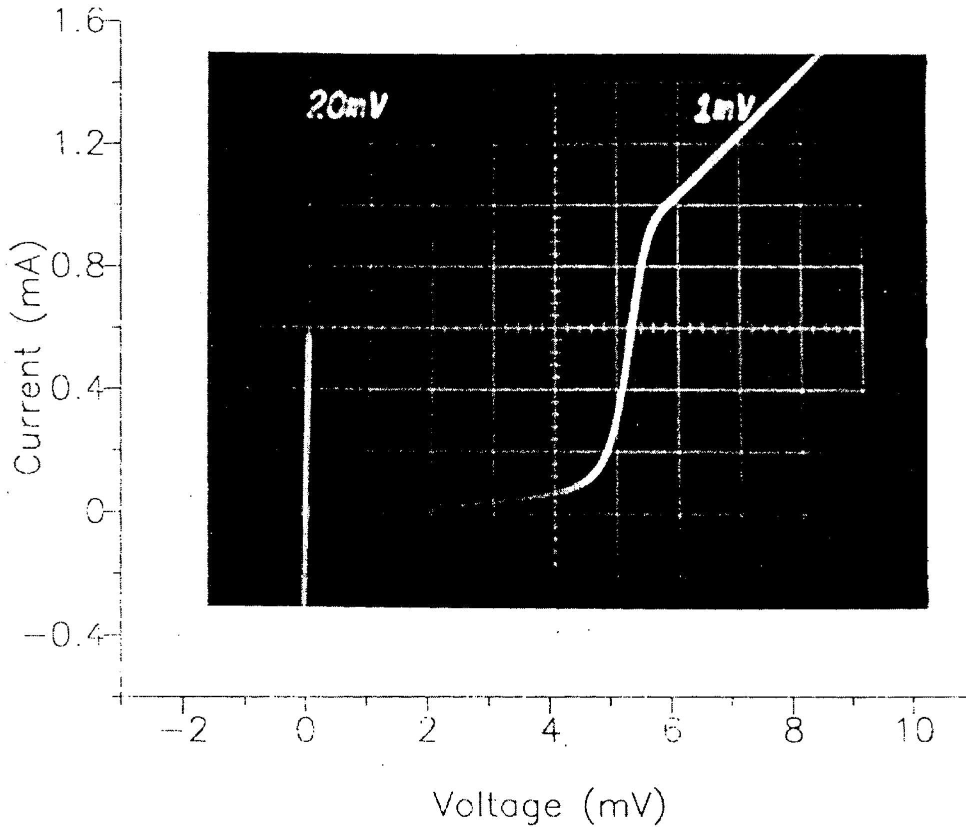

Figure 3.6 SIS I-V characteristic with a large subgap resistance.

Multiparticle and SIN tunneling were introduced in Chapter one as possible causes of subgap leakage. Here we will compare multiparticle tunneling and SIN tunneling as mechanisms for the leakage currents in NbN junctions. The purpose of this section is to explain the rise in subgap conduction at half the gap voltage, which is usually evident in NbN/MgO/NbN I-V characteristics.

Multiparticle tunneling is a mechanism that can explain the qualitative nature of subgap conduction in NbN/MgO/NbN tunnel junctions. Figure 3.7(a) shows the I-V characteristic predicted by Schrieffer and Wilkins (1963) for the subgap region of junctions exhibiting two particle tunneling. Figure 3.7(b) compares the subgap region of a typical NbN/MgO/NbN tunnel junction to the theoretical I-V characteristic. The two I-V characteristics are very similar, although the real I-V has a finite leakage below half the gap voltage, and the increase of current at half the gap voltage is not abrupt, because of gap-smearing. The qualitative agreement between the two-particle tunneling theory the NbN/MgO/NbN I-V characteristic is very good.

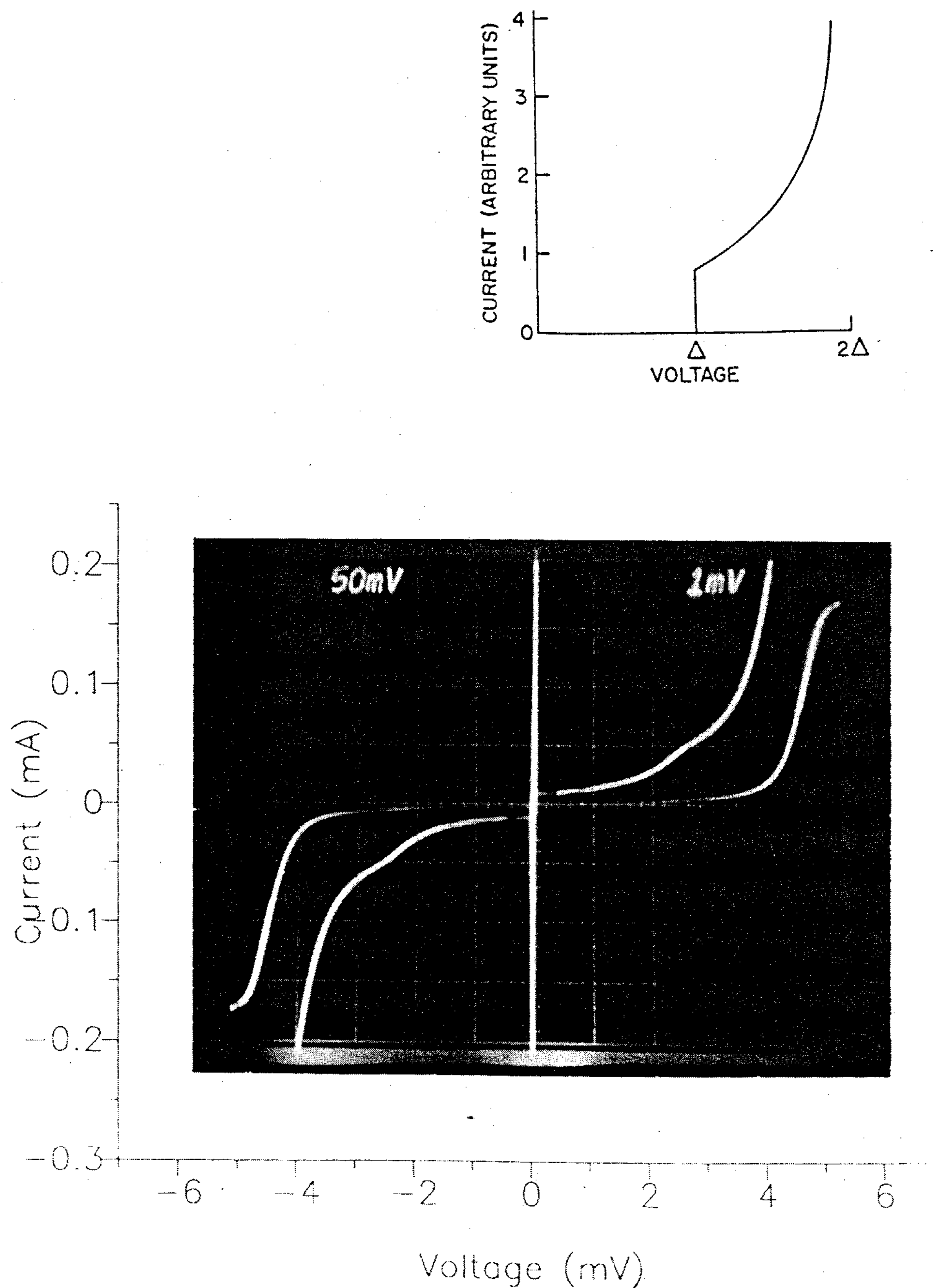

Figure 3.7 Multiparticle tunneling I-V characteristics. Figure (a) shows the I-V characteristic calculated from the theory of Schrieffer and Wilkins (1963) for the subgap region; Figure (b) compares this to an expanded view of the subgap region of an NbN/MgO/NbN tunnel junction.

As discussed in the first chapter, current can flow below the sum-gap voltage in tunnel junctions if two or more quasiparticles tunnel simultaneously. Typically, two quasiparticles tunnel simultaneously and form

a Cooper pair, or a Cooper pair breaks and both quasiparticles simultaneously tunnel into excited states. Both of these processes are shown in Figure 1.6. Because these processes rely on two or more particles tunneling together, they are lower-order processes; the probability of two-particle tunneling is T^2, where T is the transmission probability of a single quasiparticle. The ratio of the current rise at half the gap voltage to the current rise at the gap voltage is roughly equal to the transmission probability. For typical SIS tunnel junctions, like those described by Taylor and Burstein (1963), the rise of current at half the sum gap is less than 10^{-4} times the rise at the sum gap. In high current density (J_c = 10 kA/cm^2) NbN/MgO/NbN junctions, the current rise at half the gap voltage is typically 1/30th the current rise at the gap voltage.

To determine if multiparticle tunneling can explain this relatively large increase in current at half the gap voltage, consider a typical uniform square tunnel barrier. The transmission probability is

$$T = \exp\left[\frac{-4\pi d\sqrt{2m\phi}}{h}\right], \tag{3.1(a)}$$

where d is the barrier thickness, ϕ the barrier height, m the mass of the electron, and h Planck's constant. The R_nA product for the junction is then,

$$R_nA = \frac{h^2 d}{e^2 T\sqrt{2m\phi}}, \tag{3.1(b)}$$

where e is the charge on an electron (Cohen *et al.*, 1962). Assume that the barrier height is 1 eV and the barrier thickness is 0.7 nm, then $T = 4.5 \times 10^{-4}$, and $R_nA = 52\Omega\mu m^2$. This is equivalent to a critical current-density of 5.4 kA/cm^2. The magnitude of the current-density rise at half the gap voltage is $J_\Delta = J_{2\Delta} \times T$, where $J_{2\Delta}$ is the current-density rise at the gap voltage. The current-density rise at the gap voltage is equal to the critical current density within a factor of $\pi/4$; the two values are assumed to be equal for this argument. For the junction described above, the current density rise at half the gap voltage would be 1/2000th the rise at the gap voltage, which is much smaller than the observed rise in NbN/MgO/NbN junctions.

Schrieffer and Wilkins (1963) suggested a barrier model that leads to larger multiparticle tunneling current densities and that may be appropriate for MgO barriers on NbN. Consider a nonuniform barrier composed of thick regions separated by small-area, thin regions. Two-particle tunneling will occur primarily through the thin regions of the barrier. Single-particle tunneling will occur through both thin regions and the larger area thick regions. This simple model may be appropriate for MgO barriers on NbN, because MgO grows on NbN in the Stranski-Krastanov mode (LeDuc *et al.*, 1987). The first monolayer of MgO will coat the entire NbN surface, and subsequent MgO layers will grow in islands. As the barrier is made thicker, the MgO islands coalesce. For thin MgO barriers it is reasonable to expect the barrier to be composed of thick islands (two or three monolayers) separated by regions of monolayer coverage. The

monolayer region is assumed to be 0.4 nm thick and to cover 1% of the surface; the thick region is assumed to be 0.8 nm thick and to cover 99% of the surface. The current density and transmission probability for the two regions are

$$T_1 = 1.6 \times 10^{-2},\ R_nA_1 = 0.78\ \Omega\mu m^2,\ J_c^1 = 360\ kA/cm^2,\ \text{and}$$

$$T_2 = 2.7 \times 10^{-4},\ R_nA_2 = 93.\ \Omega\mu m^2,\ J_c^2 = 3.0\ kA/cm^2,$$

where the subscript 1 refers to the thin region and the subscript 2 refers to the thick region. The average critical current density for the junction is

$$J_c^{average} = 0.01 \times J_c^1 + 0.99 \times J_c^2 = 6.6\ kA/cm^2.$$

The current density rise at half the sum gap is

$$J_\Delta = 0.01 \times J_c^1 \times T_1 + 0.99 \times J_c^2 \times T_2 = 58\ A/cm^2.$$

The ratio between current rise at half the sum gap and the sum gap is 1/110. To increase the fraction of multiparticle tunneling even further, the barrier height or thickness of the thin regions must be reduced.

This analysis shows that the two-particle tunneling currents can be fairly large if the tunnel-barrier thickness is not spatially uniform. MgO barriers on NbN are not thought to be as uniform as oxidized metal barriers, because the growth kinetics of the two types of barriers is very different. Oxidized metal barriers tend to grow uniformly, whereas MgO is thought to grow first in a uniform monolayer with subsequent layers forming MgO islands. On the basis of this growth mode, multiparticle tunneling offers a plausible explanation for the leakage currents in NbN tunnel junctions. If this explanation is correct, it suggests that small, very thin areas in the tunnel barrier contribute significantly to the total conduction in the tunnel junction.

A nonuniform barrier will have two important effects on mixer performance. The increase in subgap conductance will lead to worse mixer performance. The specific capacitance at a given critical current density will be slightly lower for the nonuniform barrier. As an example for the two barriers analyzed so far, the uniform barrier has a 13% larger capacitance than the nonuniform barrier.

SIN tunneling is another possible explanation for leakage currents in NbN/MgO/NbN tunnel junctions. An SIN I-V characteristic has a conductance maximum at half the gap voltage, so like multiparticle tunneling it can explain the qualitative shape of the subgap region of NbN/MgO/NbN I-V characteristics. This theory is much simpler than multiparticle tunneling. If some region of either electrode is nonsuperconducting, then SIN tunneling will occur. SIN tunneling typically does not occur in long coherence-length materials, like

Pb, because the the nonsuperconducting regions are smaller than the coherence length. Nonsuperconducting regions that are smaller than the coherence length will only reduce the average gap, and will not contribute to SIN tunneling. In NbN tunnel junctions, nonsuperconducting areas 5-10 nm across would cause SIN tunneling. SIN tunneling offers a simple explanation for the subgap leakage in NbN tunnel junctions.

There is evidence to suggest that multiparticle tunneling theory is the correct explanation of excess leakage in NbN/MgO/NbN tunnel junctions. Junctions with large R_nA products have higher subgap-to-normal-state resistance ratios than junctions with low R_nA values. The ratio of SIN tunneling to SIS tunneling in a junction is independent of barrier thickness, whereas multiparticle tunneling currents will decrease relative to normal quasiparticle tunneling for thicker barriers. If the MgO islands grow together to virtually eliminate the monolayer regions, then almost no multiparticle tunneling would be expected. A good method of verifying that multiparticle tunneling is occurring would be to observe the effect of three-particle tunneling on NbN/MgO/NbN I-V characteristics. This is somewhat difficult since three-particle tunneling is proportional to T^3; however, if a conductance increase could be seen at $\Delta_\Sigma/3e$ or $2\Delta_\Sigma/3e$, it would be fairly conclusive evidence of multiparticle tunneling.

I-V Characteristics for High-Speed Tunnel Junctions

High-frequency mixers will use junctions having extremely small R_nA values (10 $\Omega\mu m^2$). We now discuss the properties of these junctions as compared to junctions with more typical R_nA values (100 to 1000 $\Omega\mu m^2$). The largest difference is that the ratio of the subgap resistance to the normal resistance is larger for small R_nA product junctions. The drop-back voltage is larger in small R_nA product junctions; this effect was described in the introduction. The gap-sum voltage is independent of the R_nA product with one exception. For small R_nA values, self-heating by currents in the junction can cause the gap-voltage smearing to be reduced. This effect is caused by the energy gap being reduced by an increase in quasiparticles in the junction area. The quasiparticles are injected into the electrode as they tunnel across the barrier. The excess of quasiparticles implies an increase in temperature, although not necessarily an equilibrium distribution. The increase in temperature decreases the energy gap with increasing bias current. Figure 3.8 shows an I-V characteristic, where gap heating is evident. The heat dissipated in the junction is roughly equal to V_g^2/R, so energy-gap heating is evident only in low-resistance junctions; therefore, small R_nA product submicron junctions will not exhibit this problem.

The only major differences between very low R_nA junctions and the junctions used for RF testing in this thesis are the lower subgap-to-normal-state resistance ratio and the larger drop-back voltage. Because there are only small differences, estimates can be made on how NbN/MgO/NbN junctions will work as mixers above the frequencies at which we have tested. The rounding of the I-V characteristic caused by the increased subgap leakage will have very little effect at higher frequencies, because the voltage scale of

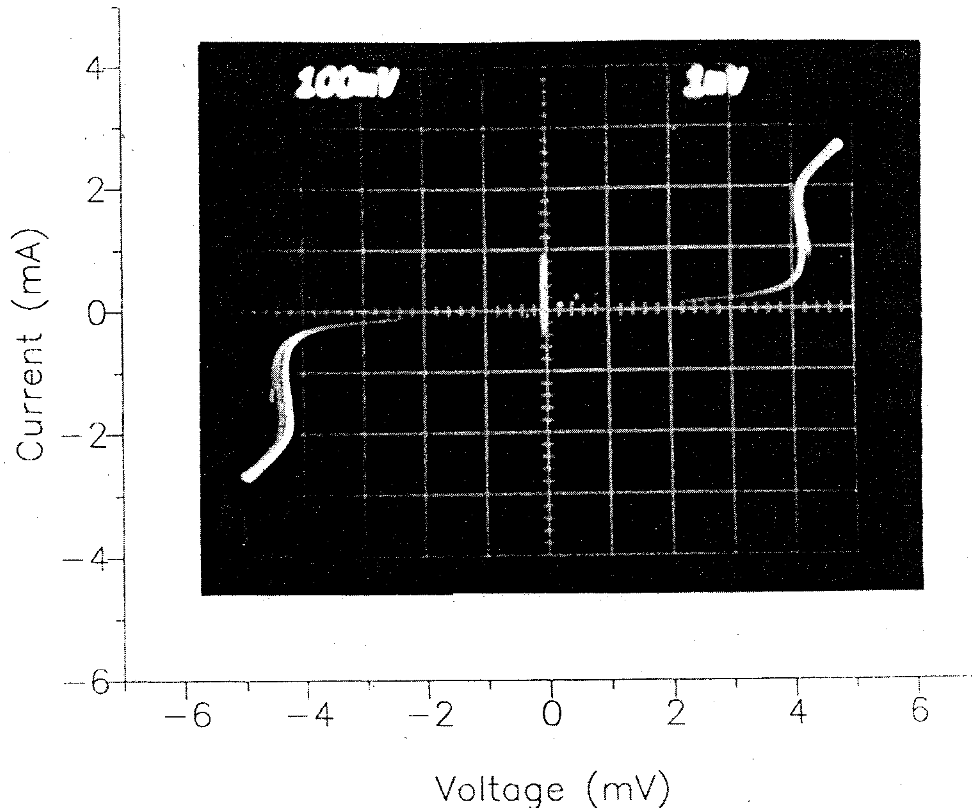

Figure 3.8 SIS I-V characteristic showing the effect of self-heating on the gap voltage.

the photon ($h\nu/e$) will be larger. The drop-back voltage is typically around 1.5 mV. This is much lower than the gap voltage and should not interfere with mixer tests below 1200 GHz. The mixer tests made at 205 GHz are a good indication of how submicron, low R_nA product junctions will work as mixers at higher frequencies.

I-V Characteristics as a Function of Temperature

One of the most attractive features of NbN is the possibility of operating NbN junctions on closed-cycle refrigerators near 10 K; therefore, measuring tunnel junction I-V characteristics as a function of temperature is important. Figure 3.9 shows an I-V characteristic for a NbN/MgO/NbN tunnel junction at various temperatures below T_c. The Josephson critical-current, energy-gap and subgap resistance are plotted as a function of temperature for a different junction in Figure 3.10. The energy gap and critical current are compared to BCS theory. The fit of the energy gap to theory is extremely good. The critical current is partially suppressed by noise in the test apparatus, so the fit of critical current to the BCS theory is not as good as the fit of the energy gap to theory. From Figures 3.9 and 3.10, we see that the I-V characteristic is still very nonlinear at 10 K. An analysis of the practicality of using NbN junctions near 10 K will be made in Chapter four.

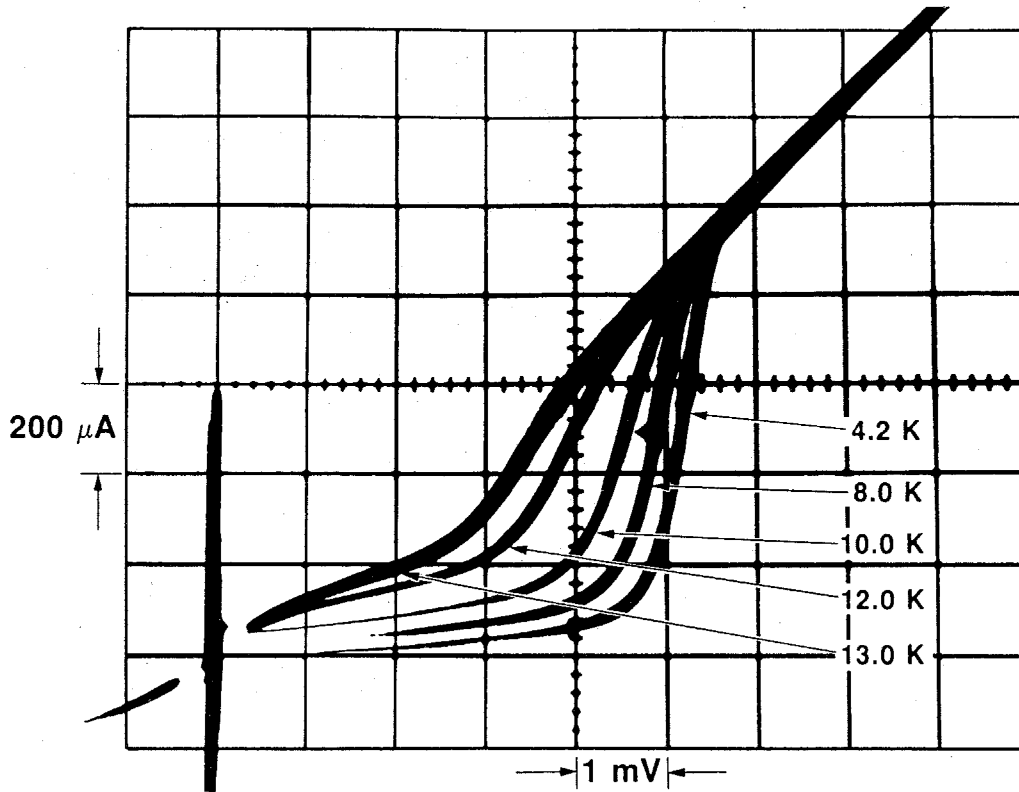

Figure 3.9 SIS I-V characteristics at different temperatures.

Switching in Tunnel Junction Electrodes

A final feature observed in I-V characteristics is switching of the electrodes from the superconducting state into the normal state as the DC bias level is raised. Figure 3.11 shows an I-V characteristic in which switching is present. The switching is seen as a hysteretic jump in voltage. There are two possible explanations for this phenomenon. The local current flow could be exceeding the critical current density of the NbN film, or quasiparticle injection could be driving the counter electrode into the normal state. These two explanations are now discussed.

The simplest explanation for switching is that the current in the wiring electrode is exceeding the critical current of the NbN as it crosses the edge of the trilayer or the edge of the mesa planarization layer. The switching occurs typically for currents of 1 mA. If the wiring level is 5 μm wide and 50 nm thick, 1 mA corresponds to a critical current density of 4×10^5 A/cm^2. This value is roughly 10 times lower than measured critical current densities; however, for very thin layers crossing a step edge, the critical current density may be reduced from its normal value.

A more complex explanation for switching relies on quasiparticle injection. As the bias is increased

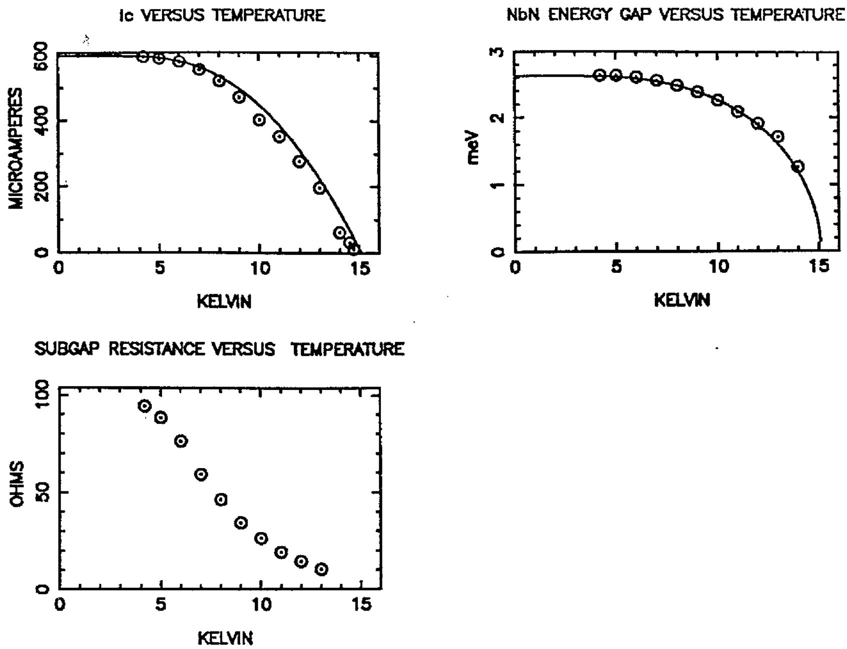

Figure 3.10 I-V properties as a function of temperature. Shown in Figure (a) is the junction critical current as compared to BCS theory. Shown in Figure (b) is the NbN energy gap as a function of temperature as compared to BCS theory. Shown in Figure (c) is the subgap resistance as a function of temperature.

above the gap voltage, quasiparticles are injected into the counter electrode. These quasiparticles represent nonequilibrium heat, because they can be converted into phonons and the phonons back in to quasiparticles. The phonons can be removed from the junction area by thermal conduction, but the thermal conductivity of superconductors is small. The quasiparticles can also diffuse away from the junction area, but this can be limited by the step coverage at the mesa edge. If the quasiparticle level is too high, the electrode will go normal. The correct explanation is not known, but smoother step edges, better planarization and thicker wiring electrodes help minimize this problem.

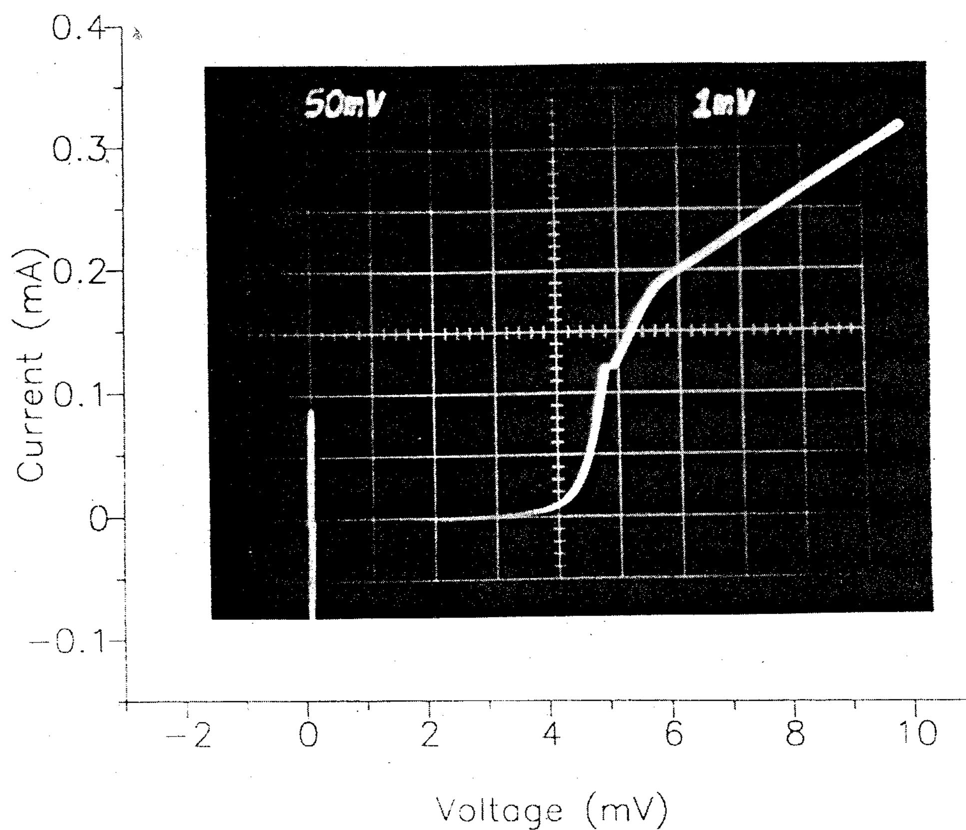

Figure 3.11 SIS I-V characteristic showing electrode switching.

Table 3.1 I-V characteristic summary

Figure no.	Area (μm^2)	R_n (Ω)	R_{subgap} (Ω)	Δ_Σ (meV)	I_c (μA)
3.3	16	173	6.0 k	5.6	4.0
3.4	4	64	820	5.0	40
3.5 (a)	30	7.8	105	5.1	340
3.5 (b)	1	96	1150	5.0	24
3.6	16	5.5	88	5.2	610
3.7	16	29	461	4.5	80
3.8	16	1.56	10.7	>4.2	1400
3.11	16	30	714	4.75	100
3.24	1	64	800	4.75	13
3.27	16/10	155	2.1 k	4.6	170
3.28 (a)	16/100	2.0 k	28 k	4.6	132
3.28 (b)	4/100	2.8 k	25 k	4.45	93
4.1	1	97	1.9 k	4.8	10

C. SQUID Measurements

The embedding impedance of an SIS junction has a strong effect on mixer performance. The embedding impedance will depend on three factors: the mixer block design, the junction capacitance and any tuning circuits integrated with the junction. Superconducting quantum interference devices (SQUIDs) are used to measure the junction capacitance and superconducting microstrip line inductance. The microstrip line properties need to be known to design integral tuning circuits accurately. The NbN magnetic penetration depth is calculated on the basis of the microstrip line inductance. The magnetic penetration depth is important because it is a basic superconducting property, and it is used to design superconducting circuits.

A DC SQUID consists of a superconducting loop with two junctions in it. As derived in Appendix A, the critical current of the two junctions in parallel is a periodic function of the magnetic flux within the loop. The period for the critical current is called a flux quantum or fluxon ($\Phi_0 = h/2e$). Microstrip line inductance, magnetic penetration depth and junction capacitance are measured using SQUIDs. The importance of these values is discussed before the measurement techniques and the results are presented.

Accurate characterization of superconducting microstrip line propagation velocity ($\bar{c}$) and impedance (Z) is necessary for the design of high-frequency circuits, like tuning stubs. The microstrip line inductance can be measured with a SQUID. If the propagation velocity is also known, then the microstrip line impedance can be calculated ($Z = \bar{c}L$, where L is the inductance per unit length). The propagation velocity of a microstrip line is measured by connecting a junction to an open-ended microstrip line and observing the resonant structure on the I-V characteristic. Propagation velocity measurements will be presented in the RF testing section.

The magnetic penetration depth affects the design of superconducting circuits. The Meisner effect (Meisner and Ochsenfeld, 1933) is the hallmark of superconductivity. As a superconductor is cooled below its transition temperature, magnetic flux is expelled from within the bulk of the superconductor; however, the magnetic flux penetrates the surface of the superconductor with a characteristic length λ (called the superconducting penetration depth). The penetration depth is typically small (10 to 500 nm), so for macroscopic superconducting bodies, the flux is largely expelled. For thin superconducting films, the penetration depth may be roughly the same as the film thickness; to characterize these structures, the penetration depth needs to be known accurately.

The penetration depth has a large effect on microstrip line inductance and propagation velocity. The electric fields in the transmission line are mostly confined to the dielectric thickness (t). In a normal metal microstrip line, the magnetic fields are also confined to the dielectric thickness, and the velocity of propagation is roughly $c/\sqrt{\epsilon_r}$, where c is the speed of light in a vacuum, and ϵ_r is the relative dielectric constant. In a superconducting microstrip line, the magnetic fields are confined to the dielectric thickness

and one penetration depth into each superconductor. This leads to a propagation velocity of roughly $c\sqrt{t/(\epsilon_r \times (t+2\lambda))}$. If the dielectric thickness is small compared to the penetration depth, a superconducting microstrip line will be a slow wave transmission line. To design superconducting circuits accurately, the penetration depth needs to be known accurately.

The most important value measured using SQUIDs is the specific capacitance (c=C/A, where C is the junction capacitance and A the junction area). The RC speed of NbN junctions is the most significant limitation on their high-frequency performance. If the normal resistance, junction area and specific capacitance as a function of R_nA are known, the RC product can be calculated as $RC=R_nA \times c(R_nA)$. The resistance is easily measured, and the junction area can be measured using a scanning electron microscope. In order to calculate junction RC roll-off frequencies, the function $c(R_nA)$ must be determined.

SQUID Design

The SQUID design used in our experiments is a microstrip line over a ground plane with two junctions connecting the microstrip line to the ground plane. The current and voltage leads for the SQUID are symmetrically placed between the two junctions. This design is based on the design of Magerlain (1981). He used this design to measure the capacitance of Pb-alloy and Nb/Pb-alloy junctions. Figure 3.12 shows a diagram of the SQUID and an equivalent electrical schematic. Because of the circuit's geometry, the inductance of the top electrode ($2L_1$) is much larger than the inductance of the ground plane ($2L_2$). Typically, the ground plane and top electrode are 200 to 400 nm thick, the dielectric layer is 120 nm thick, the microstrip line 4 μm wide, and the junctions are 80 μm apart.

Microstrip Line Inductance

The inductance of the microstrip line is measured by running a control current along the top electrode while measuring the critical current of the two parallel junctions. The control current generates a magnetic flux in the SQUID loop ($\Phi = 2L_1 I_{control}$, where Φ is the flux in the loop and $I_{control}$ is the control current). The critical current of the two junctions in parallel is a periodic function of the flux in the SQUID loop, so the inductance is

$$2L_1 = \Phi_0/\Delta I_{control}, \qquad 3.2$$

where $\Delta I_{control}$ is the period of the critical current modulation. The circuit used to measure the critical current versus control current is described in Appendix C. The simple measurement of the SQUID critical current versus control current is all that is necessary to measure microstrip line inductance. This measurement is also the basis of measuring NbN penetration depths and junction capacitance as will be described below.

Magnetic Penetration Depth

The penetration of magnetic fields into the microstrip line electrodes causes the inductance of the line

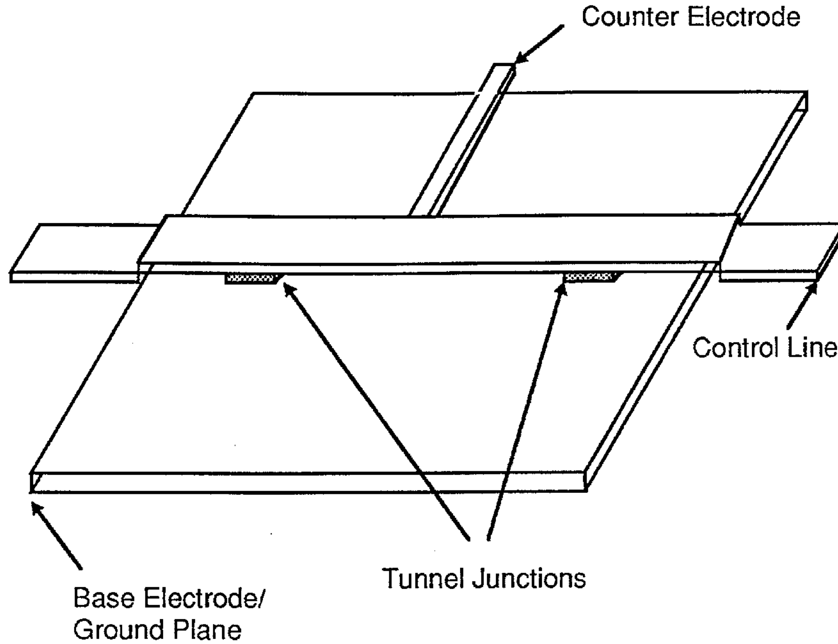

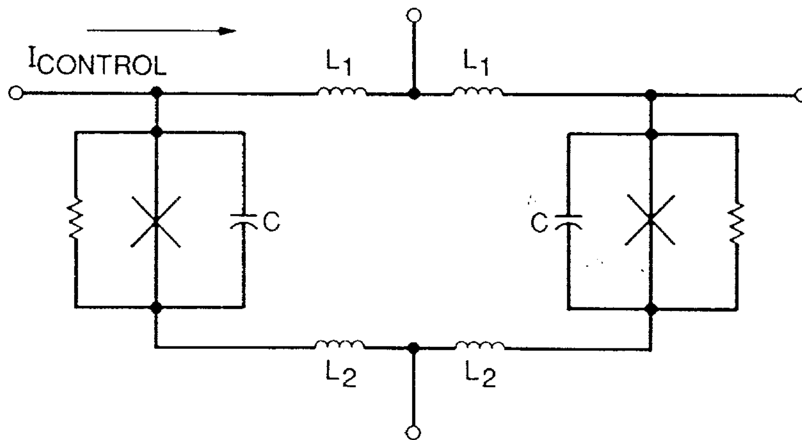

Figure 3.12 Sketch and schematic circuit diagram for a SQUID.

to be larger than that of a normal-metal microstrip line. The inductance of a superconducting microstrip line is

$$L_{sup} = \frac{\mu_0 l\kappa}{w}\left[t + \lambda_1 \coth\frac{\lambda_1}{d_1} + \lambda_2 \coth\frac{\lambda_2}{d_2}\right], \quad 3.3\ (a)$$

and the inductance of a normal metal microstrip line is

$$L_{sup} = \frac{\mu_0 l\kappa t}{w}, \quad 3.3\ (b)$$

where μ_0 is the permeability of free space, l is the line length, κ is the fringing factor, w is the line width, t is the dielectric thickness, and d_1 and d_2 are the electrode thicknesses (Van Duzer and Turner, 1981). The

penetration depth is determined by measuring the SQUID inductance and solving Equation 3.3 (a) for the penetration depth. The dimensions of the SQUID must be known accurately, and Equation 3.3 (a) must be solved numerically, because it is a nonlinear equation.

The magnetic penetration depth was measured for NbN films deposited on unheated and heated substrates. The results of these measurements are listed in Appendix D and summarized below. The mean value for the measured magnetic penetration depth of NbN deposited on unheated substrates is 380 nm with a standard deviation of ±60 nm. This value differs significantly from the published value of 280 nm (Shoji *et al.*, 1987); however, the mean value for the magnetic penetration depth of NbN deposited on heated substrates is 280 nm with a standard deviation of ±30 nm. The transition temperature of the films deposited on heated substrates was 15.8 K, whereas the transition temperatures of the films deposited on unheated substrates were typically 14.5 K. The reduction in penetration depth is due to either this improvement in the transition temperature, or the larger crystallite size of the heated films.

The scatter in the penetration depth measurements was quite large, because the film thicknesses were not measured sufficiently accurately. Thickness measurements were made on one chip from each wafer. The wafers were 3" in diameter, and the NbN thickness varied considerably across the wafer; therefore, the measurements were less accurate than they could have been. Future tests will include accurate thickness measurements of the NbN and dielectric layers for each chip tested.

Specific Capacitance

Junction capacitance is measured by observing the effect on the I-V characteristic of the LC resonance formed by the junction capacitance and the SQUID loop inductance. Josephson junctions oscillate at a frequency proportional to the bias voltage ($\nu = 2eV/h$). A constant voltage step will be evident corresponding to the LC resonance frequency. The voltage step is at

$$V_r = h/4\pi e \times \sqrt{1/LC}, \qquad 3.4$$

where V_r is the resonant voltage, $L = 2(L_1 + L_2) \approx 2L_1$, and C is the junction capacitance. Combining Equations 3.4 and 3.2, we have

$$C = \frac{\Delta I_{control}}{(2\pi V_r)^2} \times \Phi_0. \qquad 3.5$$

The measurement of junction capacitance involves both the critical-current versus control-current plot and the junction I-V characteristic at low voltage levels; an example of these measurements is shown in Figure 3.13. To calculate the specific capacitance, the junction area must also be known.

There are several possible sources of error in this measurement. The exact value of the resonant voltage step is difficult to measure. The capacitance measured includes a parasitic capacitance between the

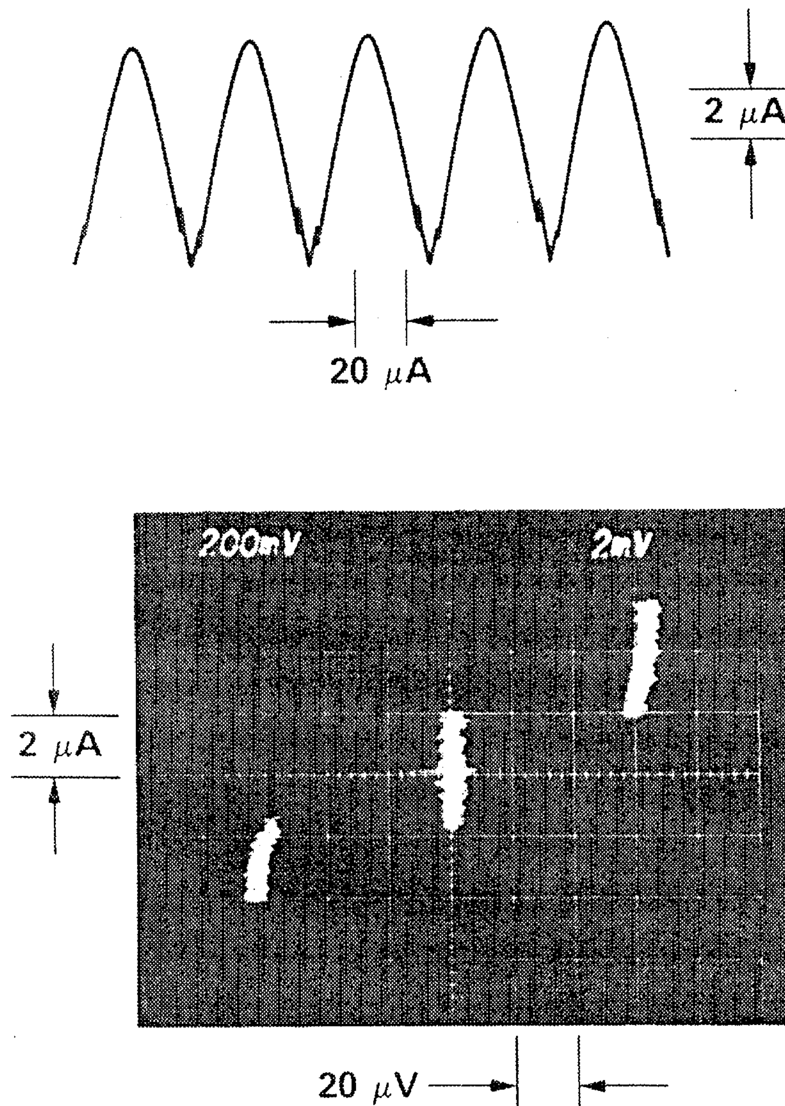

Figure 3.13 Modulation curve and voltage resonance for a SQUID. Figure (a) shows the critical current as a function of control current for a SQUID. Figure (b) shows an I-V characteristic with an LC resonance step for a SQUID.

wiring electrode and the ground plane. The ground-plane inductance (L_2) must be estimated and added to the wiring electrode inductance.

The parasitic capacitance between the wiring electrode and the ground plane can be estimated and subtracted from the total capacitance measured. In the case of the mesa junction SQUIDs, the parasitic capacitance was estimated to be 80 fF. The parasitic capacitance of the cross-line SQUIDs was generally smaller than the mesa junctions and depended on the actual SQUID dimensions. Estimating the parasitic capacitance adds some uncertainty to the specific capacitance measurement.

Thus far, the ground-plane inductance has been ignored, because it is small compared to the top-electrode inductance. The ground-plane inductance is measured by running a control current through the ground plane. For the cross-line junctions measured, the ground-plane inductance is five percent of the top-electrode inductance. This inductance can be corrected for, and it does not add significant error to the measurements.

The largest error in this measurement comes from measuring the resonant voltage (V_r). This error is a particular problem, because the capacitance depends on the resonant voltage squared. The resonant voltage steps are at small voltage and current levels (typically 1 to 10 μA and 40 to 80 μV). The step is below the drop-back voltage, so thermal and instrumental noise can switch the junction off the voltage step into the zero voltage state or finite voltage state. The leads to the SQUID are filtered to minimize this problem.

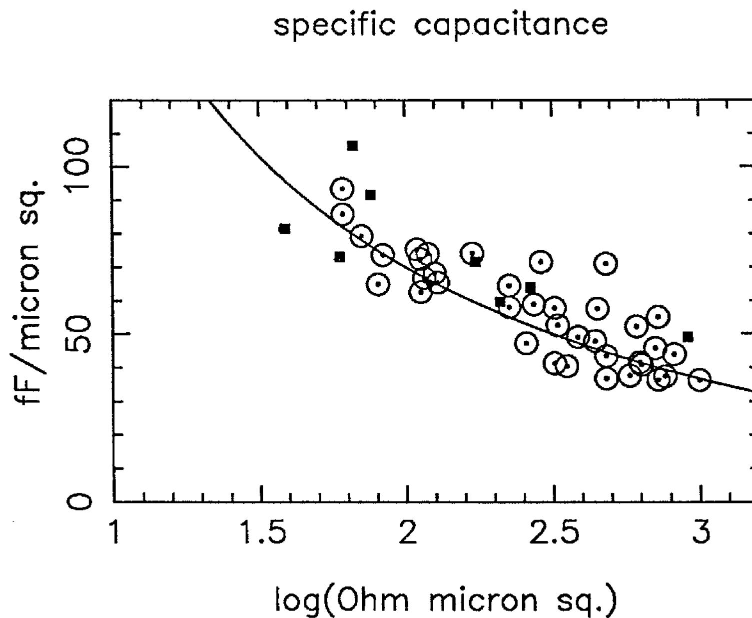

Figure 3.14 Specific capacitance versus log(R_nA). The open circles are data taken with x-line junctions, and the solid squares are data taken with mesa junctions.

All of the SQUID data is tabulated in Appendix D, and the specific capacitance is plotted as a function of log(R_nA) in Figure 3.14. The open circles in this plot represent SQUIDs fabricated with the cross-line process, and the solid squares represent older data for SQUIDs fabricated with the mesa junction process. The specific capacitance is fit to a simple model. The formula for R_nA is given by Equations 3.1 (a) and (b). If the exponential term in Equation 3.1 (a) is dominant, the log of R_nA is proportional to the barrier thickness; therefore, the specific capacitance is roughly proportional to the inverse of log(R_nA). In Figure 3.14 the data are fit to $c = \alpha/\log(R_nA) + \beta$, where α and β are fitting parameters. Despite the scatter in

the data, a trend is evident, and the fit to the model is fairly good.

Barrier Uniformity

Information about barrier uniformity can also be obtained from SQUID measurements. If the SQUID critical current is measured over a large range of control current, the magnitude of the critical current maxima will be modulated as a function of control current. The modulation is caused by the individual junction critical currents' being modulated by the magnetic field. If the junction barrier is uniform, the modulation function will be sin(x)/x with x = constant × $I_{control}$ (Van Duzer and Turner, 1981). Plotted in Figure 3.15 are this function and data from a SQUID. The fit to theory is fairly good, indicating that the MgO barrier is uniform.

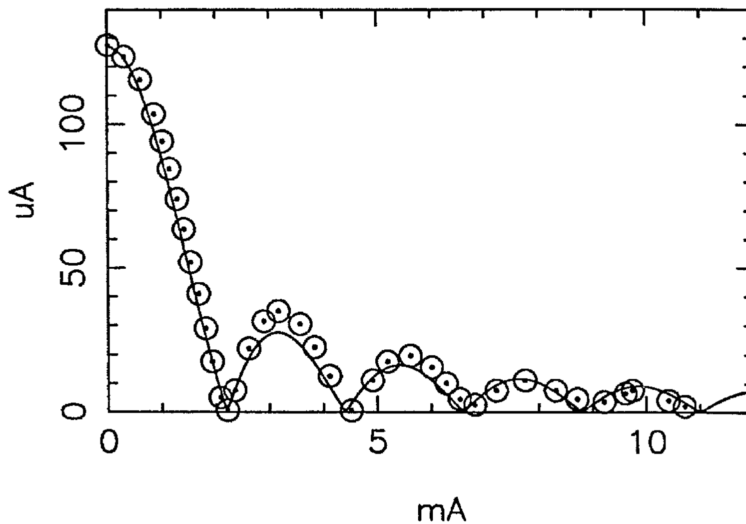

Figure 3.15 SQUID critical current maxima versus control current.

D. RF Testing

This section describes tests made of NbN/MgO/NbN tunnel junctions as mixers at 205 GHz. The mixer and receiver test setup are described. Using this test setup, the mixer-noise temperature and conversion gain can be measured accurately. The method for calculating the mixer properties is discussed. The mixer block used cannot completely tune out the capacitance of the NbN tunnel junctions. A microstrip line stub is integrated with the tunnel junction to help tune out the capacitance. The design of this stub is presented along with a description of how the stubs characteristics are measured. The mixer results are given as a function of the tuning stubs' properties. There is some evidence of a temperature-dependent loss mechanism in these stubs. Possible loss mechanisms are analyzed both experimentally and theoretically.

The test frequency of 205 GHz was chosen as a compromise between several factors. At lower frequencies, the junction capacitance is a lesser problem, but the rounding of the I-V characteristic limits mixer performance. At higher frequencies, test equipment like LO sources are more complicated, and the junction capacitance is increasingly hard to tune out; however, rounding of the I-V characteristic is a lesser problem, and the larger gap eliminates problems with the drop-back voltage, which are seen in Pb or Nb junctions at these frequencies. At the chosen frequency, ωRC will be roughly 6 for a 1 μm^2 50 Ω junction. The capacitance is large enough that it must be tuned out effectively to get good mixer performance. Inductive-tuning stubs are integrated with the tunnel junctions get good mixer performance. At 205 GHz, the voltage scale of the photon (0.8 mV) is roughly equal to the voltage range of the current nonlinearity. With this degree of rounding, some quantum effects like photon-assisted tunneling steps, and conversion gain peaks corresponding to these steps are expected; however, extreme quantum effects like negative differential resistance, and infinite available conversion gain are not expected. Successful testing at this frequency will lead to better understanding of the difficulties associated with NbN junctions, and will make future testing of submicron NbN junctions at higher frequency much easier.

Receiver Design

The receiver design used for our tests is now described. There are several important aspects to the receiver used. The mixer block design has been used before with lead-alloy tunnel junctions. The noise temperature of the receiver with lead-alloy junctions is one of the best reported values at 230 GHz. The lead-alloy mixer results can be used as a baseline for comparison with NbN mixer results. Finally, the IF components connecting the mixer to the room temperature IF amplifiers (called the IF chain) are designed to allow accurate measurement of the mixer-noise temperature and the mixer conversion gain. Mixer-noise temperature is more fundamental than the receiver-noise temperature, because it is independent of the IF amplifiers properties.

The mixer block used is nearly identical to that of Ellison and Miller (1987). The mixer block

consists of a full height waveguide with a noncontacting backshort and E plane tuner. The E plane tuner is half a guide wavelength in front of the junction. The junction is mounted across the waveguide in a channel. There is an integral low-pass filter on the junction chip, which consists of alternating high and low impedance sections one-quarter wavelengths long at 230 GHz. The filter reduces RF losses down the IF channel. The IF connection to the chip is made at the end of this filter. The mixer and receiver test apparatus were assembled by W. R. McGrath. The McGrath mixer block has two major differences from the Ellison design. A dual mode feed horn is used instead of a scaler feed horn. A symmetric choke structure is used for the SIS chip; the junction sits in the center of the waveguide. In the original Ellison mixer, the junction is at one edge of the waveguide with the junction grounded at the other edge of the waveguide. The symmetric choke structure reduces a resonance in the mixer block (Büttgenbach *et al.*, 1990).

Extensive receiver tests were made with both the Ellison and McGrath mixer blocks using Pb alloy junctions fabricated by R. E. Miller at ATT Bell Labs. Typical, double-sideband receiver-noise temperatures for this block at 230 GHz are 100 K, although receiver-noise temperatures as low as 65 K have been measured. No accurate mixer-noise measurements have been made with Pb junctions in the McGrath block; however, the IF amplifier's contribution to the noise temperature with a LHe cooled HEMT amplifier is estimated to be 5 to 20 K. This implies that the mixer-noise temperature is typically 90 K.

Mixer Measurement Technique

This section describes the experimental techniques used to measure mixer and receiver properties. Receiver-noise temperature measurements are typically made by observing the receiver's response to black-body signals. To measure receiver noise, a total power meter is hooked up to the IF output port of the receiver, and two different-temperature black bodies are coupled to the input of the receiver. The black bodies are usually at room temperature and 77 K. The power emitted by the black-body loads can be calculated from Planck's law,

$$P = \frac{h\nu B}{e^{h\nu/k_B T} - 1}, \tag{3.8(a)}$$

where B is the measurement bandwidth. Because $h\nu \ll k_B T$, this expression is frequently reduced to

$$P = k_B B T. \tag{3.8(b)}$$

Equation 3.8(b) simplifies the calculation of mixer- and receiver-noise temperatures considerably. The difference in these two equations is important only when very low-mixer noise temperatures are obtained. Measurements made for this thesis use Equation 3.8(a). From the two pairs of RF and IF signal powers, the IF power out for no signal power incident on the mixer can be extrapolated; this is referred to the

input of the receiver to obtain P_{noise}. The receiver-noise temperature is $T_r = P_{noise}/k_B B$. In the simple case where 3.8(b) is used to relate power to temperature, the receiver temperature is

$$T_r = \frac{T_{RF}^{hot} - Y T_{RF}^{cold}}{Y - 1}, \text{ where} \tag{3.9}$$

$$Y = P_{IF}^{hot}/P_{IF}^{cold},$$

T_{RF}^{hot} is the temperature of the RF hot load, T_{RF}^{cold} is the temperature of the RF cold load, P_{IF}^{hot} is the IF power out with the RF hot load at the receiver input and P_{IF}^{cold} is the IF power out with the RF cold load at the receiver input. The procedure for measuring receiver-noise temperature is shown graphically in Figure 3.16. A line is drawn between the hot and cold points in the RF temperature-IF power plane. The intersection of this line with the zero RF-temperature axis is the noise power at the output. The intersection of this line with the zero IF-power axis is the noise temperature of the mixer. Receiver measurements are particularly easy, because the IF amplifiers properties and the measurement bandwidth drop out of the calculation.

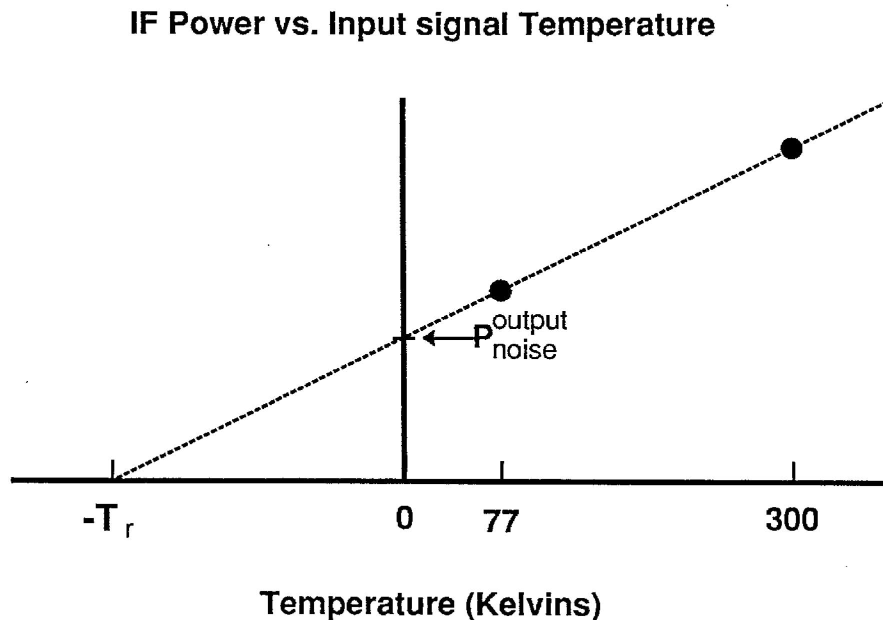

Figure 3.16 Graphical calculation of receiver noise.

The IF chain of the McGrath receiver is designed so that both mixer-noise temperature and mixer-conversion gain can be measured accurately; a similar design was used by McGrath *et al.* (1985 and 1986). The receiver has a calibrated IF noise source, which allows the IF chain to be calibrated. Once the IF chain is calibrated, the power at the mixer's IF output can be determined. The mixer conversion gain is calculated as the ratio of the input RF signal power to the IF power at the mixer's output. The

mixer-noise temperature is calculated in the same way as the receiver-noise temperature except that the IF power is measured at the mixer's IF port, not at the IF amplifier's output. The accurate measurement of mixer properties is important in understanding the results of NbN/MgO/NbN mixer tests.

Inductive Tuning Circuits

Junction capacitance can be tuned out because the NbN leads are superconducting, so there is no series resistance. If junction capacitance is tuned out, the junction RC product will not limit the high-frequency response of a mixer. In practice, as the Q of the tuning structure is increased, the instantaneous bandwidth is reduced so that small RC products are still desirable. This subsection attempts to describe the tuning circuits used in our mixer tests and elsewhere.

The most important tuning structures used are the backshort and E-plane tuner in the mixer block. Scale-model measurements and theoretical calculations have been made on the Ellison mixer block (Büttgenbach *et al.*, 1990). Several predictions are made on the basis of this work. Good coupling for junctions with $\omega RC = 4$ can be achieved if the mixer block is lossless; however, for this large a capacitance, the instantaneous bandwidth is extremely small. This indicates that achieving good coupling would be impossible with a real backshort and E-plane tuner, because physically small changes in the tuner positions will lead to drastic changes in embedding impedance. Additionally, this calculation is based on no loss for the waveguide or the leads across the waveguide. These losses will reduce the capacitance that can actually be tuned out by the mixer block at 205 GHz. For the NbN junctions tested, the capacitance is roughly 85 fF for a 1 μm^2 tunnel junction. The resistance of the junctions tested was between 45 and 80 Ω. This leads to an ωRC product ranging from 5 to 9 at 205 GHz. Clearly, the block cannot perfectly tune out the capacitance of our NbN/MgO/NbN mesa junctions without an additional tuning element.

Tuning circuits can be integrated on the chip with the tunnel junction. These integral tuning circuits can be used in a waveguide receiver to tune out the capacitance at the center frequency. This has two advantages: Mechanically adjusting the backshort is easier because the capacitance is roughly tuned out, and a larger ωRC product can be tuned out, because another pole has been added to the tuning circuit. In open-structure receivers, integrated tuning structures are the only tuning elements available.

Lumped element circuits can be used to model SIS tunnel junctions and tuning structures. Figure 3.17 shows the equivalent lumped element circuit for a tunnel junction and a shunt-inductor tuning circuit. The tunnel junction is modeled as an ideal Josephson element in parallel with a nonlinear tunneling resistor (R_t) and a shunt capacitor (C). A parallel inductor ($L_1 = 1/\omega^2 C$, where ω is the angular frequency of the signal) is used to tune out the shunt capacitor at the signal frequency. The inductor will short out the DC and IF signals, so a blocking capacitor (C_b) is placed in series with the inductor to make the shunt appear as an open circuit at the IF and DC. If the blocking capacitor is much larger than the junction capacitance,

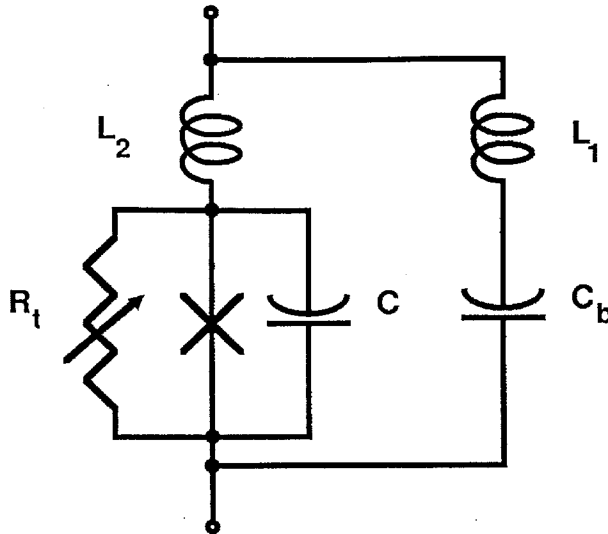

Figure 3.17 Equivalent lumped element circuit for a wire inductor tuning circuit.

it can be treated as a short at the signal frequency.

A shunt inductor can be fabricated as a small loop of wire in parallel with the junction that is capacitively coupled to one of the electrodes. The blocking capacitor can be either a lumped capacitor, or a quarter wavelength section of low-impedance transmission line at the signal frequency (Pan *et al.*, 1989.) Unfortunately, there is usually a parasitic lead inductance (L_2) in series with the junction that limits the use of wire inductors at high frequencies. The maximum angular frequency at which a wire inductor will work is $\omega = 1/\sqrt{L_2C}$. At submillimeter wavelengths, wire inductors are impractical because of this series inductance and difficulties in fabricating the small loops needed.

A second type of tuning element uses an open-ended or shor- circuited section of transmission line. The impedance of an open-ended transmission line is $iZ_0\cot(\beta l)$, where Z_0 is the characteristic impedance of the transmission line, $\beta = 2\pi\nu/\bar{c}$, $\bar{c}$ is the propagation velocity, l is the stub length, ν is the frequency and i is the square root of negative one. If the transmission line length is between a half- and a quarter-wavelength, the impedance seen by the junction is inductive. This type of circuit was used by Räisänen *et al.* (1985). To maximize the bandwidth of the tuning structure, the length is chosen to be 3/8 λ, and the line impedance is chosen to be $Z_0 = 1/\omega C$. A similar structure uses a short ($l < \lambda/4$) section of transmission line terminated with a shorting capacitor. This capacitor can be a lumped capacitor, or a 1/4 wavelength section of low impedance line (D'Addario, 1984; Pan *et al.*, 1989). Tuning stubs have inherently small bandwidths compared to wire inductors, because the stub inductance varies with frequency. The advantage of stubs is that they can be placed right at the junction. This minimizes any series inductance between the junction and the tuning element. Series arrays of tunnel junctions are used to increase the saturation power

of SIS mixers (Tucker and Feldman, 1985). When tuning structures are used on series arrays, a stub or loop inductor should be placed on each junction, so the inductance of the leads between junctions does not affect the tuning circuit (Kerr *et al.*, 1987). Open-circuited stubs have been integrated with NbN/MgO/NbN junctions. These stubs are described in greater detail in the discussion of mixer tests.

Methods of accurately characterizing microstrip line stubs are very important. Because of uncertainties in junction capacitance and microstrip line properties, tuning circuits with center frequencies different from the intended frequency are easily fabricated. The straightforward approach to this problem is to measure the junction's specific-capacitance, NbN magnetic penetration depth and microstrip line inductance using SQUIDs; and to measure the propagation velocity using open-ended microstrip line stubs connected to junctions. The design of the tuning circuit can then be based on these measurements; however, the fractional bandwidth of the tuning structure may be 10% or less, while run-to-run variations may cause errors that are larger than this in microstrip line properties or junction capacitance. RF testing of junctions with integral tuning structures can be difficult if the center frequency is not known exactly. This is especially true of open-structure receivers where no external tuning is possible. Therefore, characterizing already fabricated tuning structures is important.

Two methods of characterizing fabricated tuning structures are available. A novel method for characterizing tuning structures was used by Hu *et al.* (1988). They used a Fourier transform spectrometer to characterize the direct responsivity of a junction with a tuning structure as a function of frequency. The resonance from the tuning structure was clearly evident in their measurement. This method is, unfortunately, somewhat complex and time-consuming.

Another method of verifying stub resonance frequencies is to observe the effect of the stub on the I-V characteristic. Resonant voltage steps occur in the I-V characteristic, which are similar to the LC resonant steps that occur in the SQUID measurements. Because the impedance of the microstrip line stub is periodic with frequency ($Z = iZ_0\cot(2\pi l\nu/\bar{c})$), there are several resonant steps. The steps are at voltages corresponding to frequencies where the stub is inductive and resonates out the junction capacitance. The voltage between higher-order (n>3) steps should be $\Delta\nu = \bar{c}/2l_{stub}$, where l_{stub} is the stub length. The propagation velocity can be calculated using this formula.

We have made measurements of resonant steps in NbN junction I-V characteristics and a number of problems were encountered. Typical stubs were 4.5 μm wide and 80 μm long; these stubs showed structure in the I-V characteristic only for the first two or three resonances. To characterize transmission line velocities accurately, at least the first four steps are necessary, because the spacing of the first several steps is not constant. There are several reasons that more steps are not typically observed. Above half the gap voltage (2.3 to 2.5 mV), the junction is oscillating at a frequency for which the NbN is very lossy.

At 1.8 mV, a Fiske resonance (1964) typically occurred. A Fiske step is a resonance from the junction acting as a resonant cavity. The effect of this on the I-V characteristic typically makes it impossible to see tuning-stub resonances near this voltage. These two factors make it difficult to observe resonant steps above 1.7 mV. Finally, the microstrip line impedance of our stubs (12.5 Ω) is much larger than the impedance of the Josephson oscillations for the higher-order resonances. The output impedance of the Josephson oscillator is roughly $1/\omega C$. This is equal to the stub impedance when the junction is biased on the first step; on the higher-order steps the coupling is increasingly bad. This poor coupling reduces the current height of the higher-order resonant voltage steps.

The sharpest resonances observed were for a 7 μm by 75 μm stub, which had a lower microstrip line impedance (8.0 Ω). The I-V characteristic of the junction with this stub is shown in Figure 3.18. The resonant steps appear at 0.40, 1.00, and 1.56 mV. The first two steps are very clear, while the third is somewhat smeared. The spacing of .56 mV between the second and third steps leads to a propagation velocity of 4.0×10^7 m/s. The calculated value for the propagation velocity based on the measured penetration depth, and thickness is 4.6×10^7 m/s. This difference is well within the measurement errors.

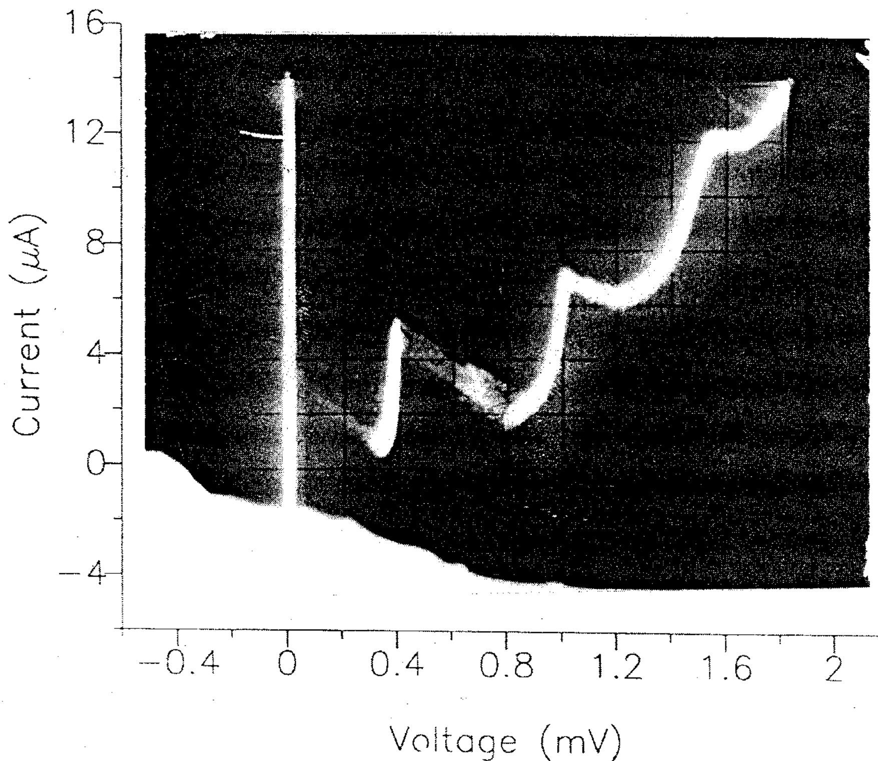

Figure 3.18 I-V characteristic showing stub resonances.

To improve characterization of tuning stubs in the future, low-impedance stubs that are several hundred

microns long will be included on mixer-mask set designs. This will give more resonances in the 0 to 1.5 mV range. Additionally, the lower impedance of the stub will couple more strongly to the Josephson oscillator, making the higher-order steps more pronounced. From these results, the propagation velocity can be calculated more accurately.

RF Measurements at 205 GHz

Mixer measurements of NbN/MgO/NbN tunnel junctions were made with the McGrath receiver. Using the complete IF chain, mixer-noise temperature, coupled mixer conversion gain, available mixer conversion gain and receiver-noise temperature were measured. Typically these quantities were measured for two LO frequencies (201 and 207 GHz) at a physical temperature of 4.2 K. The mixer backshorts were tuned for optimal response to a monochromatic signal in the upper sideband and then the lower sideband. Measurements were repeated with the cold plate of the dewar at 1.5 K. Mixer-noise temperature was almost always lowest, and the conversion gain was always largest when the mixer was biased on the second photon step below the gap voltage (n=2). Most measurements were made on the second photon step below the gap voltage, although mixer measurements were made on the first photon, and one mixer measurement was made on the third photon step below the gap. When the junction was biased on the third photon step below the gap, a magnetic field was necessary to suppress the Josephson effect. The field was large enough that it degraded mixer response. Unless otherwise noted, all mixer numbers quoted are for the second photon step below the gap voltage, and all conversion gains quoted are for coupled conversion gain, not for available conversion gain.

The results of our mixer tests are now given; all of these tests are summarized in Appendix E. Mixer tests can be broken into the three batches of junctions tested. The first set of junctions had no tuning stubs. The IF chain was not calibrated when these junctions were tested, so only the receiver-noise temperature was measured. These tests gave discouraging results with receiver temperatures ranging from 1500 to 2000 K. Subsequent scale-model measurements of the mixer indicated that the mixer block could not tune out the junction capacitance (Büttgenbach *et al.*, 1990).

For the next set of tests, open-ended microstrip line tuning stubs, were designed to tune out junction capacitance. Stub lengths and widths were designed, given the published value of magnetic penetration depth (280 nm, Shoji *et al.*, 1987). The microstrip line was designed for a bottom NbN electrode which was 300 nm thick, a top electrode which was 400 nm thick, and an SiO dielectric layer which was 150 nm thick. Masks were made, and junctions were fabricated for this design. Unfortunately, the penetration depth of our NbN films was measured to be 380 nm. Despite the error in the stub design, tests of these junctions were made with the calibrated IF chain.

Mixer tests of the second batch of junctions gave slightly better results than the first batch. The

control junction with no stub in this set, number 1.1, had a mixer-noise temperature of 767 K and a conversion gain of -20 dB. Junctions with stubs of width 4.5 μm and lengths 111, 104, and 90 μm were tested. The junction with the longest stub, number 1.3, had a significantly worse mixer-noise temperature than the untuned junction (1080 K). The junction with the 104 μm stub, number 1.2, had a slightly better mixer-noise temperature than the untuned junction (596 K). The junction with the shortest stub, number 1.4, had the lowest mixer-noise temperature of this batch (394 to 633 K across the RF band).

Using the experimental value for the penetration depth, the admittances of these stubs were calculated. The two longest stubs were longer than half a guide wavelength at 205 GHz and were capacitive. The shortest stub tuned out roughly 20 fF of the junction capacitance. The first attempt at using tuning stubs missed the design frequency, because of the error in the assumed magnetic penetration depth. The electrical properties of NbN microstrip line are particularly sensitive to the penetration depth, because the dielectric thickness, penetration depth and NbN thickness are all roughly equal.

To bring the stub resonance into the RF test band, shorter stubs had to be fabricated. The stub length is defined in the final wiring layer etch. To avoid the cost and time of having a new, third mask layer made, a novel method of altering the existing mask was devised; it is described in Appendix F. This method may prove very useful for future tuning-stub designs, because stub lengths can be easily adjusted after the mask set has been made.

A final set of junctions with stub lengths of 75 to 86 μm was fabricated and tested. Five junctions were tested from this batch. Junction number 2.4 was the control junction from this batch; it had no tuning stub. Three junctions with 4.5 μm wide stubs were tested: junction number 2.1 was 75 μm long and tuned out 95 fF at 205 GHz, junction number 2.3 was 80 μm long and tuned out 70 fF at 205 GHz, and junction number 2.5 was 86 μm long and tuned out 50 fF at 205 GHz. Junction number 2.2 had a 7 μm wide 75 μm long stub; this junction tuned 150 fF at 205 GHz. The stubs for this set of junctions tuned out a range of capacitance around the expected capacitance of 85 fF.

The lowest mixer-noise temperature for this batch was obtained with junction number 2.1. The current-voltage characteristic for this junction with and without LO applied is shown in Figure 3.19. Because of the rounding in the I-V characteristic, the photon steps are barely visible. The mixer-noise temperature of this junction at 206.4 GHz for a physical temperature of 1.5 K was 133 K, and the conversion gain was -11.9 dB. Figure 3.20 shows the mixer-noise temperature and conversion gain at four signal frequencies for this junction. The crosses represent data taken at 1.5 K, and the open circles represent data taken at 4.2 K. The mixer-noise temperature dropped by roughly 95 K when the mixer block was cooled from 4.2 K to 1.5 K. This drop in noise temperature upon cooling to 1.5 K was the largest measured. Along with this drop in noise temperature, there was an improvement in conversion gain of 2 to 3 dB. The temperature

dependence of the mixer properties is discussed at the end of this section. As is seen in Figure 3.20, the response for junction number 2.1 was better at higher frequencies. The capacitance tuned by the stub is zero when the stub is half a wavelength long and infinite when the stub is a quarter of a wavelength long. In the case of this junction, the stub was too short at the lower frequencies.

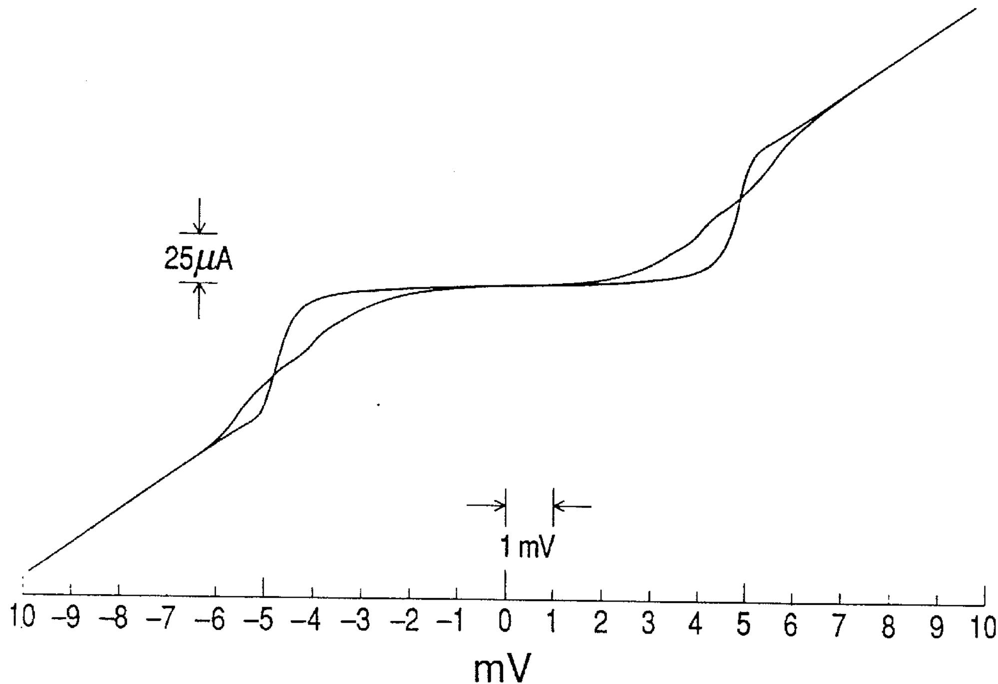

Figure 3.19 Mixer I-V characteristic with and without LO power applied.

Junction number 2.3 has a stub that is 5 μm longer than junction number 2.1; the longer stub tunes out less capacitance (70 fF versus 95 fF at 205 GHz). This junction had a mixer-noise temperature at 1.5 K, which was nearly identical to junction 2.1 (134 K) The noise temperature of this junction at 4.2 K was the lowest value measured (185 K). Figure 3.21 shows the IF power for junction number 2.3 with a hot and cold black body at the input of the mixer. Peaks in the IF power corresponding to the n=2, 1, -1 and -2 photon steps are identified in the figure. The ratio of the hot and cold IF power is the "Y factor," which is used to calculate the receiver noise (Equation 3.9). In this figure, the Y factor is almost 2 dB on the second photon step below the gap voltage.

Two more junctions with stubs were tested from this batch to bracket the optimum response as a function of capacitance tuned by the stub. The stub of junction number 2.2 was the same length as the stub of junction number 2.1, but it was 50% wider, so it tuned out 50% more capacitance. At the lowest frequency tested (199.5 GHz), this stub tuned out 174 fF, which is much larger than the junction capacitance. The mixer-noise temperature at this frequency was 358 K and 300 K at a physical temperature of 4.2 K and 1.5 K, respectively. At the highest frequency tested (208.5 GHz), this stub tuned out 135 fF,

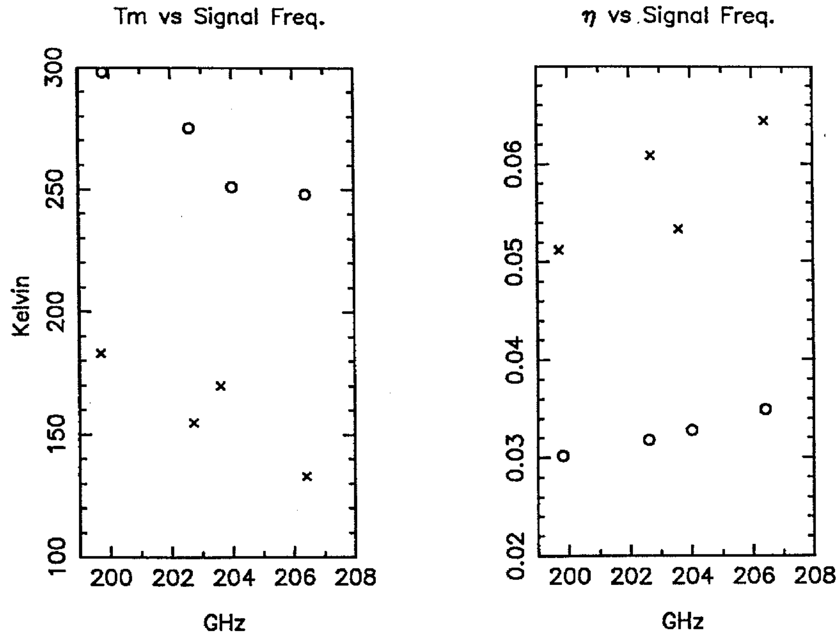

Figure 3.20 Mixer-noise temperature and conversion gain versus signal frequency. Shown are the results for junction number 2.1 across the RF band. The open circles are at 4.2 K, and the Xs are at 1.5 K.

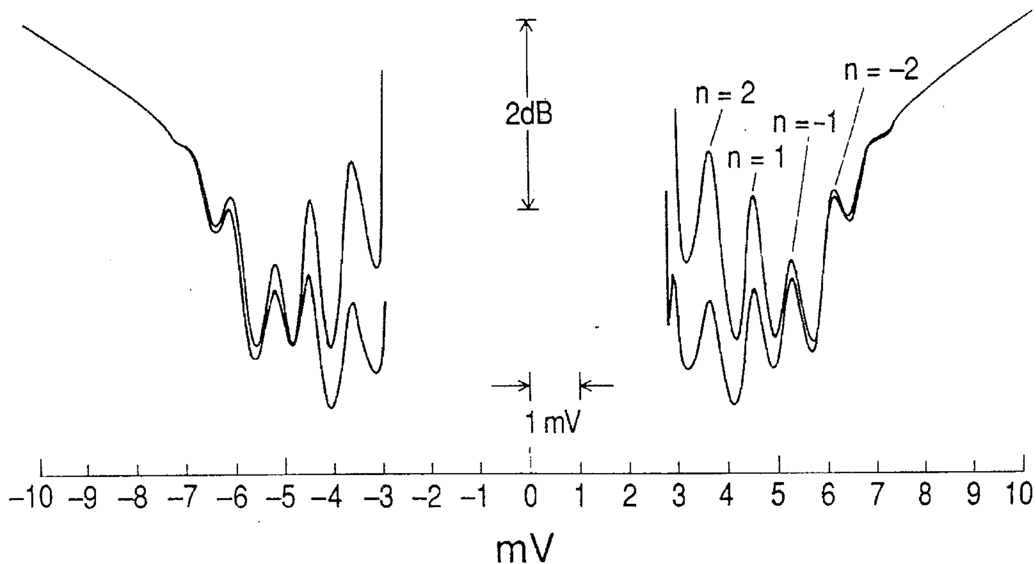

Figure 3.21 IF power out versus voltage with a hot and cold load at the mixer input. The IF power peaks at voltages corresponding to the n=2, 1, -1, and -2 photon steps are labeled.

which is closer to the actual junction capacitance. The mixer-noise temperature at this frequency was 244 K and 164 K at a physical temperature of 4.2 K and 1.5 K, respectively. The noise temperatures at

208.5 GHz were good, while the noise temperatures at 199.5 GHz were mediocre. The mixer response of a junction across even a small signal band is a good indication of whether the stub is undertuning or overtuning the junction capacitance. Junction number 2.5 bracketed the low end of capacitance tuned. The response of this junction was best at the lowest frequency tested.

To get an overall view of how mixer performance varies with the capacitance tuned by the stub, mixer noise-temperature and conversion gain are plotted as a function of the capacitance tuned by the stub for each junction at the frequencies tested; these data are shown in figure 3.22. The mixer-noise temperature is a minimum near 85 fF of capacitance tuned. This minimum agrees with SQUID measurements of the junction capacitance. The range of capacitance tuned that gives good mixer performance is fairly large, because the mixer block can tune to a range of junction impedances. The conversion gain of the mixer correlates less strongly to the capacitance tuned than the mixer-noise temperature. The scatter in this data is not caused by measurement error, because the conversion gain is measured to better than 10%.

The sideband ratio was measured for several junctions using a broad-band times 12 harmonic multiplier as a signal source. The output of the multiplier was continuously tunable over the mixer band. The power of the output signal was measured to within 2 dB. The IF signal was monitored on a conventional spectrum analyzer. The signal frequency was switched back and forth between the upper and lower sideband with the signal power held fixed. For all of the measurements made except one, the sideband ratio was less than 2 dB. The sideband ratio of junction number 2.1 was 4.5 dB at one frequency; however other measurements on this same junction at different frequencies yielded sideband ratios of 1.2, 0.6 and 0.3 dB. With the one exception, the response of NbN/MgO/NbN junctions was double sideband.

Mixer-noise temperature and conversion gain both improve when the mixer is cooled from 4.2 K to 1.5 K. We have attempted to understand this improvement. A number of possible causes have been ruled out, and the evidence indicates a temperature-dependent loss mechanism in the NbN, although no definite conclusions have been reached. This phenomenon may be particularly important to operating mixers near 10 K.

The improvement in mixer performance varied somewhat between junctions. Three junctions with tuning stubs gave fairly good mixer performance (numbers 2.1, 2.2 and 2.3). The mixer noise in these junctions improved by 41%, 25% and 25%, respectively. The correlation of mixer-noise temperature and conversion-gain improvement was good, although conversion gain typically improved by 5% more than the mixer-noise temperature. The mixer-noise temperature of the two untuned junctions tested improved by 19% and 7%. The smaller improvement of the untuned junctions indicates that the tuning stub's properties may be temperature-dependent.

Two factors affect the mixer performance: the junction's I-V characteristic and the embedding

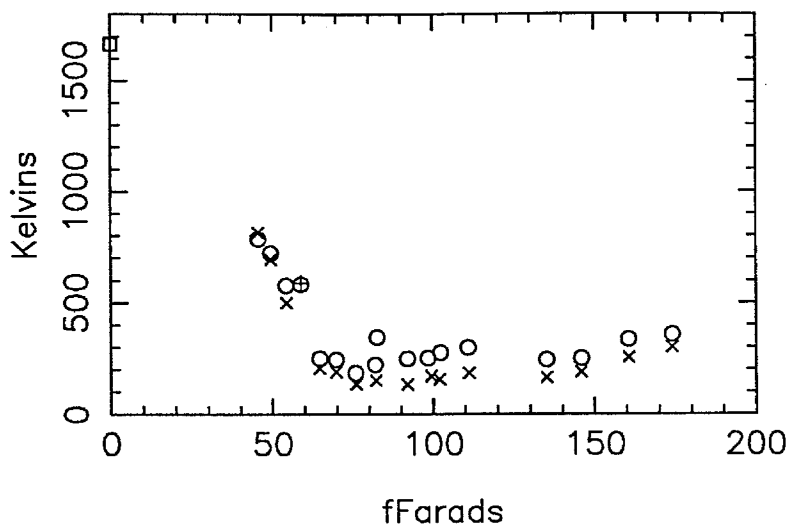

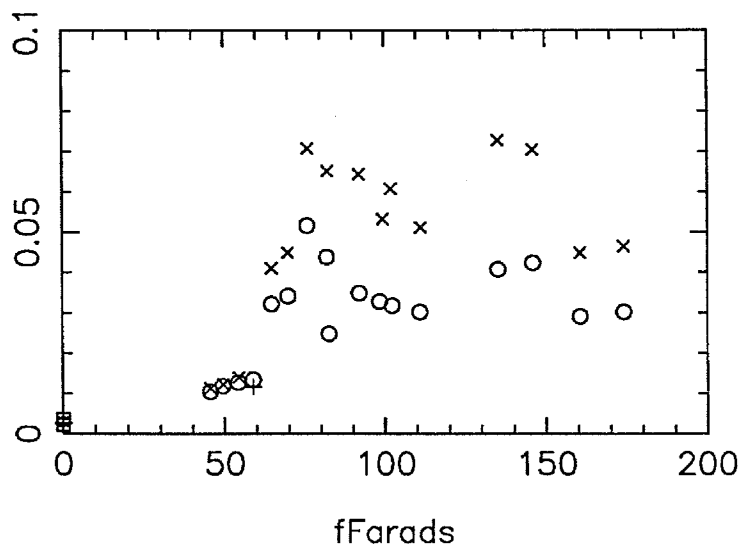

Figure 3.22 Mixer performance as a function of capacitance tuned by the stub. Figure (a) shows the mixer-noise temperature, and Figure (b) shows the coupled conversion gain as a function of capacitance tuned by the stub. Data taken at 4.2 K are shown as circles for n=2, and squares for n=1. Data taken at 1.5 k are shown as Xs for n=2, and plusses for n=1.

impedance at various frequencies. Because the temperature is well below half the transition temperature of NbN, the I-V characteristic of an NbN junction should not change significantly between 4.2 and 1.5 K. Figure 3.23 shows the I-V characteristic of junction number 2.1 at both temperatures. The sharpness of the I-V characteristic is virtually unchanged, the sum gap changes by less than 50 μV, and the subgap

conductance changes by 10% to 15% at typical bias voltages. Tucker's theory (1979) predicts that shot noise is the primary source of noise in SIS mixers. If this were the case, the mixer noise should decrease by 10% to 15% upon cooling from 4.2 to 1.5 K. This can explain the improvement in the junctions without tuning stubs, but cannot explain the 41% to 25% improvement in the junctions with tuning stubs.

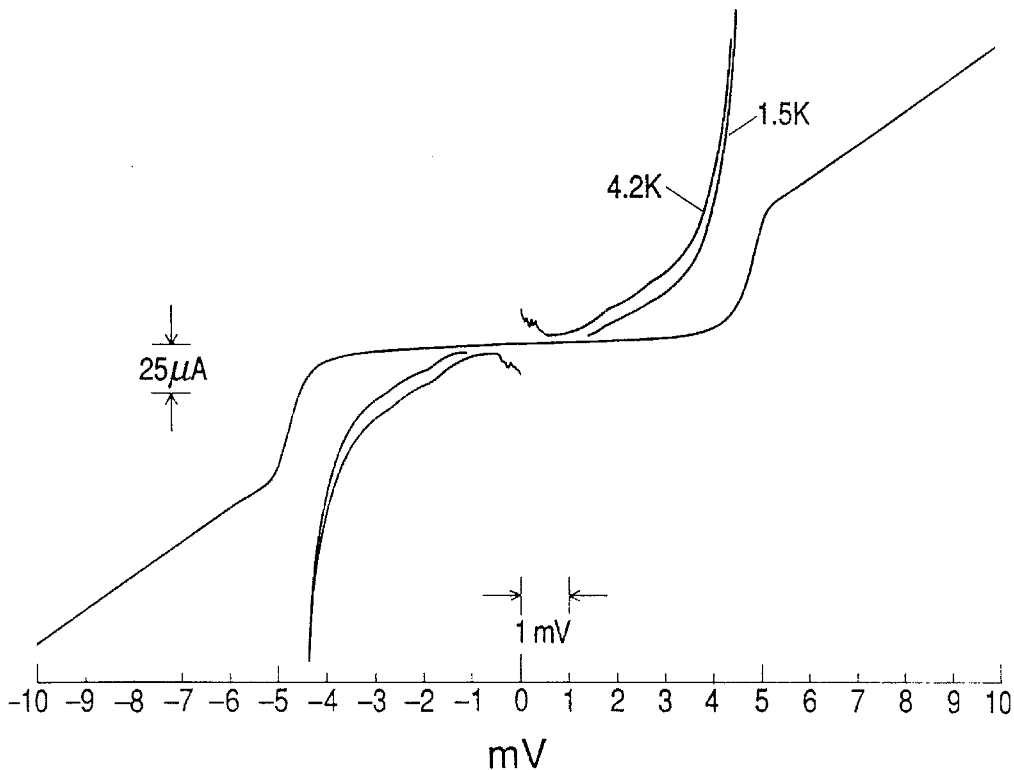

Figure 3.23 Mixer I-V characteristic at two temperatures. Shown is tunnel junction number 2.1 at 4.2 K and 1.5 K.

The embedding impedance can also affect mixer performance significantly. The larger improvement in the mixer properties of junctions with tuning stubs than without tuning stubs upon cooling to 1.5 K indicates that the tuning stub's properties (propagation velocity, impedance, or loss) are changing with temperature. Two possible materials properties could affect the propagation velocity and impedance: the dielectric constant in the SiO and the magnetic penetration depth of the NbN. The dielectric constant of SiO has not been measured at these temperatures, but there is no evidence that it is changing at these low temperatures. The magnetic penetration depth of NbN was measured as a function of temperature by Shoji *et al.* (1987), and it does not change significantly below 7 K.

The loss in the microstrip line may also be a function of temperature. The SiO is a possible source of loss in the microstrip line stub, but measurements of loss in Nb-SiO-Nb microstrip line at 100 GHz by Smith *et al.* (1990) determined the loss to be less than 10 dB/m. Unless the loss at 200 GHz is dramatically

larger than at 100 GHz, the SiO does not cause enough loss to explain the improved mixer performance at 1.5 K. Therefore, we believe the NbN has a temperature-dependent loss mechanism.

Loss in NbN Microstrip Lines

The loss in NbN microstrip lines was analyzed in two ways. A theoretical model was used to predict the loss in NbN microstrip lines, and the absorptivity of NbN was measured as a function of frequency using a Fourier transform spectrometer (FTS). Both of these methods are described, although neither provides any direct evidence that explains the improved mixer performance at 1.5 K.

Superconducting transmission lines have finite losses at 200 GHz caused by the finite inductance of the superconducting pairs. With the assistance of Jonas Zmuidzinas (1990), we have attempted to estimate the loss in our microstrip lines analytically. The Mattis-Bardeen expression is used for the impedance of NbN and the propagation velocity in the NbN. The Mattis-Bardeen formulation is a microscopic theory valid in the "dirty" limit; the dirty limit is appropriate for NbN. Microstrip line properties are analyzed using the method of Kautz (1978) and Whitaker *et al.* (1988). The magnetic fields in the NbN microstrip line are not completely confined, because the NbN layers are comparable to the magnetic penetration depth. There will be some radiation losses in the microstrip line from these stray fields. This calculation accounts for the radiative losses at the superconductor air interface, by calculating the reflection coefficient at this interface for an incident wave.

Results from this loss calculation are now given. The following parameters are assumed for the microstrip line unless otherwise specified: dielectric thickness–150 nm, relative dielectric constant–5.5, dielectric loss tangent–0.0, NbN thickness (ground plane and wiring layer)–330 nm, microstrip line width–4.5 μm, NbN sum gap–4.8 mV, NbN T_c–15 K, NbN resistivity at 20 K–130 $\mu\Omega$ cm, temperature–4.2 K and frequency–205 GHz. For the default parameters, the loss is 0.03 dB per microstrip line wavelength. If this is the only loss, then the Q of the tuning stub is 145. The calculation of the loss was repeated for a temperature of 1.5 K. At the lower temperature the loss is 0.01 dB per wavelength. The relative difference in microstrip line loss at 4.2 and 1.5 K is large, but the absolute loss is small in both cases. This calculation cannot account for the 25% to 41% improvement in mixer noise temperature upon cooling to 1.5 K.

The variation of microstrip line losses with other parameters is also important and can be calculated. The loss for thicker films (600 nm) is roughly half that of the 330 nm films. The loss for thinner films (150 nm) is 2.6 times worse than the 330 nm films. Thicker NbN layers should be used to reduce loss in NbN microstrip line. The loss of films at 8 K is 0.5 dB per wavelength. This is much larger than the loss at 4.2 K. Even if the NbN layers are 1.0 μm thick, the loss is still 0.3 dB per wavelength at 8 K. This has important ramifications for high-temperature operation of NbN devices. The loss per wavelength was calculated as a function of frequency for 600 nm-thick NbN films; the results are given in Table 3.2.

The loss is less than 0.04 dB per wavelength up to 1100 GHz. The theoretical model indicates that tuning stubs should work well up to the gap frequency, if the NbN electrodes are thick enough.

Table 3.2 NbN microstrip line loss as a function of frequency

Frequency (GHz)	Loss per Wavelength (dB)	Loss per Wavelength (%)
100	0.013	0.29
200	0.014	0.32
300	0.015	0.34
400	0.015	0.35
500	0.016	0.37
600	0.018	0.40
700	0.020	0.45
800	0.022	0.51
900	0.026	0.59
1000	0.031	0.71
1100	0.039	0.90
1200	0.97	20.0
1300	3.6	56.5

The absorptivity of a NbN film was measured as a function of frequency by Miller and Richards (1990). The absorptivity is a direct measurement of loss in the film. The data given here are still preliminary. The Miller apparatus is shown in Figure 3.24. The measurement is made by attaching a bolometer to a thin quartz sample with NbN on one side. The temperature rise in the sample is a measure of the absorption of radiation by the NbN film. The NbN sample is in a dewar with a brass reference sample. The absorptivity of the brass is constant over the frequencies measured, because the mean-free path of the conduction electrons in the brass is very short, so the electron scattering is defect-limited, not phonon-limited. The two samples look out into a Fourier transform spectrometer. The difference signal between the bolometers attached to the NbN and brass samples is measured as a function of the FTS mirror position. The Fourier transformation of this function gives the absorptivity versus frequency. The temperature dependence of the absorptivity cannot be measured, because the bolometer must be at 1.5 K to get adequate signal to noise.

The absorptivity of NbN as a function of frequency is shown in Figure 3.25 The absorptivity has a broad peak near 150 GHz, a sharp peak at 750 GHz and a large value above 1100 GHz. The rise above 1100 GHz is expected, because this corresponds to the gap frequency ($2\Delta_{NbN}/h$). Above this frequency, photons can break Cooper pairs, and the resistivity of the film should approach that of the normal state. The peak at 750 GHz is probably due to a Fabry-Perot resonance in the sample that is 4-mil fused quartz with a gold film on one side and NbN on the other. Because the NbN is less than a penetration depth

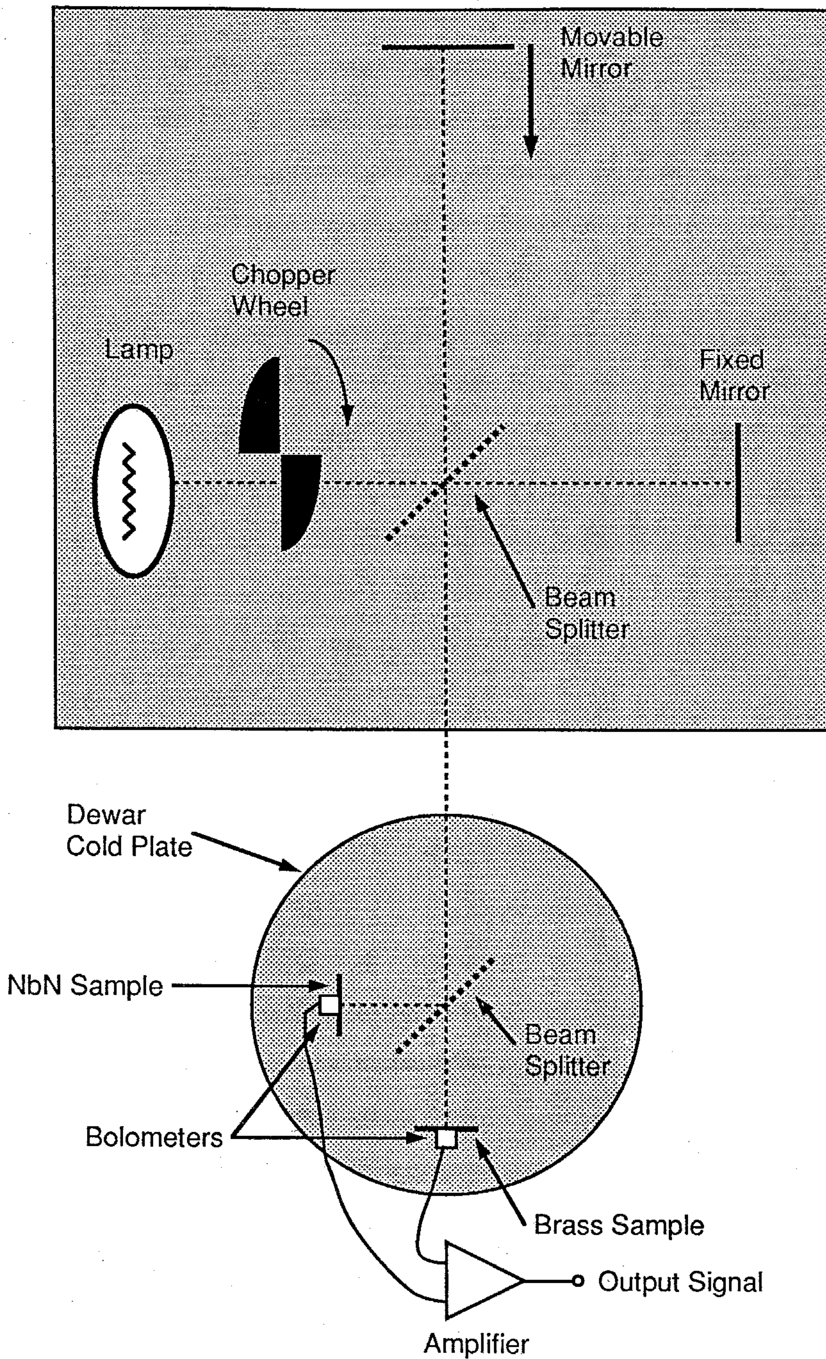

Figure 3.24 Diagram of RF loss measurement apparatus.

thick (d_{NbN} = 300 nm), it is partially transparent, and the quartz acts like a half wavelength Fabry-Perot cavity. This peak may also correspond to loss from Nb in the films at $2\Delta_{Nb}/h$. These possibilities will be investigated further by measuring thicker NbN films.

The broad peak at 150 GHz is important to mixer tests at 205 GHz. There are two possible ex-

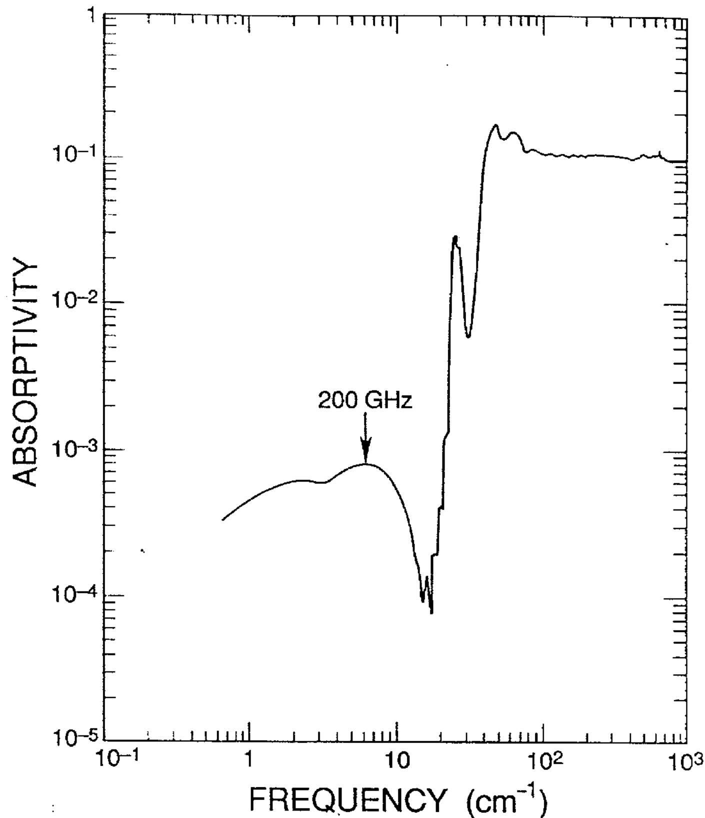

Figure 3.25 Absorptivity of NbN as a function of frequency.

planations for this low-frequency peak in absorptivity. Radiation may be passing through the NbN and being absorbed in the fused quartz. This seems unlikely to account for the magnitude of the loss or the frequency dependence. Nonsuperconducting material between NbN grain boundaries may be causing this low-frequency loss. The coupling between NbN grains can be modeled as a Josephson weak link with a shunt capacitor. As the frequency is increased, more current will pass through the capacitor, which is a lossless element. Because there are many different capacitor values for the individual grains, this roll-off will be slower than 3 dB per octave of frequency, which is normal for an RC filter. This explanation describes the shape of the peak at 150 GHz well. To test this hypothesis, higher-quality films, possibly with residual resistivity ratios less than one, should be tested and compared to the original film.

There are several experiments that need to be done to address more carefully the problem of loss in NbN microstrip lines. The key question to be addressed is whether the loss stems from the NbN itself, or the degree to which the electromagnetic fields are confined by the NbN. FTS measurements of thicker and higher quality NbN films should be made and compared to previous results. This will determine if the absorptivity is dependent on thickness or film quality. Additionally, microstrip line stubs, which completely

confine the magnetic field, should be fabricated and tested with mixers.

Summary

This section has described the results of the first mixer tests with NbN/MgO/NbN tunnel junctions. The results of these tests were encouraging. The mixer-noise temperature at 4.2 K is between 185 and 250 K; this is 2 to 3 times higher than lead-alloy junctions in this same mixer block. The performance of the NbN junctions is worse than the lead junctions for two primary reasons: The capacitance of the NbN junctions is larger, and the I-V characteristics of the NbN junctions are more rounded than lead junctions. The capacitance of the NbN junctions is partially tuned out by integral microstrip line tuning stubs. Understanding these tuning circuits is critical if submicron NbN junctions are to be used at frequencies approaching 1100 GHz. The mixer-noise temperature decreases to 133 to 200 K when the mixer is cooled to 1.5 K. This improvement cannot be explained by changes in the I-V characteristic alone. One possible cause for this improvement is a temperature-dependent loss mechanism in the NbN-SiO-NbN microstrip line stub. A preliminary investigation of possible loss mechanisms was made.

E. Junction Uniformity

A focal plane array is a one- or two-dimensional array of antennas and mixers, which is placed at the focal plane of a telescope. Each element in the focal plane array will image a different point on the sky. Focal plane arrays will allow much faster mapping of extended sources. For this application, many nearly identical junctions would have to be fabricated on a single wafer; therefore, the uniformity of NbN/MgO/NbN junctions across a wafer must be measured.

Most junction properties are uniform to within over a two-inch diameter wafer. Typically, junction sum gaps and subgap leakage are vary by less than 5% over a wafer. As a example, the sum gap of NbN junctions typically varies by a tenth of a millivolt over a two-inch wafer. This variation is caused by the size of the magnetron sputter guns (two inches in diameter). Small variations like this are not a problem for focal plane array fabrication. The junction resistance varies across a wafer or chip more than other properties. Each junction in a focal plane array must have the same impedance as the antenna to which it is coupled. This section describes measurements of resistance uniformity and possible causes of nonuniformity in junction resistance.

The easiest parameter to measure for large numbers of junctions is the junction critical current. Fortunately, the product of a junction's critical current and its normal resistance is roughly constant. For a BCS superconductor at 0 K, $I_cR_n = \pi\Delta_\Sigma/4e$. If NbN were an ideal BCS superconductor, I_cR_n would be 3.5 to 4.1 mV for gap values of 4.5 to 5.2 mV. Strong coupling superconductors like NbN typically have their critical currents reduced from the BCS value. A typical NbN junction has an I_cR_n value of 2.8 to 3.1 mV, depending on the sum gap of the junction.

Junction critical current uniformity is usually measured by fabricating series arrays of tunnel junctions. The I-V characteristic of 10 junctions in series is shown in Figure 3.26. As the current level is raised, the junction with the lowest Josephson critical current switches out of the zero-voltage state; as the current level is raised further, each junction in order of increasing critical current switches out of the zero-voltage state. The line of critical currents is easily seen at 170 μA. By reading each value off, statistics on critical current uniformity can be determined. In this figure, the critical currents are between 165 and 175 μA.

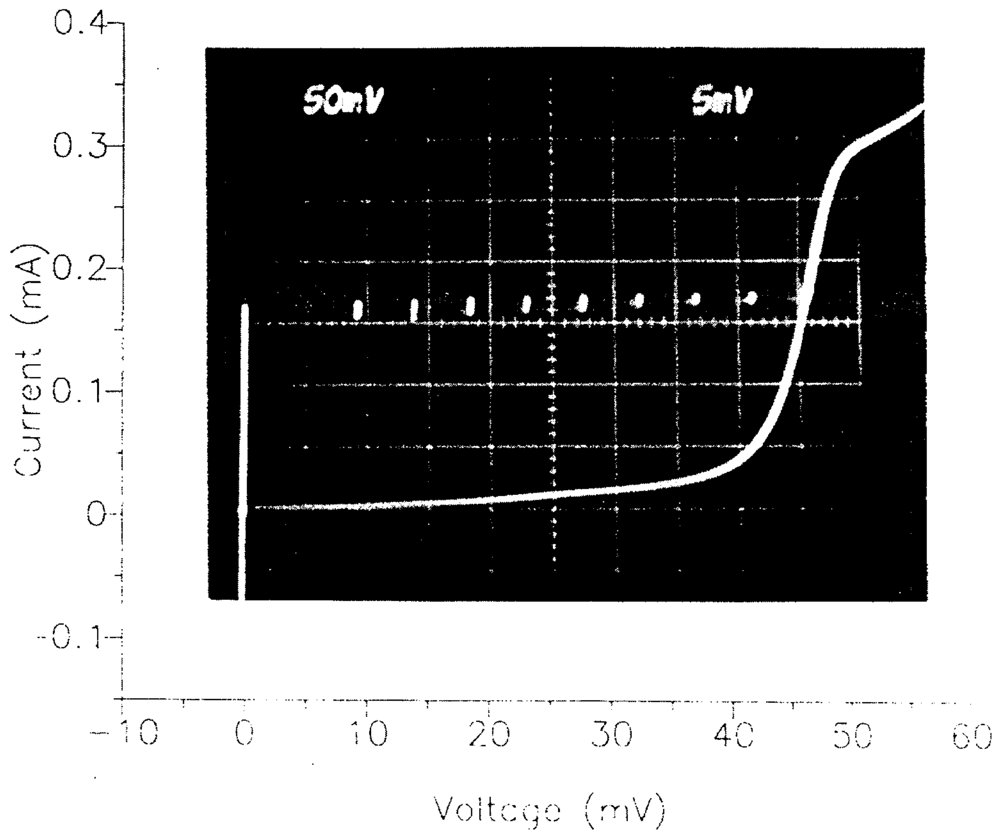

Figure 3.26 Series array I-V characteristic for 10 junctions.

The chips used to measure critical current uniformity consisted of 304 junctions connected in series. There are leads coming off the series array at various points, so blocks of 1, 10, 20, and 100 junctions can be measured separately. Arrays of both 2 x 2 and 4 x 4μm^2 junctions were fabricated. Figure 3.27(a) shows an I-V characteristic for an array of 100 4 x 4μm^2 junctions, the minimum-to-maximum spread of critical currents for this array is 11%. The typical spread in critical currents for these arrays is 15%, and the typical standard deviation for these arrays is $\pm$3%. Figure 3.28 shows a histogram of critical currents for a typical array of 104 4 x 4 μm^2 junctions. Uniformity of 2 μm junctions is much worse than 4 μm junction. Figure 3.27(b) shows an I-V characteristic for an array of 100 2 x 2μm^2 junctions. The uniformity of 2 μm junctions is reduced, because defining reproducible 2 μm features using photolithography is difficult.

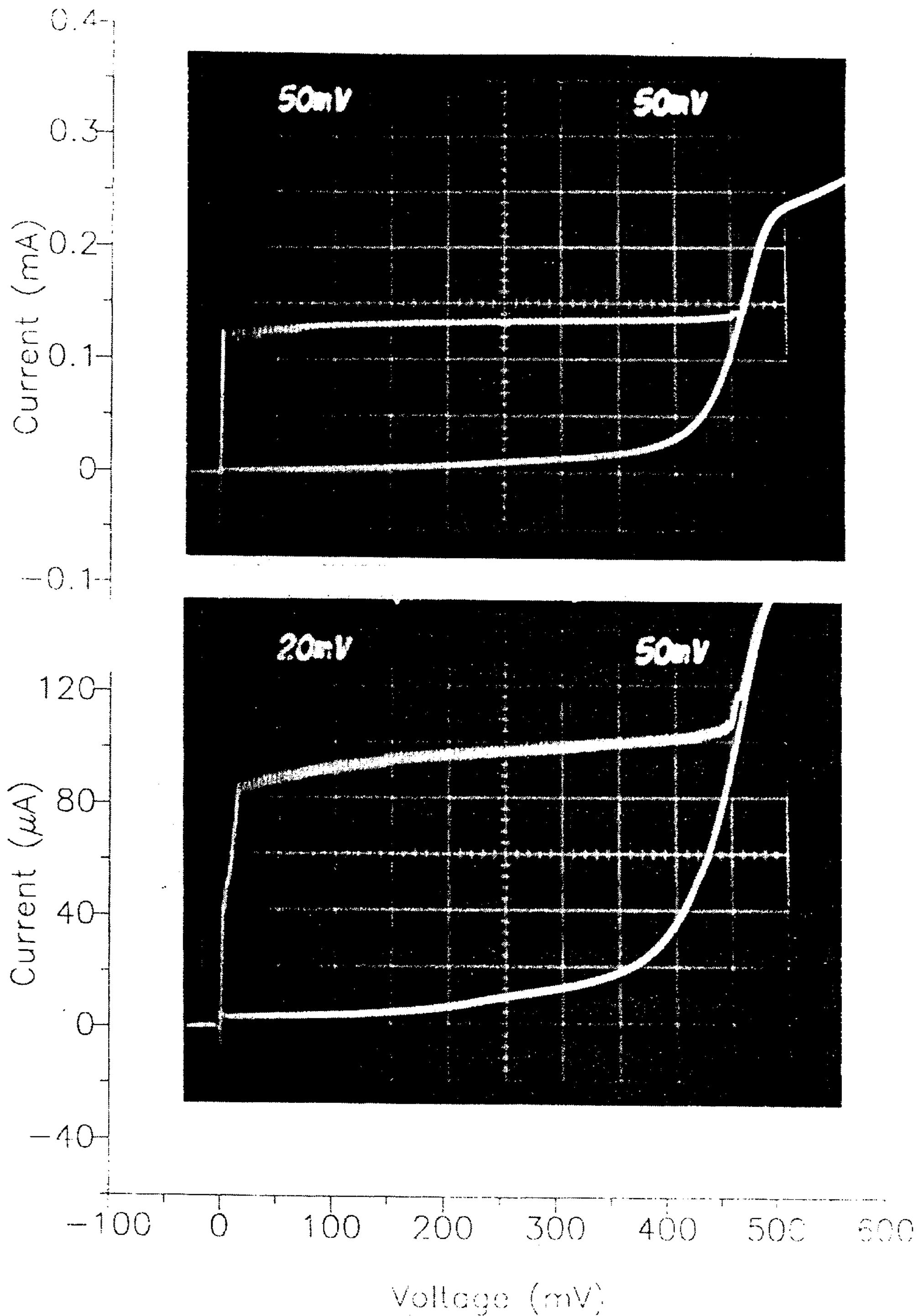

Figure 3.27 Series array I-V characteristics for 100 junctions. Figure (a) shows an I-V characteristic for an array of 100 4 × 4 μm^2 junctions. Figure (b) shows an I-V characteristic for an array of 2 × 2 μm^2 junctions.

Focal plane arrays will require reasonably uniform junctions over a wafer. Tests on single junctions as nearmillimeter wavelength mixers typically show good results with resistances ranging from 50 to 100 Ω.

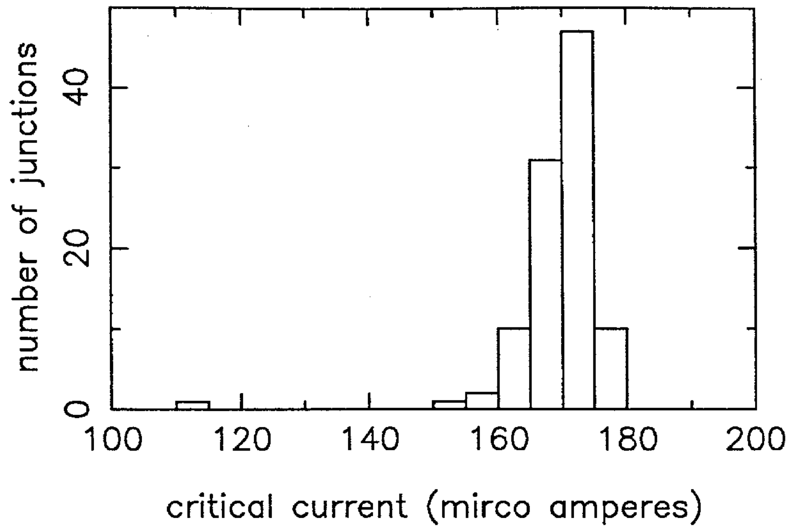

Figure 3.28 Histogram of critical currents. This histogram shows the distribution of critical currents for an array of 104 4 × 4 μm^2 tunnel junctions over a 0.25" chip.

The critical currents for series arrays of 4 × 4 μm^2 tunnel junctions are uniform to less than 15%. This implies that the trilayers are uniform over the chip area, so lithography and processing will limit the uniformity of micron and submicron junctions. Junction areas defined using electron-beam lithography can be easily controlled to within 50 nm; however, other processes, such as RIE, may limit junction uniformity. Finally, no series arrays of NbN edge junctions have been fabricated, but the uniformity of 9 edge junctions on a single chip is less than 30% (Hunt, 1989). The present data suggest that NbN junctions should have sufficient uniformity for focal plane arrays, but submicron junctions need to be fabricated before final conclusions can be drawn.

F. Chapter Summary

This chapter has described a number of measurements made to characterize NbN/MgO/NbN tunnel junctions and NbN films; in this final section these results and their effect on SIS mixers will be summarized. Areas for possible improvement in device or material quality will be discussed.

The R vs. T plot is the simplest measure of a superconductor's quality. High-transition temperature (15.5 K) NbN can be deposited on unheated substrates; however, it is much easier to deposit high transition temperature NbN on heated substrates (250 to 500° C). Measurements of the film critical current, room-temperature resistivity and residual resistivity ratios for heated and unheated films suggest that as the substrate temperature is increased the NbN crystal size increases. The increase in crystallite size decreases the effect that nonsuperconducting material in the grain boundary regions has on the films. This

nonsuperconducting material is thought to cause gap-smearing in NbN tunnel junctions.

The magnetic penetration depth is another important material property of NbN. Using SQUIDs, the magnetic penetration depth for NbN deposited on unheated substrates (400° C) was measured to be 380 nm; while films deposited on heated substrates had penetration depths of 280 nm. The penetration depth of 280 nm on heated substrates agrees well with other published values. One question that should be addressed is how much the penetration depth varies from run-to-run under similar deposition conditions? Variations of the penetration depth will affect the reproducibility of NbN microstrip circuits like tuning stubs. The large penetration depth of NbN makes most transmission lines slow wave structures. Slow wave structures can be used to fabricate compact delay lines or tuning stubs; however, the penetration depth and film thickness need to be known accurately to design transmission lines of known impedance and electrical length.

Most data on NbN/MgO/NbN tunnel junction are obtained from the I-V characteristic. The biggest advantage NbN junction have over other materials is the large gap voltage. Gap voltages are typically 5.0 mV, although junctions with gap voltages as high 5.6 mV have been fabricated. The large gap voltages of NbN/MgO/NbN junctions will make them useful as mixers well into the submillimeter band if the RC product can be decreased or the capacitance tuned out.

I-V characteristics of NbN/MgO/NbN junctions are typically much more rounded than Pb or Nb tunnel junctions. NbN junctions have rounded I-V characteristics for several reasons. The short electronic coherence length of NbN makes gap-smearing a problem. Gap-smearing can be reduced if better quality NbN can be deposited. The ratio of the subgap to normal resistance in NbN tunnel junctions is small (10) as compared to high-quality niobium or lead junctions. There are three possible sources of subgap conduction in NbN junctions. Parallel conduction through weak-link Josephson junctions occurs at pinholes in the barrier. This form of leakage is occasionally observed, but is not the major cause of leakage. The subgap leakage is characterized by a rise in the leakage current at half the sum-gap voltage. This could be caused by either multiparticle tunneling, or SIN tunneling. If subgap conduction is caused by SIN tunneling, it could be reduced by depositing higher-quality superconducting electrodes. If subgap conduction is caused by multiparticle tunneling, then it is inherent to the barrier material. The sharpness of NbN/MgO/NbN I-V characteristics can be improved by improving NbN film quality, but the I-V characteristic of NbN junctions will never be as sharp as Pb or Nb junctions, because of the short coherence length of NbN. The difference in I-V sharpness will have a more significant effect on mixer performance at lower frequencies.

The specific capacitance of NbN/MgO/NbN junctions was measured as a function of the normal-resistance, area product. This function needs to be known to calculate the RC product of the junctions. The specific capacitance of NbN/MgO/NbN junctions is roughly twice that of comparable lead-alloy and

Nb junctions. In submillimeter wavelength mixers, the junction capacitance must be tuned out at the signal frequency.

NbN mixers have been tested at 205 GHz. Successful testing of NbN junctions was possible only after microstrip line stubs were designed to tune out the junction capacitance. Proper design of these stubs relied on accurate characterization of NbN penetration depth. These tests showed reasonable performance over the frequency range tested. Typical noise temperatures of NbN junctions were a factor of two to three worse than Pb junctions in the same mixer block. The difference in noise temperature is attributed primarily to I-V characteristic sharpness, although loss in the tuning stubs may also have degraded mixer performance. This loss is currently under investigation. Future mixer tests will focus on using submicron junctions at higher frequencies. The 205 GHz tests will help in correctly designing high-frequency mixers.

Chapter IV. Conclusions and Future Work

This chapter makes some conclusions on the future of NbN junctions: their limitations, and their advantages. NbN junctions were developed because of their relatively large gap voltages. The energy gap allows the NbN films to have low RF losses up to 1200 GHz, and it reduces the effect of Josephson phenomena, such as the drop-back voltage. However, the RC product of NbN junctions will limit high-frequency performance of these devices. The ultimate high-frequency limit of NbN junctions will depend on the maximum quality factor (Q) of the tuning structure used to resonate out the junction capacitance. At the highest frequencies submicron, low R_nA product junctions are required.

This thesis began with a description of why NbN and MgO were chosen as the superconductor and barrier material. To conclude this thesis, other barrier materials and other superconductors that may prove useful in the future are discussed. Different barrier materials can improve the RC product of NbN junctions, and new superconductors can have larger energy gaps and transition temperatures. Both of these possibilities are discussed.

Finally, the possibility of operating NbN-based mixers on closed-cycle refrigerators is analyzed. Refrigerators are desirable in locations where liquid helium is not practical as a coolant.

A. RF Limitations of NbN/MgO/NbN Junctions

The most important limitation for NbN/MgO/NbN junctions as mixers at submillimeter wavelengths is the RC product of the junction. The RC product decreases with decreasing barrier thickness. The minimum barrier thickness is one monolayer. Shoji *et al.* (1987) have fabricated junctions with 0.5 nm-thick MgO barriers, roughly one monolayer. The R_nA product for these junctions is 6.4 $\Omega\mu m^2$. The specific capacitance is a function of the R_nA product. Given the data in Figure 3.14, the specific capacitance at $6.4\Omega\mu m^2$ is estimated to be 150 $fF/\mu m^2$. These junctions have $\omega RC = 1$ at 170 GHz. Junctions with R_nA products of 9.5 $\Omega\mu m^2$ have been fabricated in our lab, and the I-V characteristics of these junctions are only slightly worse than junctions with thicker barriers. Waveguide tuners and integral tuning circuits can be used to resonate out the junction capacitance. The upper-frequency limit for NbN/MgO/NbN mixers will be determined by the Q of the tuning structures used to tune out the junction capacitance.

The tests made at 205 GHz used integral tuning stubs. The Q of the tuning circuits used was roughly 7.5. If similar Q's can be obtained at frequencies near a THz, NbN junctions will be useful up to the gap frequency ($2\Delta_{NbN}/h$=1200 GHz). This simple extrapolation of 205 GHz tests to 1000 GHz neglects several important factors. The loss in NbN tuning circuits and the impedance to which a waveguide mixer block can match will not be constant with frequency.

Inductive tuning circuits near a THz may encounter several problems. Microstrip line stubs may be lossy at these frequencies. We have begun investigating possible loss mechanisms in NbN films and

microstrip lines at millimeter and submillimeter wavelengths. Theoretical calculations based on the Mattis-Bardeen theory indicate that NbN transmission lines should be adequate upto the gap frequency; however, initial experimental evidence indicates that there may be an additional loss mechanisms in NbN at low frequencies (100 to 200 GHz). Accurate characterization of loss in NbN circuits is necessary to determine at what frequencies and for what Q's tuning circuits will work.

Waveguide mixer blocks will become increasingly lossy at higher frequencies, so the 205 Ghz test may not scale to higher frequencies. The mixer block can match to a broad range of junction impedances and may be tuning out a significant fraction of the junction capacitance. At higher frequencies, waveguide mounts will have more loss, and will not be able to match to as broad an impedance range. At very high frequencies (1 THz), fabrication of wave guide mixers may be impossible because of the small waveguide dimensions. Open-structure receivers can be fabricated even at very high frequencies, but in an open-structure mixer, there are no external tuning circuits. All tuning of the junction capacitance must be done with integral tuning circuits. Extremely accurate characterization of tuning circuits and junction properties would have to be made in an open-structure receiver. Despite these problems, if tuning circuits with quality factors of 7 can be fabricated, NbN/MgO/NbN mixers should work up to the gap frequency.

NbN junctions have several advantages over lead-alloy and Nb junctions at high frequencies. Superconductors are lossy above the gap frequency ($2\Delta/h$). This implies that PbInAu is lossy above 550 GHz, and Nb is lossy above 680 GHz. Above the gap frequency, the junctions can still be efficient mixers, but tuning circuits will be very lossy. Another limitation associated with the gap is the drop-back voltage. As discussed in the first chapter, the drop-back voltage increases with decreasing RC products. Experimentally, the highest current density Nb and Pb-alloy junctions have almost no stable bias voltage below the energy gap. Magnetic fields are needed to suppress the Josephson effect. Suppressing the Josephson effect in submicron junctions is difficult, because a quantum of magnetic flux must pass through the barrier region. The drop-back voltage may prove to be a limiting factor in the high-frequency operation of Pb-alloy or Nb mixers.

For NbN junctions to be competitive with Pb-alloy or Nb junctions at low frequencies, the I-V characteristics must be sharp compared to a photon step ($V_{photon} = h\nu/e$). This corresponds to 0.8 mV at 205 GHz. Typical NbN junctions have gap widths of 1.0 mV. Because of gap-smearing, mixer-noise temperatures of NbN junctions at 205 GHz are 2 to 3 times worse than Pb-alloy junctions in the same receiver. Some NbN junctions have gap widths as low as 0.6 mV. Further work fabricating junction on heated substrates may yield sharper I-V characteristics and improve low-frequency performance; however, NbN junctions will be most useful in the submillimeter wavelength range

B. Submicron Devices

To take advantage of the low R_nA junctions mentioned above, submicron junctions need to be fabricated. The normal state resistance of a junction used as a mixer is typically 50 Ω. For a 6.4 $\Omega\mu m^2$ junction, the junction area would be .13 μm^2. To obtain junctions this small, either electron-beam lithography or edge-geometry junctions are needed.

Edge-junctions have already been fabricated with areas of 0.1 μm^2 (Hunt *et al.*, 1989). This corresponds to a 0.1 μm base electrode and a 1 μm-wide counter electrode. To reach their ultimate limit, edge-junctions need to be fabricated at the highest critical current density. Future work on edge-junctions will be in improving the quality of high current density devices. In particular, gap-smearing needs to be reduced in these junctions.

Submicron Mesa or cross-line junctions can be fabricated using e-beam lithography. The minimum feature that can be directly written with e-beam lithography is roughly 10 nm. Difficulties in fabricating e-beam junctions will come from processing problems, not lithography. Planarization of submicron junctions using self-aligned liftoff will be difficult. A process was developed for planarization and etch-back using spin-on glass. This process was described in Chapter two. An I-V characteristic of a 1 μm^2 junction fabricated using this process is shown in Figure 4.1. Reactive ion etching may undercut the mesa, causing shrinkage in the junction dimensions. The etching step may also cause damage near the edge of the mesa. This damage would affect the I-V characteristics of submicron junctions much more than larger junctions. A process to fabricate e-beam-defined submicron junctions at JPL is currently being developed, and these problems are being addressed.

C. New Barriers and New Superconducting Materials

MgO oxide is used as a barrier because it helps stabilize the NbN counter electrode in the B1 phase. The barrier material determines the RC product for a junction. Barrier materials with lower barrier heights and smaller relative dielectric constants will have a smaller RC product for a given thickness barrier. For this reason, the search for new barrier materials is very important. In addition, other kinds of barriers may lead to more uniform and reproducible junctions.

The easiest method for fabricating uniform reproducible barriers for Josephson circuit applications is to deposit a metallic overlayer and to oxidize this layer. This method is used very successfully for Nb/Al-AlO_x/Nb junctions. Attempts at using overlayers of Al and Mg on NbN have already failed. One of the problems is that no lattice match exists to help stabilize the counter electrode, since the thermal oxides are amorphous. Additionally, many metals diffuse into NbN along the grain boundaries. For a metallic overlayer to be successful, the metal cannot diffuse into the NbN, and some other method must be used to stabilize the counter electrode in the B1 phase. The most likely method of stabilizing the counter electrode

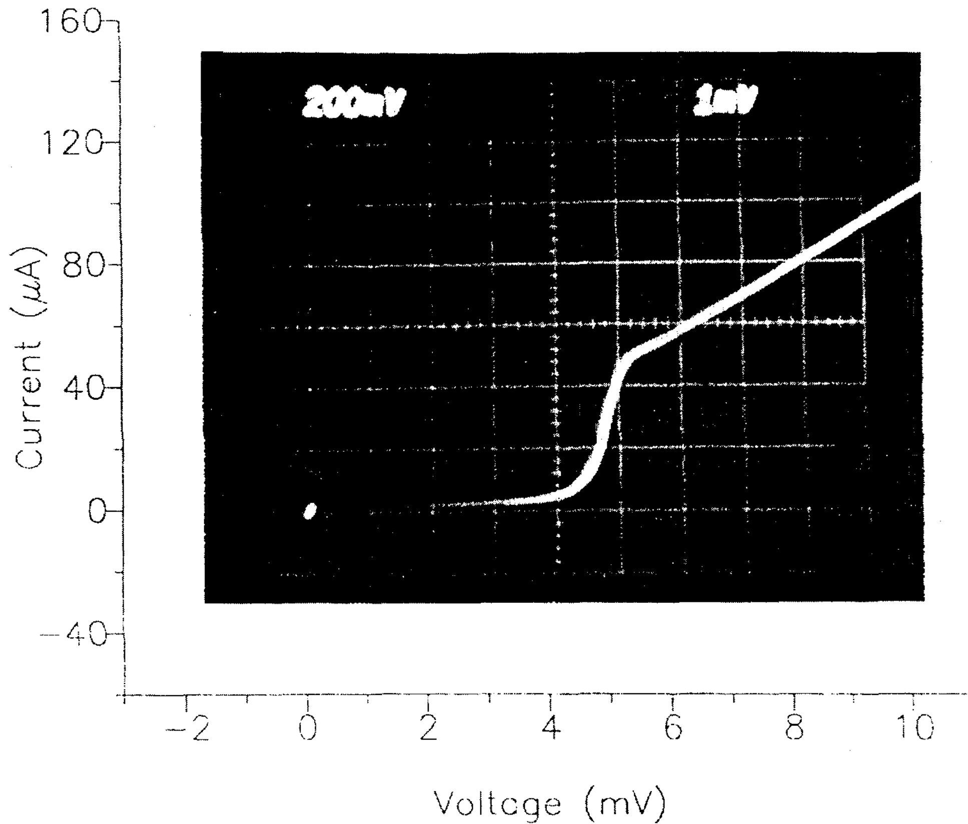

Figure 4.1 I-V characteristic for a junction fabricated using the SOG etch back process.

is substrate heating.

When searching for new as-deposited barriers, as opposed to metallic overlayers, several factors are important. The barrier should have a lattice match with NbN, so it will grow epitaxially. The barrier should wet the NbN surface, so the barrier will be continuous for thin layers. Predicting how a barrier will grow on NbN is difficult.

Aluminum nitride barriers were tried with NbN at JPL (LeDuc, 1987). Aluminum nitride was chosen as a barrier material for several reasons. NbN/AlN multilayers were deposited at Argon laboratories for magnetic measurements (Murduck *et al.*, 1988; Gray *et al.*, 1988). TEM photos of these multilayers showed excellent growth of AlN on NbN. The layers were well separated even for thin layers. There is a lattice match between the (111) surface of NbN and the (100) surface of AlN, which is hexagonal. Only limited success was had by LeDuc in fabricating NbN/AlN/NbN junctions. The gap of these junctions was always small (less than 4 mV), and the subgap conduction was large. The results indicate that the counter electrode was not growing polyepitaxially on the barrier. The search for new barrier materials is difficult, but it is an important area for future work.

There are other superconductors that could be used in fabricating large gap voltage SIS mixers. Several

A15 superconductors have transition temperatures higher than NbN (Nb_3Ge has a transition temperature of 23 K). The larger transition temperatures are advantageous in applications where the operating temperatures are around 10 K. The difficulty with these materials is to stabilize the superconducting phase. Typically, these materials are deposited at substrate temperatures in excess of 1000° C. At these temperatures, thin barriers will be destroyed by thermal expansion. In addition, the counter electrode must be superconducting in the first electronic coherence length, which is short in A15 materials (approximately 3 nm). Because of these problems, success in fabricating junctions with A15 superconductors has been extremely limited.

The discovery of high-temperature superconductivity has created a new class of materials to consider for SIS junction fabrication; however, there are many difficulties in fabricating tunnel junctions from oxide superconductors. Most importantly, no superconducting energy gap has been seen definitively in a tunneling experiment with these materials. Additionally, the surface morphology of even the epitaxial films is very rough and uneven. This makes covering the base layer with an artificial barrier difficult. The barrier material used cannot chemically reduce the superconductor. This rules out the simplest barriers, oxidized metallic overlayers, because materials like Al would remove oxygen from the superconductor. Oxide barriers, like MgO, are promising in this regard. Stabilizing the oxide-superconductor counter electrode will be more difficult than stabilizing NbN counter electrodes. Finally, the high substrate temperatures necessary to deposit these films are high (approximately 500° C). Oxide superconductor-based SIS tunnel junctions are not likely to be of use as mixers in the near future. The most probable use for these materials will be as weak-link Josephson junctions in small-scale integrated circuits, such as SQUID magnetometers. Significant progress has already been made in this area (Laibowitz *et al.* 1990).

D. Operation of NbN Junctions on Closed-Cycle Refrigerators

Operation of NbN mixers near 10 K is an attractive possibility for the future. In many remote locations such as satellites, liquid helium is not a practical refrigerant, because of its cost and the difficulty in shipping it to a remote location. Mixers based on NbN junctions could be cooled using two-stage, closed-cycle refrigerators. In Chapter three, junction I-V characteristics were presented as a function of temperature, and loss in NbN films was analyzed as a function of temperature. Given this information, the maximum operating temperatures for NbN junctions and probable operating points for refrigerators are discussed.

For mixer applications, the important I-V parameters are the subgap leakage and the width of the gap voltage. As temperature is increased, the subgap leakage degrades rapidly, as is shown in Figures 3.9 and 3.10; however, the I-V characteristic in Figure 3.9 is still reasonably nonlinear at 9 K. Above this temperature, the I-V quality degrades rapidly with increasing temperature. Operation of mixers in the 8 to 9 K range should be feasible, with some degradation of mixer noise and conversion gain relative to 4.2 K operation. At 9 K, the I-V characteristic will be very sensitive to the transition temperature of the

NbN. The transition temperatures of the base and counter electrodes should be in the 16 to 17 K range to obtain as sharp an I-V characteristic as possible. To obtain high transition temperature films, the junction trilayers should be deposited at elevated substrate temperatures. Regardless of the electrodes' transition temperature, the mixer performance will degrade rapidly above 10 K.

The RF loss in NbN films is a strong function of temperature; this has a large impact on mixer design. Loss in NbN microstrip lines was calculated using the Mattis-Bardeen theory. These calculations predict that the loss at 8 K and 205 GHz in NbN films will be large (7% per wavelength) even for thick NbN films (1 μm). This is very discouraging for elevated temperature operation of NbN mixers. With this large a loss, NbN tuning circuits will not work well. The alternative to NbN tuning circuits is normal-metal tuning circuits. Materials like Au have very large DC conductivities at 10 K; however, at millimeter wavelengths the anomalous skin depth will make the RF surface conductivity much larger than the DC conductivity. Normal-metal tuning circuits need to be analyzed further to determine how effective they will be at submillimeter wavelengths.

There are several types of refrigerators that can be used to reach cryogenic temperatures. The general tradeoffs are complexity or efficiency versus operating temperature. The simplest refrigerators are two-stage helium refrigerators. These refrigerators operate by compressing and expanding helium gas. The first stage cools the compressed gas for the second stage. Two-stage helium refrigerators are extremely reliable. Cryopumps, commonly used on vacuum systems, operate unattended for months at a time. Unfortunately, commercially available two-stage refrigerators reach only 12 K. Slightly lower temperatures may be possible in two-stage refrigerators at the expense of cooling efficiency. To reach significantly lower temperatures, a third refrigerator stage must be used. The typical third stage is a Joule-Thompson (J-T) valve. A J-T valve is a small orifice through which the compressed gas expands. Helium gas can be liquefied using a J-T valve. The problem with J-T valves is that they can be clogged by impurities in the helium. Generally, three-stage J-T refrigerators are much less reliable than two-stage refrigerators; however, three-stage refrigerators have been used at the Owens valley radio observatory for many years to cool SIS mixers (Woody, 1986). These refrigerators work continuously for up to 6 months. Other kinds of third stages may be more reliable than J-T expanders. For example, third stages based on adiabatic demagnetization can be used. These stages do not use helium gas, and have no moving parts. Finally, mixers can be operated at 12 K with degraded performance. The ultimate solution will involve improving junction transition-temperatures, i mproving refrigerator technology, and lowering the requirements on mixer performance.

Appendix A. The Josephson Effect

In this appendix the Josephson equations are derived using an argument first proposed by Feynman (1963). Next, these equations are used to calculate the properties of a symmetric DC SQUID. Finally, the response of a junction to a constant DC bias voltage is examined.

Josephson Equation

Consider two superconductors separated by a very thin insulating barrier. Each superconductor can be described by a macroscopic wave function

$$\Psi_i = \sqrt{\rho_i}\, e^{i\theta_i}, \quad i = 1, 2, \qquad \text{A.1}$$

where ρ_i is the density of Cooper pairs, and θ_i is the macroscopic phase of the wave function. If there is an overlap of the two wave-functions characterized by an overlap integral K, we have

$$i\hbar \frac{d\Psi_1}{dt} = U_1\Psi_1 + K\Psi_2$$

$$i\hbar \frac{d\Psi_2}{dt} = U_2\Psi_2 + K\Psi_1, \qquad \text{A.2}$$

where U_i is the chemical potential of each superconductor. If the two superconductors are linked together through a battery with a potential V, we can let

$$U_1 = e^*V/2, \; U_2 = -e^*V/2, \qquad \text{A.3}$$

where e^* is the charge of a Cooper pair. Plugging A.1 and A.3 in to A.2, and separating real and imaginary parts we have

$$\dot{\rho}_1 = \frac{2K}{\hbar}\sqrt{\rho_1\rho_2}\,\sin\phi,$$

$$\dot{\rho}_2 = \frac{-2K}{\hbar}\sqrt{\rho_1\rho_2}\,\sin\phi, \qquad \text{A.4}$$

$$\dot{\theta}_1 = \frac{K}{\hbar}\sqrt{\rho_2/\rho_1}\,\cos\phi \; - \frac{e^*}{2\hbar}\,V,$$

$$\dot{\theta}_2 = \frac{K}{\hbar}\sqrt{\rho_1/\rho_2}\,\cos\phi \; + \frac{e^*}{2\hbar}\,V, \qquad \text{A.5}$$

where $\phi = \theta_2 - \theta_1$. We can associate $\dot{\rho}_1 = -\dot{\rho}_2$ with the pair current flow from superconductor 1 to 2, because ρ_i is the density of pairs. Because the two superconductors are linked through an external circuit, there is no net change in ρ_i. This leads to Josephson's first equation

$$J = J_0 \sin\phi, \; J_0 = \frac{2Ke^*}{\hbar}\sqrt{\rho_1\rho_2}. \qquad \text{A.6}$$

Subtracting the two equations in A.5, we have the second Josephson equation,

$$\dot{\phi} = e^*V/\hbar, \text{if } e^* = 2e, \text{ then } \dot{\phi} = 2eV/\hbar. \qquad \text{A.7}$$

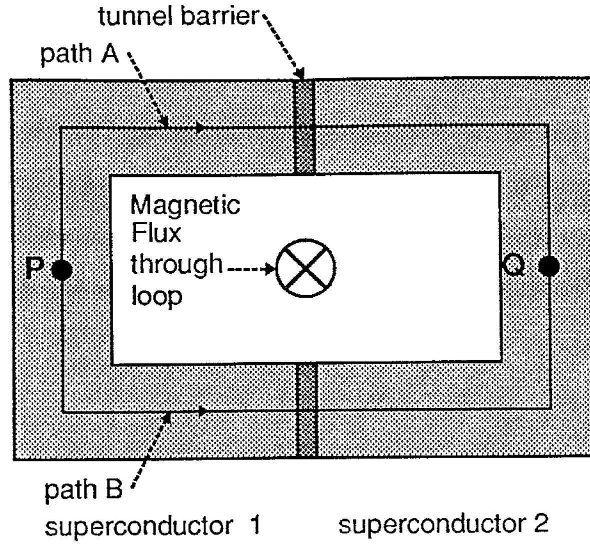

Figure A.1 SQUID schematic. The SQUID shown above is a superconducting loop broken by two tunnel barriers.

SQUID Theory

Consider a superconducting loop with two identical Josephson junctions as is shown in Figure A.1. Again we have the macroscopic wave function $\Psi = \sqrt{\rho}\, e^{i\theta}$. The pair current in the superconductor is

$$\mathbf{J} = \hbar/m^* \, (\nabla\theta - \frac{e^*}{\hbar}\,\mathbf{A})\rho., \tag{A.8}$$

where **A** is the vector potential of the magnetic field, **J** is the pair current density, and m* is the mass of the pair. If we are far from the surface of the superconductor, then **J** = 0, so we have

$$\nabla\theta = \frac{e^*}{\hbar}\,\mathbf{A}. \tag{A.9}$$

Consider two paths from point P to point Q; one is along path A and the other is along path B. Taking the path integral of A.9 we have

$$\int_{\text{path A}} \nabla\theta \cdot d\mathbf{l} = \phi_a + \frac{e^*}{\hbar} \int_{\text{path A}} \mathbf{A} \cdot d\mathbf{l}$$

$$\int_{\text{path B}} \nabla\theta \cdot d\mathbf{l} = \phi_b + \frac{e^*}{\hbar} \int_{\text{path B}} \mathbf{A} \cdot d\mathbf{l}, \tag{A.10}$$

where ϕ is the phase change of θ across the tunnel barrier. The phase of the wave function is unique to within a factor of $2\pi n$, so the two integrals must be equal within a factor of $2\pi n$. Equating Equations A.10 and rearranging the terms we have

$$\phi_a - \phi_b = 2\pi n + \frac{e^*}{\hbar} \oint_{\text{path A}-\text{B}} \mathbf{A} \cdot d\mathbf{l}. \tag{A.11}$$

The closed-loop integral of the vector potential is the magnetic flux Φ passing through the loop. Therefore, we have

$$\phi_a - \phi_b = 2\pi n + \Phi/\Phi_0, \text{ where } \Phi_0 = \hbar/2e. \tag{A.12}$$

In the case where the loop inductance is negligible ($LI_c \ll \Phi_0$), $\Phi = \Phi_{external}$. Let the two phases be

$$\phi_a = \phi_0 + \Phi_{external}/2\Phi_0, \; \phi_b = \phi_0 - \Phi_{external}/2\Phi_0 + 2\pi n. \tag{A.13}$$

Using A.6, we have

$$I_{total} = I_0 \sin \phi_0 \cos (\Phi_{external}/2\Phi_0). \tag{A.14}$$

The phase ϕ_0 can be adjusted by controlling the current flowing in the external circuit, so the maximum current that can pass through the SQUID in the zero voltage state is

$$I_{maximum} = I_0 \left|\cos (\Phi_{external}/2\Phi_0)\right|. \tag{A.15}$$

The maximum critical current will be a periodic function of external magnetic flux. If the loop inductance is not negligible, the phase difference in the junctions will create circulating currents that will partially cancel the external flux. The flux in the loop becomes

$$\Phi = \Phi_{external} + LI_0/2 \times (\sin \phi_b + \sin \phi_b). \tag{A.16}$$

In real SQUIDs, the maximum critical current never modulates to zero. Additionally, if $\beta_e \equiv 2\pi LI_0/\Phi_0$ is larger than one, then circulating currents caused by the phase difference can add or subtract fluxons to the loop (Barone and Paternò, 1982). This creates metastable states for the SQUID. External noise can switch the SQUID between various states. SQUIDs that have β_e larger than one are called hysteretic SQUIDs. Another often seen effect which is that the individual junctions will have their critical currents modulated by magnetic flux entering the barrier region. This results in a sin (x)/x modulation of I_0 versus $\Phi_{external}$. An example of this is shown in Chapter 3.

Response of a Josephson Junction to a Constant DC Bias Voltage

If a stiff voltage source is put on a Josephson junction, it will oscillate at a frequency proportional to that voltage. Consider the second Josephson Equation A.7. If we integrate this equation, we have

$$\phi = \phi_0 + 2eV_{DC}/\hbar \times t, \tag{A.17}$$

where ϕ_0 is a constant. Plugging the time-dependent phase into the first Josephson Equation (A.6), we get

$$J = J_0 \sin(2eV_{DC}/\hbar \times t). \tag{A.18}$$

The junction has a sinusoidal current flowing in it at a frequency proportional to the DC voltage. The proportionality constant between the voltage and frequency is $2e/h = 484$ MHz/μV. A Josephson junction is a voltage-controlled oscillator. In the case of a real Josephson junction, which has capacitance and is biased with a load resister, the oscillations are not sinusoidal, but have higher harmonic content. Even in the situation of complicated embedding impedances, the junction will oscillate at the same fundamental frequency. This effect is taken advantage of in many circuits.

Appendix B. Photoresist Processing

This appendix is a summary of photolithography processes used for several resists. All lithography was done on a Carl Suss MJB-3 contact mask aligner at a wavelength of 315 nm. The thickness and material of the mask plates affect the exposure intensities. Exposure intensities are given for 0.032" white-crown mask plates. Exposures were made in the vacuum contact mode for optimum resolution.

AZ 5214-E (and AZ 5206-E) processing, positive tone

1. Prime sample HMDS 1 min.
2. Spin sample dry 4000 rpm
3. Spin on AZ 5200 resist 4000 rpm
4. Soft bake on hot plate at 95 °C for 2 min.
5. Expose sample 185 mJ/cm^2 (92 mJ/cm^2)
6. Develop sample AZ 400K 1:4 H_2O 1 min.
   (AZ developer can also be used if Al processing is done)
7. Rinse sample in DI H_2O

AZ 4330-RS (AZ 4110) processing

1.-4. as above

5. Expose samples 1060 mJ/cm^2 (540 mJ/cm^2)
6. Develop samples AZ 400K 1:4 H_2O 3 min.
7. Rinse sample in DI H_2O

AZ 5214-E image reversal

1.-4. as above

5. Expose sample 470 mJ/cm^2
6. Post-exposure bake on a hot plate at 105 °C for 2 min.
7. Flood expose sample 470 mJ/cm^2
8. Develop AZ 400 K 45 sec.
9. Rinse sample in DI H_2O

Image reversal of AZ 5200 works by the creation of an acid in the first exposure. During the post-exposure bake this acid acts to catalyze a reaction, which reduces the solubility of the resist in the basic developer. The flood exposure then exposes all the resist, so the uncatalyzed resist will be removed in the

developer. For the conditions listed above, the resist profile is close to vertical. If the first exposure time and the post exposure bake time are reduced, only the top layer of resist is catalyzed. When the resist is developed, the bottom layer of resist is undercut. The degree of undercutting can be adjusted by altering these times. This undercutting is a problem for small, light-field patterns (since they will develop away), but it is very useful for liftoff stencils, where an undercut resist profile is desired.

Appendix C. SQUID Measurement Circuit

SQUID measurements involve measuring junction critical current versus control current. There are several difficulties involved in this problem. The control line is direct-coupled, so it is electrically connected to the wiring and counter electrode. This means that either the I-V or control current measurement must be a floating measurement. Additionally, the maximum value of the critical current must be measured. This appendix describes the electronics used to measure SQUID modulation curves. The circuit used is shown in Figure C.1.

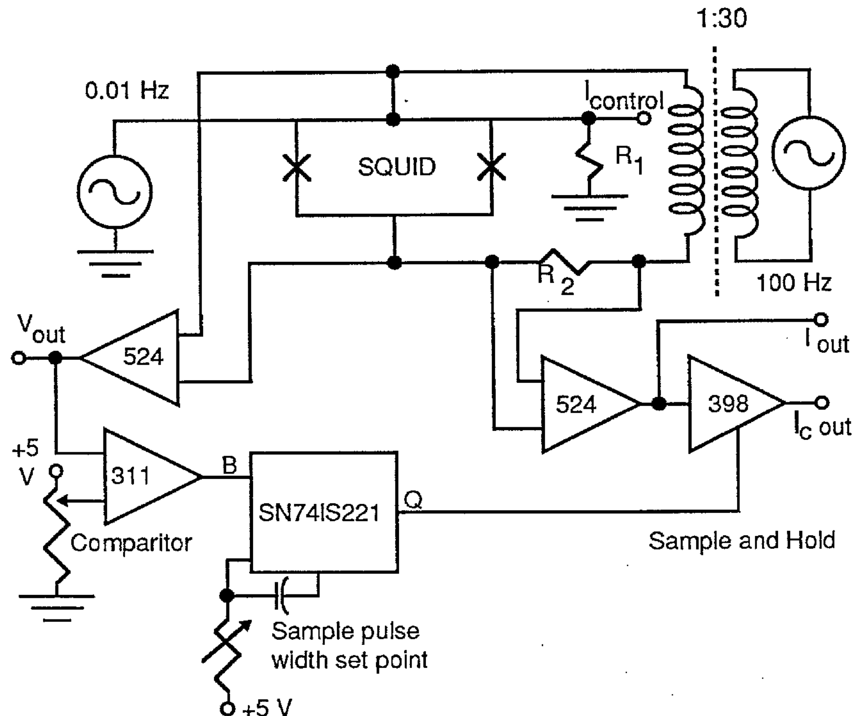

Figure C.1 SQUID measurement circuit. This circuit is used to measure critical current as a function of control current for an undampened DC SQUID. The I-V measurement is floating and is driven through a step-down transformer. The critical current is measured by holding the current level, at which the interferometer switches out of the zero voltage state.

The measurement circuit works as follows. The I-V measurement is floating. The SQUID drive is isolated by a transformer. The voltage measurement is made with an Analog Devices 524 instrumentation amplifier. The current in the sense resistor (R_2) is also measured using an AD 524. The critical current is measured by storing the current value at which the SQUID switches out of the zero voltage state. This current level is stored using a sample and hold circuit. The voltage level is compared to a set value by the 311 comparator chip. On the positive edge of the comparator transition, an SN741S221 monostable is triggered; the monostable outputs a pulse whose width is controllable by a variable resistor and a capacitor.

This pulse width sets the sample period for the 398 sample and hold. The sample period is typically 10-20 μsec. Because the I-V sweep rate is fairly slow (100 Hz), the sampling time introduces very little error in the critical current measurement. The control current is driven directly through the SQUID and through a current sense resistor (R_1). The drive to the control line is a triangle wave at a very low frequency (typically 0.01 Hz). The output of the sample and hold and the voltage across R_1 are input into an X-Y recorder. The trace on the X-Y recorder is then critical current versus control current.

Appendix D SQUID Data Summary

ID no.	R_nA ($\Omega\mu m^2$)	Junction Area (μm^2)	Line Width (μm)	Line Length (μm)	ΔI_c (μA)	V_r (μV)	L (pH)	λ_{NbN} (nm)	Total Capacitance (fF)	Specific Capacitance (fF/μm^2)
1	128.	16.0	4.	40.0	74.0	72.0	28.0	466.	748.	46.7
2	112.	16.0	8.	86.0	57.0	54.0	36.3	536.	1024.	64.0
3	112.	16.0	4.	80.0	40.5	48.0	51.1	442.	921.	57.6
4	136.	4.0	2.	40.0	52.0	108.0	39.8	381.	234.	58.4
5	164.	4.0	4.	86.0	44.7	106.0	46.3	411.	208.	52.1
6	160.	4.0	2.	80.0	28.0	80.0	73.9	363.	229.	57.3
7[2]	244.	4.0	2.	30.0	85.0	—	24.4	332.	—	—
8	408.	4.0	2.	30.0	65.0	140.0	31.8	384.	174.	43.4
9	304.	4.0	2.	80.0	25.3	80.0	81.8	375.	207.	51.8
10	312.	4.0	4.	86.0	38.0	110.0	54.5	439.	165.	41.1
11	380.	4.0	2.	40.0	42.0	122.0	49.3	421.	148.	37.0
12[2]	344.	4.0	4.	86.0	41.0	—	50.5	410.	—	—
13	316.	4.0	2.	30.0	62.0	142.0	33.4	387.	161.	40.3
14	224.	16.0	4.	40.0	67.0	62.0	30.9	471.	913.	57.1
15	240.	16.0	4.	80.0	38.0	42.0	54.5	437.	1129.	70.5
16[2]	224.	16.0	4.	80.0	37.0	—	55.9	444.	—	—
17	360.	4.0	2.	40.0	65.0	154.0	31.8	328.	144.	35.9
18	360.	4.0	4.	86.0	58.0	118.0	35.7	347.	218.	54.6
19	220.	4.0	2.	80.0	29.3	90.0	70.6	352.	190.	47.4
20	288.	4.0	2.	30.0	82.0	170.0	25.2	341.	149.	37.2
21	240.	16.0	4.	40.0	139.0	112.0	14.9	333.	581.	36.3
22	192.	16.0	8.	86.0	115.0	88.0	18.0	375.	778.	48.6
23	160.	16.0	4.	80.0	61.0	70.0	33.9	365.	652.	40.8
24	240.	16.0	4.	80.0	68.0	72.0	30.4	338.	687.	43.0
25	496.	16.0	4.	80.0	42.0	62.0	49.3	464.	573.	35.8
26	176.	16.0	4.	40.0	132.0	104.0	15.7	334.	639.	40.0
27	352.	16.0	4.	80.0	64.0	68.0	32.3	341.	725.	45.3
28[2]	80.	4.0	2.	40.0	65.4	—	31.7	327.	—	—
29[2]	80.	4.0	2.	30.0	94.0	—	22.0	310.	—	—
30[2]	82.	16.0	8.	86.0	144.0	—	14.4	320.	—	—
31	84.	4.0	4.	86.0	68.0	110.0	30.4	316.	294.	73.6
32[2]	88.	4.0	2.	80.0	42.0	—	49.3	276.	—	—
33[2]	58.	16.0	8.	86.0	132.0	—	15.7	330.	—	—
34	59.	16.0	4.	80.0	65.5	54.0	31.6	336.	1177.	73.6
35[2]	76.	4.0	2.	30.0	118.0	—	17.5	251.	—	—
36[2]	76.	4.0	2.	80.0	45.4	—	45.6	246.	—	—
37[2]	76.	4.0	4.	86.0	105.0	—	19.7	213.	—	—
38	58.	16.0	4.	40.0	164.0	90.0	12.6	274.	1061.	66.3
39	54.	16.0	8.	86.0	132.0	76.0	15.7	316.	1198.	74.8
40	56.	16.0	4.	80.0	90.0	64.0	23.0	256.	1151.	72.0
41	64.	16.0	4.	80.0	89.0	67.0	23.3	258.	1039.	64.9
42[2]	72.	4.0	2.	30.0	94.0	—	22.0	297.	—	—
43	30.	16.0	4.	40.0	143.0	71.0	14.5	303.	1486.	92.9
44	30.	16.0	4.	80.0	76.0	54.0	27.2	290.	1366.	85.4
45	144.	4.0	2.	30.0	49.0	95.0	42.2	452.	284.	71.1
46[1]	38.	9.5	3.	42.0	125.0	83.0	16.6	265.	871.	91.7
47[1]	456.	9.5	3.	42.0	51.0	70.0	40.6	473.	465.	49.0
48[1,2]	114.	9.5	3.	42.0	87.0	—	23.8	341.	—	—
49[1]	33.	9.5	3.	42.0	88.0	65.0	23.5	338.	1011.	106.5

50[1]	30.	9.9	3.	42.0	71.0	68.0	29.2	388.	725.	73.2
51[1]	86.	8.7	3.	42.0	104.0	88.0	19.9	303.	624.	71.7
52[1]	133.	9.5	3.	42.0	86.0	81.0	24.1	344.	607.	63.9
53[1]	19.	9.7	3.	42.0	96.0	76.0	21.6	319.	791.	81.5
54[1]	105.	9.5	3.	42.0	85.0	83.0	24.4	346.	567.	59.6
55[1]	241.	7.3	3.	42.0	46.0	66.0	45.0	501.	473.	64.8
56[1]	98.	10.0	3.	42.0	94.5	88.0	21.9	320.	559.	55.9
57[1]	77.	9.9	3.	42.0	90.0	74.0	23.0	331.	781.	78.9
58[1,2]	33.	9.3	3.	42.0	74.0	—	28.0	374.	—	—

[1] Mesa junction, 80 fF of parasitic capacitance subtracted.

[2] No resonance step measured.

Description of Table Headings

The table headings have the following meaning: "R_nA" is the normal-resistance area product for the junctions in the SQUID. "Junction Area" is the area of each junction. "Line Width" is the width of the microstrip line connecting the two junctions. "Line Length" is the length of the microstrip line connecting the two junctions. "ΔI_c" is the period of the critical current of the SQUID as a function of control current. "V_r" is the value of the resonant voltage step in the I-V characteristic. "L" is the measured inductance of the microstrip line connecting the two junctions. "λ_{NbN}" is the magnetic penetration depth of the NbN film. "Total Capacitance" is the capacitance of one of the junctions calculated using Equation 3.5. Specific capacitance is the total capacitance minus the parasitic capacitance divided by the junction area.

Appendix E. RF Testing Summary

Junction ID no.[3]	R_n (Ω)	L_{stub} (μm)	W_{stub} (μm)	T_{phys} (K)	ν_{signal} (GHz)	Capacitance Tuned (fFarad)	n	T_m (K)	η_c $\times 10^{-2}$	η_a $\times 10^{-2}$
1.1	47.5	0.0	0.0	4.2	205.0	0.	2	767.	0.99	1.20
1.2	45.0	104.	4.5	4.2	205.0	-19.	2	644.	1.21	1.52
1.2				1.5	205.0	-19.	2	605.	1.26	1.75
1.3	48.4	111.	4.5	4.2	199.8	-27.	2	1085.	0.61	0.94
1.3				4.2	202.6	-31.	2	1082.	0.62	0.99
1.3				4.2	205.4	-35.	2	1079.	0.70	0.89
1.4[1]	45.0	90.	4.5	4.2	199.6	19.	2	398.	1.82	2.16
1.4				4.2	202.6	16.	2	394.	1.86	2.26
1.4				4.2	203.6	15.	2	568.	1.42	1.68
1.4				4.2	206.4	12.	2	633.	1.34	1.46
1.5[1,2]	61.0	74.	4.5	4.2	199.5	69.	2	464.	1.87	2.19
1.5				4.2	202.3	64.	2	445.	1.89	2.19
1.5				4.2	205.6	58.	2	376.	2.41	2.80
1.5				4.2	208.4	53.	2	403.	2.31	2.67
1.5				4.2	208.4	53.	1	440.	1.50	2.07
1.5				1.5	199.7	69.	2	386.	2.16	2.52
1.5				1.5	199.7	69.	2	451.	1.22	1.71
1.5				1.5	202.5	63.	2	410.	2.18	2.53
1.5				1.5	202.5	63.	2	394.	1.43	2.07
1.5				1.5	205.6	58.	2	325.	2.67	3.03
1.5				1.5	205.6	58.	1	376.	1.62	2.37
1.5				1.5	208.4	53.	2	359.	2.47	2.79
1.5				1.5	211.8	48.	2	533.	1.72	2.01
2.1	64.0	75.	4.5	4.2	199.8	111.	2	298.	3.02	3.23
2.1				4.2	202.6	102.	2	275.	3.18	3.45
2.1				4.2	204.0	98.	2	251.	3.28	3.57
2.1				4.2	206.4	92.	2	248.	3.49	3.99
2.1				4.2	210.4	83.	2	345.	2.48	2.75
2.1				1.5	199.7	111.	2	183.	5.12	5.45
2.1				1.5	202.7	102.	2	155.	6.08	6.53
2.1				1.5	203.6	99.	2	170.	5.33	5.89
2.1				1.5	206.4	92.	2	133.	6.44	6.97
2.2	61.0	75.	7.0	4.2	199.5	174.	2	358.	3.02	3.13
2.2				4.2	202.3	161.	2	336.	2.91	3.05
2.2				4.2	205.7	146.	2	250.	4.24	4.41
2.2				4.2	208.5	135.	2	244.	4.08	4.25
2.2				1.5	199.5	174.	2	300.	4.65	4.71
2.2				1.5	202.3	161.	2	254.	4.49	4.54
2.2				1.5	205.7	146.	2	188.	7.05	7.20
2.2				1.5	208.5	135.	2	164.	7.28	7.42
2.3	71.0	80.	4.5	4.2	199.8	82.	2	222.	4.39	4.79
2.3				4.2	202.6	76.	2	185.	5.17	5.64
2.3				4.2	205.6	70.	2	245.	3.42	3.80
2.3				4.2	208.4	65.	2	251.	3.22	3.63
2.3				1.5	199.7	82.	2	151.	6.52	6.94
2.3				1.5	202.5	76.	2	134.	7.08	7.63
2.3				1.5	205.6	70.	2	190.	4.50	4.97
2.3				1.5	208.4	65.	2	206.	4.11	4.54
2.3				1.5	211.9	59.	1	591.	1.16	1.79

2.4	68.0	0.	0.0	4.2	199.6	0.	1	1664.	0.35	0.49
2.4				4.2	202.3	0.	1	2688.	0.22	0.31
2.4				4.2	205.5	0.	1	2871.	0.22	0.29
2.4				4.2	208.3	0.	1	2740.	0.24	0.33
2.4				1.5	202.5	0.	1	2116.	0.27	0.37
2.4				1.5	205.5	0.	1	2477.	0.26	0.35
2.4				1.5	208.3	0.	1	2180.	0.27	0.38
2.5	80.0	86.	4.5	4.2	199.6	59.	2	585.	1.34	1.46
2.5				4.2	202.4	54.	2	580.	1.27	1.38
2.5				4.2	205.5	49.	2	725.	1.18	1.28
2.5				4.2	208.3	46.	2	789.	1.04	1.18
2.5				1.5	202.3	54.	2	501.	1.40	1.49
2.5				1.5	205.5	49.	2	697.	1.22	1.30
2.5				1.5	208.3	46.	2	819.	1.12	1.18

[1] Asymmetric antenna structure; junction mounted at edge of waveguide.

[2] Junction stub shortened by scribing off the end of the stub under a microscope using a micro manipulator.

Description of Table Headings

The table headings have the following meaning: "Junction ID number" refers to different junctions tested; junction numbers 1.X denote junctions from the first batch tested; junction ID numbers 2.X denote junctions from the second batch. "R_n" is the normal state resistance of the junction. "L_{stub}" is the stub length, and "W_{stub}" is the stub width. "T_{phys}" is the physical temperature of the mixer and junction during the mixer measurements. "ν_{signal}" is the signal frequency. "Capacitance tuned" is the calculated value for the amount of capacitance the stub will tune out at the signal frequency. Negative values of capacitance tuned indicates that the stub is capacitive, not inductive, at the signal frequency. "n" is the photon step number; the best results are usually for n=2. "T_m" is the mixer-noise temperature. "η_c" is the coupled conversion gain. "η_a" is the available conversion gain if the IF impedance of the junction were perfectly matched to the IF chain.

Appendix F. Mask-Modification Proceedure

A process was developed to modifiy the length of the tuning stubs on the third mask layer. This process is very important because bandwidth of the tuning stub is small (less than 10%), and it is easy to design the stub for the wrong center frequency. If the stub length can be modified, the center frequency of the tuning circuit can be changed. This process is easy and quick, taking roughly two hours, wheras having a new commercial mask plate made is expensive and time-consuming.

The mask stub length was modified using the following method. The existing mask is copied onto a photoresist and chrome-covered mask blank. The photoresist is developed, but the chrome is not etched. The second mask layer is aligned to this chrome blank. This mask layer consists of 200 μm by 40 μm rectangular holes in a dark field. The junction dot sits in this rectangle, but the dot is irrelevant to this process. These rectangles are aligned so that the end of the stub is visible in this rectangle. A second exposure is made, and the mask is again developed, so the end of the stub is removed. The chrome is then etched. Finally, the mask is copied to restore the right-handedness of the mask.

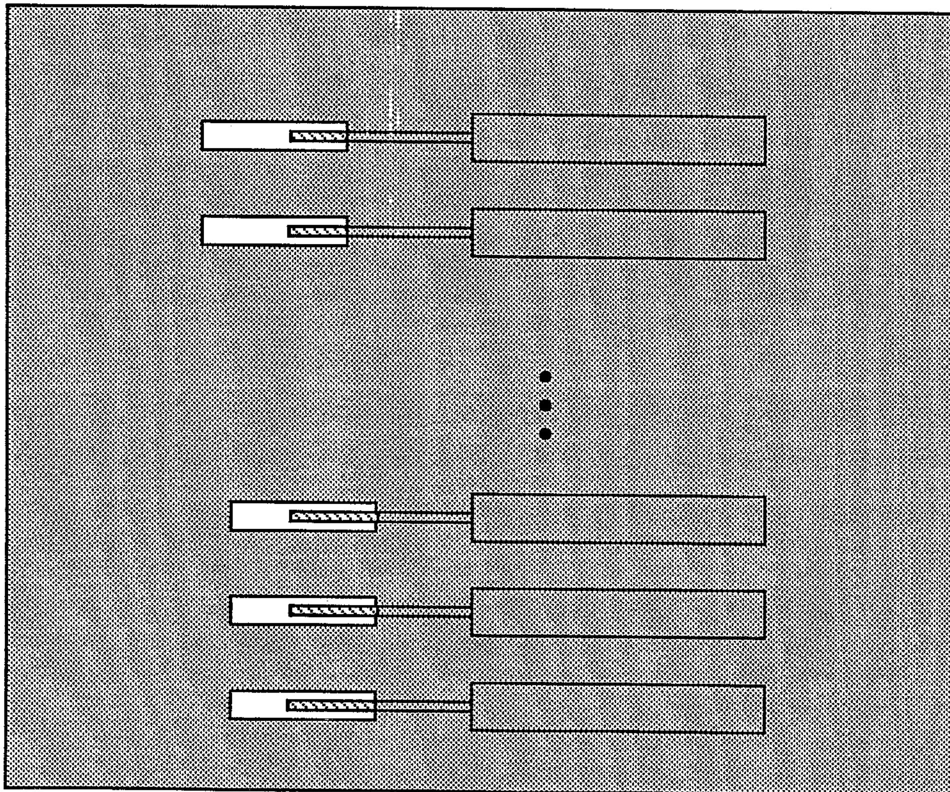

Figure F.1 Mask modification procedure.

A slight variation of this process is actually used. After aligning the rectangles over the stub ends, the mask is rotated slightly. This leads to shorter stubs on one side of the mask and longer stubs on the

other. This alignment is shown in Figure 3.19. The small variation of length across the mask compensates for material variations, which will affect the propagation velocity of the microstrip line. Because the mask aligner has a calibrated micrometer on its x-y stage, stub lengths can be controlled to $\pm 3\ \mu m$. If run-to-run reproducibility of the materials properties is still a problem, two sets of junction can be fabricated in parallel until the final wiring layer etch. One set can be finished and tested. If the stub lengths of the first set are incorrect, the stub length of the second set can be made the correct length using the mask-modification procedure.

References

Aoyagi, M., A. Shoji, S. Kosaka, F. Shinoki, and H. Hayakawa, "A 1 μm Cross-Line Junction Process,"*Advances in Cryogenic Engineering Materials*, vol. 32, Plenum:New York, 1986, pp. 557–563.

Anderson, P. W., and A. H. Dayem, "Radio-Frequency Effects in Superconducting Thin Film Bridges," *Phys. Rev. Lett.*, vol. 13, 195-197, 1964.

Bacon, D. D., A. T. English, S. Nakahara, F. G. Peters, H. Schreiber, W. R. Sinclair, and R. B. van Dover, "Properties of NbN Thin Films Deposited on Ambient Temperature Substrates," *J. Appl. Phys.*, vol. 54, no. 11, 6509–6515, 1983.

Baker, J. M., and J. H. Magerlein, "Tunnel barriers on Pb-In-Au alloy films," *J. Appl. Phys.*, vol. 54, 2556, May 1983.

Bardeen, J., L. N. Cooper, and J. R. Schrieffer, "Theory of Superconductivity," *Phys. Rev.*, vol. 108, 1175–1204, Dec. 1957.

Bardeen, J. "Tunneling From a Many-Particle Point of View," *Phys. Rev. Lett.*, vol. 6, 57-59, 1961.

Barone, A., and G. Paternò, *Physics and Applications of the Josephson Effect*, John Wiley & Sons:New York, 1982.

Beha, H., W. Jutzi, and G. Mischke, "Margins of a 16-pS/bit Interferometer Shift Register," *IEEE Trans. Elect. Devices*, vol. ED-27, no. 10, 1882-1887, October 1980.

Bhushan, M. "NbN Film Deposition using Optical Emission Spectroscopy," *IEEE Trans. Magn.* vol. MAG-23, no. 2, March 1987a.

Bhushan, M. "Analysis of Reactive Sputtering Mechanism for NbN Film Deposition," *J. Vac. Sci. Technol.*, vol. A5, no. 5, 2829-2835, September/October 1987b.

Braginski, A. I., J. Talvacchio, M. A. Janocko, and J. R. Gavaler, "Investigation of Crystalline Oxide Tunnel Barriers Formed by Thermal Oxidation of Metallic Aluminum Overlayers on Superconductor Surfaces," *J. Appl. Phys.*, vol. 60, no. 6, 2058, 1986.

Büttgenbach, T. H., R. E. Miller, M. J. Wengler, D. M. Watson, and T. G. Phillips, *IEE Trans. Microwave Theory Tech.*, vol. MTT-36, 1720–1726, Dec. 1988.

Büttgenbach, T. H., T. D. Groessbeck, and B. N. Ellison, "A Scale Mixer Model for SIS Waveguide Receivers," *Int. J. IR and Millimeter Waves*, vol. 11, no. 1, January 1990.

Cohen, M. H., L. M. Falicov, and J. C. Phillips, "Superconductive tunneling," *Phys. Rev. Lett.*, vol. 8, 316–319, 15 April 1962.

Cooper, L. N., "Bound Electron Pairs in a Degenerate Fermi Gas," *Phys. Rev.*, vol. 104, 1189-1190, 1956.

Cukauskus, E. J.,"The Effects of Methane in the Deposition of Superconducting Niobium Nitride Thin Films at Ambient Temperature," *J. Appl. Phys.*, vol. 54, no. 2, 1013–1017, Feb. 1983.

Cukauskus, E. J., M. Nisenoff, D. W. Jillie, H. Kroger, and L. N. Smith, "High Quality Niobium Nitride-Niobium Josephson Tunnel Junctions," *IEEE Trans. Magn.*, vol. MAG-19, no. 3, May 3 1983.

D'Addario, L. R. "An SIS Mixer for 90-120 GHz with Gain and Wide Bandwidth," *Int. J. IR and Millimeter Waves*, vol. 5, no. 11, 1419-1442, 1984.

Dolan, G. J., "Offset masks for lift-off photoprocessing," *Appl. Phys. Lett.*, vol. 31, 337–339, Sept. 1977.

Dolan, G. J., T. G. Phillips and D. P. Woody, "Low-noise 115-GHz mixing in superconducting oxide-barrier tunnel junctions," *Appl. Phys. Lett.*, vol. 34, 347–349, Mar. 1, 1979.

Dolan, G. J., R. A. Linke, T. C. L. G. Sollner, D. P. Woody, and T. G. Phillips,"," *IEEE Trans. Microwave Theory Tech.*, vol. MTT-29, 788, 1981.

Ellison, B. N., R. E. Miller, "A low noise 230 GHz SIS receiver," *Intl. J. of IR and Millimeter Waves*, vol. 8, no. 6, 1987.

Ellison, B. N., P. L. Shcaffer, W. Schaal, D. Vail, and R. E. Miller, "A 345GHz SIS Receiver For Radio Astronomy," submited to *Int. J. Infrared and Millimeter Waves*, 1989.

Face, D. W., D. E. Prober, W. R. McGrath, and P. L. Richards, "High quality tantalum superconducting tunnel junctions for microwave mixing in the quantum limit," *Appl. Phys. Lett.*, vol. 48, 1098–1100, April 21, 1986.

Faris, S. M., "Generation and Measurement of Ultrashort Current Pulses With Josephson Devices,"*Appl. Phys. Lett.*, vol. 36, no. 12, pp. 1005-1007, June 1980.

Feynman, R. P., R. B. Leighton, M. Sands, *The Feynman Lectures on Physics*, Reading:Addison-Wesley, 1963.

Fiske, M. D., "Temperature and Magnetic Field Dependence of the Josephson Tunneling Current," *Rev. Mod. Phys.*, vol. 36, 221-222., 1964.

Gavaler, J. R., J. K. Hulm, M. A. Janocko, and C. K. Jones, "Preparation and Superconducting Properties of Thin Films of Transition Metal Interstitial Compounds,"*J. Vac. Sci. Tech.*, vol. 6, no. 1, 177-180, 1969.

Gavaler, J. R., J. Talvacchio, and A. I. Braginski, "Epitaxial Growth of NbN Films," *in Advances in Cryogenic Engineering-Materials*, edited by A. F. Clark and R. P. Reed, Plenum:New York, 1986.

Gheewala, T. R.,"Josephson Logic Devices and Circuit," *IEEE Trans. Elec. Devices*, vol. ED-27, no. 10, 1857-1869, October 1980.

Giaever, I., "Energy gap in superconductors measured by electron tunneling," *Phys. Rev. Lett.*, vol. 5, 147–148, 15 Aug., 1960.

Gray, K. E., R. T. Kampwirth, J. M. Murduck and D. W. Capone II, *Physica*, vol. C152, 445, 1988.

Gurvitch, M., M. A. Washington, and H. A. Huggins, "High Quality Refractory Josephson Tunnel Junctions Utilizing Thin Aluminum Layers," *Appl. Phys. Lett.*, vol. 42, 472–474, 1983.

Gurvitch, M., J. P. Remika, T. M. Rowell, J. Geerk, and W. P. Lowe, "Tunneling, Resistive and Structural Study of NbN and Other Superconducting Nitrides," *IEEE Trans. Magn.*, vol. MAG-21, no. 2, pp. 509–513, March 1985.

Hoffman, D. W., and J. A. Thorton, *Thin Solid Films*, vol. 45, no. 387, 1977.

Hu, Q., C. A. Mears, P. L. Richards, and F. L. Lloyd, "Measurement of Integrated Tuning Elements for SIS Mixers with a Fourier Transform Spectrometer," *Int. J. IR and Millimeter Waves*, vol. 9, no. 4, 303-320, 1988.

Hunt, B. D., H. G. Leduc, S. R. Cypher, J. A. Stern, and A. Judas, "NbN/MgO/NbN Edge-Geometry Tunnel Junctions," *Appl. Phys. Lett.*, vol. 55, no. 1, July 3 1989.

Hunt, B. D., Private Communication, 1989.

Hurrell, J. P., D. C. Pridmore-Brown, and A. H. Silver, "Analog-to-Digital Conversion with Unlatched SQUID's," *IEEE Trans. Elec. Devices*, vol. ED-27, no. 10, 1887-1896, October 1980.

Imamura, T., H. Hoko, and S. Hasuo, "Integration Process For Josephson LSI Based on Nb/Al_x/Nb Junctions," *Extended Abstracts of the 1987 Int. Superconducting Electronics Conference*, pp. 57–62, Aug. 1987.

Inatani, J., T. Kasuga, A. Sakamoto, H. Iwashita, and S. Kodaira, "A 100 GHz Mixer of Nb/Al-AlO_x/Nb Junctions," *IEEE Trans. Magn.*, vol. MAG-23, no.2, March 1987.

Johnson, W. J., "Nonlinear Wave Propagation on Superconducting Tunneling Junctions," Ph.D. Thesis, University of Wisconsin, Madison, 1968.

Josephson, B. D., *Phys. Lett*, vol. 1, 251, 1962.

Josephson, B. D., "Supercurrents through Barriers," *Advances in Physics*, vol. 14, 419–451, 1965.

Kautz, R. L., "Picosecond Pulses on Superconducting Striplines," *J. Appl. Phys.*, vol. 49, no. 1, 308-314, 1978.

Kerr, A. R., S. K. Pan, and M. J. Feldman, "Integrated Tuning Elements for SIS Mixers," *Extended Abstracts of the 1987 Int. Superconducting Electronics Conf.*, Aug. 1987.

Kerr, A. R., S. K. Pan, S. Whiteley, M. Radparvar, and S. Faris, "A Fully Integrated SIS Mixer for 75-100 GHz," *Proceedings, IEEE Microwave Symposium*, May 1990.

Kittel, C., *Introduction to Solid-State Physics*, 5th Ed., John Wiley and Sons:New York, 1976.

Kleinsasser, A. W., and R. A. Buhrman,"High-Quality Submicron Nb Tunnel Junctions with Reactive Ion-Beam Oxidation," *Appl. Phys. Lett.*, vol. 37, no. 9, 841, 1980.

Laibowitz, R. B., R. H. Koch, A. Gupta, G. Koren, W. J. Gallagher, V. Foglietti, B. Oh, and J. M. Viggiano, "All High T_c Edge Junctions and SQUIDs," *J. App. Phys.*, vol. 56, no. 7, 686-688., Feb. 1990.

LeDuc, H. G., private communication, 1987.

LeDuc, H. G., J. A. Stern, S. Thakoor, S. Khanna, "All Refractory NbN/MgO/NbN Tunnel Junctions," *IEEE Trans. Magn.*, vol. MAG-23, no. 2, March 1987.

Letrou, C., D. Crètè, J-C, Pernot, A. Rabhi, and P. Encenaz, "Heterodyne Mixing Experiments With NbN-Based SIS Junctions," *Int. J. of IR and Millimeter Waves*, vol. 8, no. 4, 333-350, 1987.

Lin, B. J., "Optical Methods for Fine Line Lithography," *Fine Line Lithography*, edited by R. Newman, North Holland:Amsterdam, 1980.

Lin, L. J., and D. E. Prober, "Ion-Beam Deposition of NbN_xC_y Thin Films for Microelectronic Applications," *IEEE Trans. Magn.*, vol. MAG-23, no. 2, 839–842, March 1987.

Lukens, J. E., A. K. Jain, and K-L. Wan, "Using the Josephson Effect for Millimeter and Submillimeter Wave Generation," in *Sensing and Signal Processing and Superconducting Materials*, edited by R. Nichols, J. A. Ionson, Proc. SPIE 879, 1988.

Magerlein, J. H., "Specific Capacitance of Josepson Tunnel Junctions," *IEEE Trans. Magn.*, vol. MAG-17, 286-289, 1981.

McGrath, W. R., P. L. Richards, A. D. Smith, H. van Kempen, R. A. Batchelor, "Large gain, negative resistance, and oscillations in superconducting quasiparticle heterodyne mixers," *Appl. Phys. Lett.*, vol. 39, 655–658, Oct. 15, 1981.

McGrath, W. R.,A. V. Räisänen, P. L. Richards, R. E. Harris, and F. L. Lloyd, "Accurate Noise Measurements of Superconducting Quasiparticle Array Mixers," *IEEE Trans. Magn.*, vol. MAG-19, p. 212, 1985.

McGrath, W. R., A. V. Räisänen, and P. L. Richards, "Variable Temperature Loads for Use in Accurate Noise Measurements of Cryogenically-Cooled Microwave Amplifiers and Mixers," *Int. J. of IR and Millimeter Waves*, vol. 7, no. 4, April 1986.

Meisner, W., and R. Ochsenfeld, "Ein Neur Effekt bei Eintritt der Supraleitfähigkeit,"*Naturwissenschaften*, vol. 21, 787-788, 1933.

Meng, X. F., R. S. Amos, A. W. Lichtenberger, R. J. Mattauch, and M. J. Feldman, "NbN Edge Junction Fabrication: Edge Profile Control by Reactive Ion Etching," vol. MAG-25, no. 2, 1239-1242, March 1989.

Miller, D. and P. L. Richards, Private Communication 1990.

Mitsuoka, T., T. Yamashita, T. Nakazawa, Y. Onodera, Y. Saito, and T. Anayama, "Superconductive Transition Temperatures of Reactively Sputtered Niobium Nitride Films,"*J. Appl. Phys.*, vol. 39, 4788, 1968.

Murduck, J. M., D. W. Capone, II, I. K. Schuller, S. Foner, J. B. Ketterson, "Critical Current Enhancement in NbN/AlN Multilayers," *Appl. Phys. Lett.*, vol. 52, no. 6, 504–506, February 1988.

Oya, G., and Y. Onadera, "Superconducting Transition Temperatures of Vapour Deposited Niobium Nitride," *J. Vac. Sci. Tech.*, vol. 7, no. 6, 44–47, Nov./Dec. 1970.

Oya, G., and Y. Onadera, "Transition Temperature and Crystal Structure of Single-Crystal and Polycrystalline NbN Films," *J. Appl. Phys.*, vol. 45, no. 3, 1389–1397, 1974.

Pan, S. K., A. R. Kerr, M. J. Feldman, A. W. Kleinsasser, J. Stasiak, R. L. Sandstrom, and W. J. Gallagher, "An 85-116 GHz SIS Receiver Using Inductively Shunted Edge-Junctions," *IEEE Microwave Theory and Techniques*, vol. 37, no. 3, 580-592, March 1989.

Phillips, T. G., and D. P. Woody, "Millimeter- and submillimeter-wave receivers," *Ann. Rev. Astron. Astrophys.*, vol. 20, 285–321, 1982.

Phillips, T. G., "Techniques of Submillimeter Astronomy," proceedings of *Summer School on Millimeter and Submillimeter Astronomy, Stirling, Scotland*, June 1987.

Pippard, A. B., "An experimental and theoretical study of the relation between magnetic field and current in a superconductor," *Proc. Roy. Soc. (London)*, vol. A216, pp. 547–568, Feb. 24, 1953.

Powell, R. A., ed., *Dry Etching for Microelectronics*, Materials Processing Theory and Practice, vol. 4, North Holland:Amsterdam, 1984.

Räisänen, A. V., W. R. McGrath, P. L. Richards, and F. L. Lloyd, "Broad-Band Match to a Millimeter-Wave SIS Quasi-Particle Mixer," *IEEE Tansactions on Microwave Theory and Technique*, vol. MTT-33, no. 12, December 1985.

Richards, P. L., T. M. Shen, R. E. Harris and F. L. Lloyd, "Quasiparticle heterodyne mixing in SIS tunnel junctions," *Appl. Phys. Lett.*, vol. 34, 345–347, Mar. 1, 1979.

Robertazzi, R. D. and R. A. Buhrman, "Josephson Terahertz Local Oscillator," *IEEE Trans. Magn.*, vol. MAG-25, no. 2, 1384-1387, 1989.

Rudner, S., and T. Claeson, "Arrays of Superconducting Tunnel Junctions as Low Noise 10-GHz Mixers," *Appl. Phys. Lett.*, vol. 34, no. 2, 711–713, 1979.

Rudner, S., M. J. Feldman, E. Kollberg, and T. Claeson,"The Antenna Coupled SIS Quasiparticle Array Mixer," *IEEE Trans Magn.*, vol. MAG-17, no. 2, 690, 1981a.

Rudner, S., M. J. Feldman, E. Kollberg, and T. Claeson,"Superconductor-Insulator-Superconductor Mixing with Arrays at Millimeter-Wave Frequencies," *J. Appl. Phys.*, vol. 52, 6366, 1981b.

Schrieffer, J. R., and J. W. Wilkins, "Two Particle Tunneling Processes Between Superconductors," *Phys. Rev. Lett*, vol. 10, no. 1, Jan. 1, 1963.

Serling, S. A., "High-Vacuum Codeposition of Niobium Nitride," *J. Appl. Phys.*, vol. 43, no. 6, 2869–2872, June 1972.

Shapiro, S., "Josephson Currents in Superconducting Tunneling: The Effect of Microwaves and Other Observations," *Phys. Rev. Lett.*, vol. 11, 80–82, 1963.

Shen, T.-M., P. L. Richards, R. E. Harris, and F. L. Lloyd, "Conversion gain in mm-wave quasiparticle heterodyne mixers," *Appl. Phys. Lett.*, vol. 36, 777–779, May 1 1980.

Shinoki, F., A. Shoji, S. Kosaka, S. Takada, and H. Hayakawa, "Niobium Nitride Josephson Tunnel Junctions with Oxidized Amorphous Silicon Barriers," *Appl. Phys. Lett.*, vol. 38, 285–286, 1981.

Shoji, A., S. Kosaka, F. Shinoki, M. Aoyagi, and H. Hayakawa, "All Refractory Josephson Tunnel Junctions Fabricated by Reactive Ion Etching," *IEEE Trans. Magn.*, vol. MAG-19, 827–830, 1983.

Shoji, A. M. Aoyagi, S. Kosaka, F. Shinoki, and H. Hayakawa,"Niobium Nitride Josephson Tunnel Junctions with Magnesium Oxide Barriers," *Appl. Phys. Lett.*, vol. 46, no. 11, June 1 1985.

Shoji, A., H Aoyagi, S. Kosaka, and F. Shinoki, "Temperature-Dependent Properties of Niobium Nitride Josephson Tunnel Junctions," *IEEE Trans. Magn.*, vol. MAG-23, no. 2, 1987.

Smith A. D., J. A. Carpenter, and L. Lee, "Measured Properties of Superconducting Niobium Microstrip at 100 GHz" *presented at the March meeting of the APS*, March 1990.

Sutton, E. C., "A superconducting tunnel junction receiver for 230 GHz," *IEEE Trans. Microwave Theory Tech.*, vol. MTT-31, 589–592, July 1983.

Talvacchio, J., and A. I. Braginski, "Tunnel Junctions Fabricated from Coherent NbN/MgO/NbN and NbN/Al_2O_3/NbN Structures," *IEEE Trans. Magn.*, vol. MAG-23, no. 2, 859–862, 1987.

Taylor, B. N., and E. Burstein, "Excess Currents in Electron Tunneling Between Superconductors," *Phys. Rev. Lett.*, vol 10., no. 1, 14-17, Jan. 1, 1963.

Thakooor, S., J. L. Lamb, A. P. Thakoor, and S. K. Khanna, "Room Temperature Deposition of Superconducting NbN-for SIS Junctions," *J. Appl. Phys.*, vol. 58, no. 12, 4643, 1985.

Tinkham, M., *Introduction to Superconductivity,* McGraw-Hill:New York, 1975.

Torrey, H. C. and C. A. Whitmer, *Crystal Rectifiers,* MIT Rad. Lab. Series, vol. 15, New York:McGraw Hill, 1948.

Tsuboi, M., J. Inatani, T. Kasuga, R. Kawabe, A. Sakamoto, H. Iwashita, and K. Miyazawa, *Int. J. IR and Millimeter Waves,* vol. 8, no. 1, 1-11, 1987.

Tucker, J. R., *Proceedings of the 14th International Conference on Low Temperature Physics* edited by Krusius, M. and Vuorio, M. , vol. 4, p. 180, North Holland:Amsterdam, 1975.

Tucker, J. R., and M. F. Millea, "Photon detection in nonlinear tunneling devices," *Appl. Phys. Lett.*, vol. 33, 611–613, Oct. 1978.

Tucker, J. R., "Quantum limited detection in tunnel junction mixers," *IEEE J. Quantum Electron.*, vol. QE-15, 1234–1258, Nov. 1979.

Tucker, J. R., in *Reviews of Infrared and Millimeter Waves,* edited by K. J. Button, Plenum:New York, 1983.

Tucker, J. R., and M. J. Feldman, "Quantum detection at millimeter wavelengths," *Rev. Modern Phys.*, vol. 57, 1055–1113, Oct. 1985.

Van Duzer, T., and C. W. Turner, *Principles of Superconducting Devices and Circuits,* Elsevier North Holland:New York, 1981.

Villegier, J. C., L. Vieux-Rochaz, M. Goniche, P. Renard, and M. Vabre, "NbN Tunnel Junctions," *IEEE Trans Magn.*, vol. MAG-21, 498-504, 1985.

Wan, K-L., A. K. Jain, and J. E. Lukens, "Submillimeter Wave Generation Using Josephson Junction Arrays," *IEEE Trans. Magn.*, vol. MAG-23, 1076–1079, 1989.

Watson, D. M. and J. E. Huffman, "Germanium Blocked-Impurity-Band Far-Infrared Detectors," *Appl. Phys. Lett.*, vol. 52, no. 19, 1602-1604, 1988.

Wengler, M. J., D. P. Woody, R. E. Miller and T. G. Phillips, "A low noise receiver for millimeter and submillimeter wavelengths," *Intl. J. of IR and Millimeter Waves,* vol. 6, 697–706, Aug. 1985

Wengler, M. J., Private Communication, 1986.

Wengler, M. J., D. P. Woody, "Quantum noise in heterodyne detection," *IEEE J. of Quantum Electron.*, vol. QE-23, 613–622, May 1987.

Werthamer, N. R., "Nonlinear self-coupling of Josephson radiation in superconducting tunnel junctions," *Phys. Rev.*, vol. 147, 255–263, 8 July 1966.

Whitaker, J. F., R. Sobolewski, D. R. Dykaar, T. Y. Hsiang, and G. A. Mourou, "Propagation Model for Ultrafast Signals on Superconducting Dispersive Striplines," *IEEE Trans. Microwave Theory and Techniques*, vol. 36, no. 2, 277-285, Feb. 1988.

Wolf, P., B. J. Van Zeghboeck, and U. Deutsch, "A Josephson Sampler with 2.1 pS Resolution,"*IEEE Trans. Magn.*, vol. MAG-21, no. 2, 226-229, March 1985.

Wolf, S. A., I. L. Singer, E. J. Cukauskas, T. L. Fracavilla, and E. F. Skelton,"Effects of Deposition Parameters on the Properties of Superconducting RF Reactively Sputtered NbN Films," *J. Vac. Sci. Tech.*, vol. 17, no. 1, 411–414, Jan./Feb. 1980.

Woody, D., P., Private Communication, 1986.

Zmudidzinas, J., Private Communication, 1990.